INL/EXT-21-61295

Advanced Reactor Technologies: Gas-Cooled Reactor Research and Development Quarterly Report

July, August, and September 2020

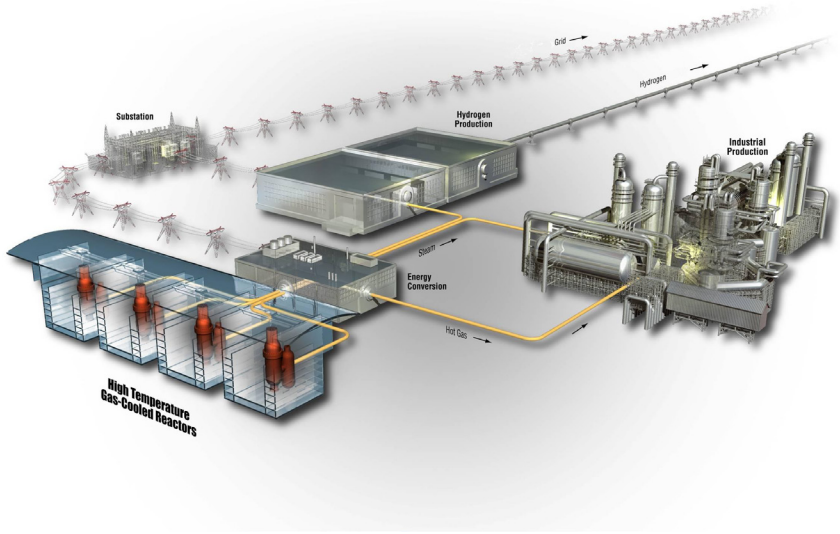

The INL is a
U.S. Department of Energy
National Laboratory
operated by
Battelle Energy Alliance

Idaho National Laboratory

Please note this report contains preliminary data, interim conclusions, and observations from work-in-progress.

INL/EXT-21-61295

Advanced Reactor Technologies: Gas-Cooled Reactor Research and Development Quarterly Report

July, August, and September 2020

Idaho National Laboratory
INL ART Program
Idaho Falls, Idaho 83415

http://www.art.inl.gov

Prepared for the
U.S. Department of Energy
Office of Nuclear Energy
Under DOE Idaho Operations Office
Contract DE-AC07-05ID14517

Page intentionally left blank

INL ART Program

Advanced Reactor Technologies: Gas-Cooled Reactor Research and Development Quarterly Report

July, August, and September 2020

Approved by:

Travis Mitchell

Travis R. Mitchell
INL ART Program Manager

2/22/2021
Date

Page intentionally left blank

CONTENTS

FIGURES

TABLES

ACRONYMS

AGC	advanced graphite creep
AGR	Advanced Gas Reactor
AMIX	Air Moisture Ingress Experiment
ASME	American Society of Mechanical Engineers
ASTM	American Society for Testing and Materials
ATR	Advanced Test Reactor
BCT	body-centered tetragonal
BEC	backscattered electron composition
BPVC	Boiler and Pressure Vessel Code
CCCTF	Core Conduction Cooldown Test Facility
CRP	Coordinated Research Project
DIC	digital image correlation
DLBL	deconsolidation and leach-burn-leach
DOA	Dry Transfer Cubicle Cask Insert Overpack Adaptor
DOE	Department of Energy
DTF	designed-to-fail
DWO	density wave oscillations
EDS	electron dispersive X-ray spectroscopy
EELS	electron energy-loss spectroscopy
FACS	Fuel Accident Condition Simulator
FR	fuel ring
FY	fiscal year
GCR	gas-cooled reactor
GIF	Generation IV International Forum
GWG	Graphite Working Group
HDG	high dose graphite
HFEF	Hot Fuel Examination Facility
HTGR	high-temperature gas-cooled reactor
HTR	high-temperature reactor
IAEA	International Atomic Energy Agency
IMGA	Irradiated Microsphere Gamma Analyzer
INL	Idaho National Laboratory
IPyC	inner pyrolytic carbon

IRDFF	International Reactor Dosimetry and Fusion File
LBL	leach-burn-leach
MFT	maximum fuel temperature
NDMAS	Nuclear Data Management and Analysis System
NMD	Nonmetallic Design and Materials
NRC	Nuclear Regulatory Commission
NSTF	Natural Convection Shutdown Heat Removal Test Facility
NWG	NMD Working Group
OPyC	outer pyrolytic carbon
ORNL	Oak Ridge National Laboratory
PCC	Pearson Correlation Coefficients
PIE	post-irradiation examination
RVE	representative volume element
SEM	scanning electron microscopy
SMT	Simplified Model Test
STEM	scanning transmission electron microscopy
STP	Selected Technical Papers
TA	time-average
TEM	transmission electron microscopy
TF	thermal fluid
TRISO	tristructural isotropic
UAM	uncertainty analysis in modeling
WG	working group
XCT	X-ray computed tomography

Advanced Reactor Technologies: Gas-Cooled Reactor Research and Development Quarterly Report

1. MAJOR ACCOMPLISHMENTS HIGHLIGHTS

1.1 Fuels Development

ngnp

July

- Completed the irradiation campaign for the AGR-5/6/7 experiment and commenced with experiment cooldown. The AGR-5/6/7 experiment achieved a total of 361 effective full-power days and 6,167 MWd.
- Completed a 20-minute live-time Cs/Ce survey with the Irradiated Microsphere Gamma Analyzer (IMGA) of all particles from radially deconsolidated AGR 3/4 Compact 10-4.
- Completed a post-IMGA burn of all segments from radially deconsolidated AGR 3/4 Compact 1-4 and leaching is in progress.
- Received a replacement control board for X-ray tomograph system and installed new board and motors to restore system to full operation.
- Completed an X-ray tomography of all randomly and specially selected particles from AGR-2 Compact 3-1-2.
- Completed radiochemical analyses of half of the samples from the destructive sampling of AGR-3/4 Capsule 12 inner and outer rings.
- Designed and built equipment for leaching AGR-5/6/7 capsule components. Currently testing the equipment on the benchtop.
- Completed transmission electron microscopy (TEM) data collection on three lamellae from the fuel center and half fuel center positions on the unirradiated AGR-2 fuel kernel (F51-LEU01-49T) at the Center for Advanced Energy Studies.
- Completed TEM and precession electron diffraction data analysis and interpretation of particle AGR2-222-RS027.
- Submitted a paper summarizing first two decades of the AGR program to appear in the American Nuclear Society's August edition of Nuclear News.
- Gave numerous presentations at the Gas-Cooled Reactor (GCR) Annual Program Review and at videoconferences with the technical coordination team.
- Completed the shipment to the Nevada National Security Site of the final two waste packages associated with the disposition of excess AGR program uranium-bearing material at Oak Ridge National Laboratory (ORNL) and submitted a letter documenting the early completion of Level 3 Milestone M3AT-20IN030401025 “Complete disposition of unirradiated LEU, NU, and DU at ORNL associated with AGR Fuel Fabrication/Characterization.”

August

- Completed a cross sectioning of additional special particles with features of interest identified through X-ray computed tomography (XCT) from AGR-2 uranium carbide/oxide (UCO) Compact 6-3-3, AGR-2 UCO Compact 6-2-1, AGR-2 UCO Compact 2-2-1, and AGR-2 UO_2 Compact 3-1-2.
- Completed scanning electron microscopy (SEM)/energy-dispersive spectroscopy (EDS) analysis of sectioned special particles from as-irradiated AGR-2 UO_2 Compact 3-1-2 and 1800°C safety-tested AGR-2 UCO Compact 6-2-1.
- Completed an XCT of four additional cracked particles from AGR-2 Compact 2-2-1; all have suitable cracks and will be shipped to Idaho National Laboratory (INL) for reirradiation and safety testing.
- Completed a 6-hour, live-time gamma counting with the IMGA of 15 randomly selected particles from each segment of the radially deconsolidated AGR-3/4 Compact 10-4.
- Completed leach-burn-leach of all segments and samples from the radial deconsolidations of AGR-3/4 Compacts 3-2 and 8-2. Individual particle inspection and gamma counting is incomplete.
- Completed radiochemical analyses of all samples from the physical sampling of AGR-3/4 Capsule 12 inner and outer rings.
- Designed, built, or ordered equipment for leaching AGR-5/6/7 test train components and tested some different designs of equipment on the benchtop.
- Completed reviews of the Fuel Accident Condition Simulator (FACS) furnace temperature versus power histories and determined that no thermocouple drift had occurred and that thermocouple readings from one test to another are consistent.
- Issued the AGR-5/6/7 post-irradiation examination plan in fulfillment of a Level 3 milestone M3AT-20IN030401049, "Complete AGR-5/6/7 Post-Irradiation Examination (PIE) Plan."
- Received the carts that were designed and built to hold the large control cabinet and transformers for the Air Moisture Ingress Experiment (AMIX). These carts allow these items to be moved and transported to the basement of the Fuel Conditioning Facility.
- Hired a postdoctoral researcher to work at INL on fission product transport phenomena associated with the AGR-3/4 experiment.
- Completed a shipment of the final set of AGR-2 Capsule 4 pebble-bed modular reactor lamellae to Nelson Mandela University.
- Completed Fiscal Year (FY) 2020 AGR-5/6/7 experiment monitoring and simulation progress report (INL/EXT-19-55429, Rev 1), M3AT-20IN030401063 on August 28.

September

- Completed an additional microstructural analysis of abnormal particles from AGR-2 UO_2 Capsule 3 compacts.
- Submitted Level 2 milestone deliverable report, "Destructive PIE and Safety Testing of Six AGR-2 UO_2 Capsule 3 Compacts," ORNL/TM-2020/1612, milestone number M2AT-20IN030401043.
- Submitted Level 2 milestone deliverable report, "AGR-2 Loose Particle Heating Tests in the Furnace for Irradiated TRISO Testing," ORNL/TM-2020/1715, milestone number M2AT-20IN030401044.
- Submitted Level 2 milestone deliverable report, "Radial Deconsolidation and Leach-Burn-Leach of AGR-3/4 Compacts 1-4 and 10-4," ORNL/TM-2020/1707, milestone number M2AT-20IN030401048.

- Completed an analysis of precision gamma scanner spectra from the reirradiations of AGR-3/4 fuel compacts.
- Completed an operational test of the FACS furnace ahead of several planned tests with reirradiated fuel compacts and particles; however, the tests of two AGR-3/4 fuel compacts will be delayed due to repairs to cranes and manipulators at the Hot Fuels Examination Facility (HFEF).
- Completed a radiochemical analysis of all the samples from physical sampling of the AGR-3/4 Capsule 12 rings.
- Completed an electron probe microanalysis on sample AGR2-633-RS09.
- Completed selected area diffraction and electron energy-loss spectroscopy for AGR-2633-RS28.
- Installed the AMIX large control cabinet and electrical transformers onto carts to allow them to be moved and transported to the basement of the Fuel Conditioning Facility.
- Received the radiation shielding for the AMIX filter gamma detector and began testing it in the lab.
- Received the cold traps for the AMIX fission gas monitoring system.
- Began Phase I qualification testing of equipment for acid leaching of the stainless-steel shells of the AGR-5/6/7 at HFEF.
- Received the mass spectrometer for residual gas analysis of AMIX.

1.2 High-Temperature Materials Development

Highlights of high-temperature materials activities during July, August, and September 2020 are as follows:

July

- Presented at and participated in the 2020 ART GCR Campaign Program Review.
- Performed single-bar simplified model test (SMT) testing on Alloy 617 at 950°C. During the test, a virtual strain of 0.4%, 0.7%, and 1.34% was achieved for a few cycles each. This test utilized a constant elastic follow-up factor of 3.
- Drafted and issued a report titled “Single-bar SMT Testing on Alloy 617 Using Software Controls” (INL/EXT-20-59163). This completed Milestone M4AT-20IN030502042.

August

- Participated in the August 2020 virtual American Society of Mechanical Engineers (ASME) Boiler and Pressure Vessel Code (BPVC) Week.
- Awarded Certificates of Acclamation by the Section III Committee of the BPVC: “For outstanding volunteer service to ASME and the nuclear industry” to Richard and Jill Wright, recognizing their work in the completion of a major technical contribution to Section III of the BPVC, resulting in the development of Code Case N-898 for the use of Alloy 617 (UNS N06617) for Section III Division 5 Class A elevated-temperature service construction.

September

- Planned scope and budget for FY 2021.
- Drafted and issued a report titled “Effects of Notches on the Intermediate Creep-Rupture Life of Alloy 617 Weldment” (INL/EXT-20-59726). This completed milestone M3AT-20IN030502041.

1.3 Graphite

Highlights of graphite activities during July, August, and September 2020 are as follows:

July

- Installed leadscrew and carriage combination (with brakes) on rail. HFEF activities are on schedule for the receipt of the Advanced Graphite Creep (AGC)-4 experiment on August 17.
- Ran simulations to characterize the mass loss gradient for NBG-18 due to oxidation. Comparing the NBG-18 results to IG-110, a lower diffusivity in NBG-18 causes a narrower relative oxidation profile.
- Submitted manuscript entitled "Background for Addressing Adequacy or Optimization of ASME Section III Division 5 (2017 ed.) Rules for Nonmetallic Core Components" to ASME for publication consideration as a Nuclear Technical Book.
- Revised and moved to ballot a new test standard for the determination of elastic constants from the ultrasonic velocity. An ORNL graphite staff member participated in the American Society for Testing and Materials (ASTM) DO2.F committee meeting.
- Acquired TEM data on several graphite samples. This data will be used to explore the neutron and electron irradiation effects in TEM foils.
- Initiated the preparation of a journal article on the effects of neutron irradiation and electron damage on crystal strains.
- Completed ART Level 2 milestone (M2AT-20OR030504055), "Status Report on ASME Code Development in 2020," (ORNL/TM-2020/1590) due July 31, 2020.
- Completed Level 2 milestone, M2AT-20IN030504038, "HDG-1 Pre-IE Data Package Report" (INL/EXT-20-59175), detailing preirradiation mechanical properties.

August

- Completed and resolved observations on a contractor readiness assessment for the use of the Dry Transfer Cubicle Cask Insert Overpack Adaptor (DOA) at the Materials Fuels Complex HFEF. This allows the use of the DOA for the transfer of the AGC-4 experiment to HFEF for disassembly.
- Optimized reactive surface area parameters for a graphite oxidation model for graphite grade NBG 18. These parameters were derived from data produced by oxidation experiments with variable specimen shapes conducted at INL.
- Acquired computer controller for newly purchased dilatometer in Lab C-18.
- Rearranged AGC specimen storage to make room for AGC-4.
- Completed Level 4 milestone (M4AT-20OR0305040511), ORNL/TM-2020/1591 "USDOE ART Graphite – Selection and Acquisition Strategy." Moreover, the required review of the Generation IV International Forum (GIF) graphite acquisition plan was also completed.
- Provided an additional response and review of Nuclear Regulatory Commission (NRC) comments on ASME graphite code (ASME BPV III, 5, HHA) to INL.
- Submitted a manuscript on the technical basis of the graphite design code (ASME BPV III, 5, HHA) to ASME for publication as a Nuclear Technical Book. The submitted manuscript is being reviewed by ASME for acceptance, and we are currently waiting for proofs and copyright permissions.

- Provided a copy of the International Atomic Energy Agency (IAEA) Graphite Database to the GIF Handbook technical lead. The database was uploaded into the Handbook Chapter K-Data Packages for further processing.
- Prepared XCT for future modeling simulations.
- Performed preliminary simulations (based on porosity) of an effective thermal conductivity for four of the AGC selected graphite grades.
- Supported the approval of new ASTM Selected Technical Papers (STP) symposium on nuclear graphite testing by ASTM leadership for 2021. The new symposium is titled "Graphite Testing for Nuclear Applications: The Validity and Extension of Test Methods for Material Exposed to Operating Reactor Environments" and will be held in conjunction with International Nuclear Graphite Specialist Meeting 2021 in September.
- Developed changes to the ASTM D7846-16 "Standard Practice for Reporting Uniaxial Strength Data and Estimating Weibull Distribution Parameters for Advanced Graphites" to be submitted to ballot.
- Attended and participated in the ASME August code week (held virtually) and in various nonmetallic material related committees. An update on the ASME/NRC Roadmap effort, including ASME's response to NRC's (Numark, LLC) code assessment, was presented by ART graphite researchers to multiple committees. This assessment was comprehensive and will provide guidance on future modifications to the code.
- Completed the preirradiation material testing of graphite samples for the first high dose graphite (HDG) test train. External report INL/EXT-20-59175, "HDG-1 Graphite Pre-Irradiation Data Package Report," was released in August detailing the material property measurements of each HDG-1 specimen, individual sample locations within the capsule, and expected total dose levels achieved for this 600°C experiment (final dose range = 0.5 to 15 dpa).
- Completed Level 3 milestone (M3AT-20IN0305040210), "Complete AGC-4 Sizing and Shipping for PIE." The milestone was originally due May 1, 2020. Due to COVID-19 related delays at INL, it was completed August 25, 2020.
- Initiated the irradiation of HDG-1 in the Advanced Test Reactor (ATR) for the first of 11 planned cycles. This experiment is reirradiating samples from AGC-2 to dose levels of approximately 15 dpa.

September

- Optimized multiple parameters in a graphite oxidation model developed by Kane and compared the simulated results to experimental results produced at INL. This optimization and the subsequent simulations, while reasonably successful, highlighted avenues for further model development.
- Initiated the GIF Graphite Working Group (GWG) report on graphite oxidation. This will outline graphite oxidation research activities from the last 10 years (2010–2020) funded by the Department of Energy (DOE) through the Next-Generation Nuclear Plant (NGNP) and ART programs.
- Submitted "A Macro-scale Ruck and Tuck Mechanism for Deformation in Ion-irradiated Polycrystalline Graphite," (by Doug Liu, David Cherns, Steve Johns, Yan Zhou, Junliang Liu, Wei-Ying Chen, Ian Griffiths, Karthik Chinnathambi, Meimei Li, Martin Kuball, Joshua J Kane, William E Windes), to *Carbon*, September 2020.

1.4 Methods

Highlights of methods activities during July, August, and September 2020 are as follows:

July

- Completed the reference RELAP5-3D calculation. The overall conclusion is that we can qualitatively reproduce the countercurrent single-phase gas flows that happen during the depressurized conduction cooldown transient, which was the main purpose of the test.
- Continued with planned FY 2020 experimental matrix testing at the Natural Convection Shutdown Heat Removal Test Facility at Argonne National Laboratory. The tests started at a 60% water inventory in the last week of July and will target the boil-off stage where the closed natural circulation loop breaks and flow stagnates.

August

- Submitted the Level 2 milestone deliverable documenting testing accomplishments and results from year two of the water-based Natural Convection Shutdown Heat Removal Test Facility program (M2AT-20AN030302012).
- Submitted the Level 3 milestone deliverable "Issue Summary of INL Phase IV Transient Results for IAEA CRP on HTGR UAM Benchmark" (M3AT-20IN030301012), due September 4, 2020.
- Completed the RELAP5-3D simulation of the loss-of-cooling test PG 26 performed at the High Temperature Test Facility.

September

- Submitted the Level 3 milestone on the RELAP5-3D Modeling of the PG 26 test at the High Temperature Test Facility (M3AT 20IN030302021) on September 30, 2020.

2. DETAILED ACCOMPLISHMENTS

2.1 Fuels Development and Qualification

2.1.1 Safety Testing and PIE of AGR-2 UO_2 fuel compacts

Six of the AGR-2 Capsule 3 UO_2 compacts were shipped to ORNL for as-irradiated PIE or safety testing in the Core Conduction Cooldown Test Facility (CCCTF) followed by a post-safety-test examination. Detailed results from the safety testing and destructive PIE were reported in a FY 2020 deliverable report (Hunn et al. 2020), and excerpts from that report are summarized herein. The individual identities and key irradiation and safety test parameters for these six compacts are listed in Table 1. Compacts 3-1-2 and 3-3-1 were examined in the as-irradiated state. The compacts were deconsolidated to break up the matrix, and the particles and matrix debris were leached in hot nitric acid to detect exposed actinides and fission products. Particles were separated for an IMGA survey, while the matrix debris was burned and leached again to measure any remaining actinides and fission products not removed by the previous leaches. Any particles with abnormal inventories of the gamma-emitting isotopes measured with the IMGA were put aside for further analysis, which included longer, 6-hour gamma counting and various combinations of XCT, optical microscopy, and SEM with EDS. Additional particles were randomly selected and subjected to the same examinations. Safety testing was performed on Compacts 3-1-1, 3-3-2, 3-4-2, and 3-4-1. The primary focus of the safety testing was to measure releases of cesium, which would indicate a failure of the normally high retention of this isotope exhibited by good silicon carbide (SiC). A low krypton release indicated that no particles experienced complete tristructural isotropic (TRISO) failure. After the completion of a safety test, each safety-tested compact was subjected to the same series of examinations performed on the as-irradiated compacts.

Table 1. Irradiation and safety test parameters for AGR-2 UO_2 Capsule 3 compacts analyzed at ORNL.

Compact [a]	Safety test (°C)	Burnup [b] (% FIMA)	Fast fluence [b] (n/m^2)	Temperature [c] (°C)		
				TAVA	TA_{min}	TA_{max}
AGR-2 3-1-2	none	10.66	3.45×10^{25}	1012	903	1084
AGR-2 3-3-1	none	10.46	3.49×10^{25}	1062	997	1104
AGR-2 3-1-1	1500	10.60	3.41×10^{25}	1011	900	1083
AGR-2 3-3-2	1600	10.54	3.53×10^{25}	1062	999	1105
AGR-2 3-4-2	1600	10.69	3.50×10^{25}	1013	904	1085
AGR-2 3-4-1	1700	10.62	3.47×10^{25}	1013	901	1085

[a] The compact identification denotes the compact's location in the irradiation test train: *capsule-level-stack*.

[b] Compact average burnups and fast neutron fluences ($E_n > 0.18$ MeV) are based on physics calculations (Sterbentz 2014).

[c] Compact time-average, volume-average (TAVA), time-average minimum (TA_{min}) and time-average maximum (TA_{max}) temperatures are based on thermal calculations (Hawkes 2014).

2.1.1.1 Summary of safety test results

Table 2 lists the cumulative releases of fission products of interest at the end of each AGR-2 UO_2 Capsule 3 safety test. Values are reported in terms of a *compact fraction*, which is the amount released divided by the calculated compact inventory, and the number of *particle equivalents*, which is defined as the compact fraction multiplied by the average number of particles per compact: 1,543 for AGR-2 UO_2 compacts (Hunn, Montgomery, and Pappano 2010). Krypton releases were negligible at 1500°C and 1600°C, clearly indicating there were no particles in these three tests with completely failed TRISO. The ^{85}Kr release during the 1700°C safety test was somewhat elevated, with a cumulative release of 0.067 particle equivalents. However, it did not show the expected magnitude and temporal profile of ^{85}Kr release from a failed TRISO particle. The ^{85}Kr release during the 1700°C safety test was consistent with the transport through an intact pyrocarbon from a particle with failed SiC (Demkowicz et al. 2015).

Table 2. Cumulative releases of radioactive isotopes from safety-tested AGR-2 UO_2 Capsule 3 compacts.

Fission product	Compact 3-1-1 1500°C safety test	Compact 3-3-2 1600°C safety test	Compact 3-4-2 1600°C safety test	Compact 3-4-1 1700°C safety test
^{85}Kr	~6.2×10^{-6} (~0.01)	<1×10^{-6} (<0.002)	<1×10^{-6} (<0.002)	4.33×10^{-5} (0.067)
^{90}Sr	3.35×10^{-5} (0.052)	1.44×10^{-3} (2.23)	2.70×10^{-3} (4.16)	4.47×10^{-2} (68.9)
^{110m}Ag	6.37×10^{-3} (9.83)	1.73×10^{-2} (26.6)	1.13×10^{-2} (17.5)	8.92×10^{-2} (138)
^{134}Cs	3.62×10^{-4} (0.56)	2.11×10^{-3} (3.26)	9.29×10^{-3} (14.3)	8.72×10^{-2} (135)
^{137}Cs	3.90×10^{-4} (0.60)	2.05×10^{-3} (3.16)	9.21×10^{-3} (14.2)	8.21×10^{-2} (127)
^{154}Eu	2.90×10^{-5} (0.045)	3.76×10^{-4} (0.58)	3.15×10^{-4} (0.49)	3.05×10^{-3} (4.70)

Values are reported as compact fractions and particle equivalents (in parentheses).

Cesium releases indicated a SiC failure in one particle at 1500°C, and there was an exponential increase in SiC failure as safety test temperatures were increased from 1500° to 1600°C and again from 1600 to 1700°C. Figure 1 illustrates how the cesium release from the SiC failure varied not only in magnitude but also as a function of time. At 1500°C, significant cesium from the SiC failure was not observed until after a soak time of 258 h. Shorter periods before the obvious onset of SiC failure were observed at 1600°C (after 39 hours for Compact 3-3-2 and after 87 hours for Compact 3-4-2). A significant cesium release occurred in the first 13 hours at 1700°C. The 1500°C safety test was extended 100 hours beyond the normal 300 hour time-at-temperature test period to allow for evolution and further observation of the SiC failure. The 1700°C safety test was terminated after 164 hours because of excessive SiC failure and release of radioactive nuclides. Cumulative releases of ^{90}Sr, ^{110m}Ag, and ^{154}Eu were dominated by SiC failure at 1600°C and 1700°C, as discussed in ORNL/TM-2020/1612 (Hunn et al. 2020).

Figure 2 is a plot of the ^{134}Cs release rates in particle equivalents per hour with the time for each data set shifted to roughly align the data to the onset of a significant cesium release from SiC failure. This graph illuminates the similarities and differences in the release behavior. The initial 50 hours of significant cesium release from Compact 3-3-2 at 1600°C was similar to that from Compact 3-1-1 at 1500°C, which suggests that the release from Compact 3-3-2 during most of this period was from a single particle with failed SiC. The higher slopes of the release rate trendlines for Compacts 3-4-1 and 3-4-2 suggest release from more than one particle soon after onset of SiC failure. While the release rate from Compact 3-3-2 overlaid that from Compact 3-1-1 for the first 50 hours after onset, it did not drop off afterward like it did in Compact 3-1-1 as available cesium in the one particle with failed SiC was depleted. The gradual increase in the Compact 3-3-2 ^{134}Cs release rate after 50 hours indicated that more and more particles with failed SiC were contributing as time progressed. Compacts 3-4-1 and 3-4-2 showed even greater escalating release rates consistent with their higher populations of particles with failed SiC.

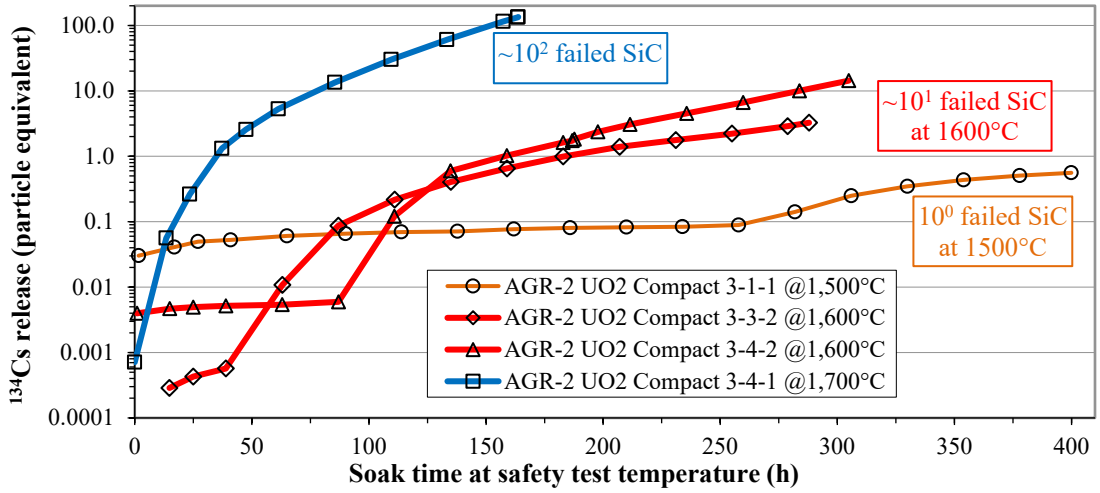

Figure 1. ^{134}Cs release during safety testing of four AGR-2 UO_2 compacts (^{137}Cs release was similar).

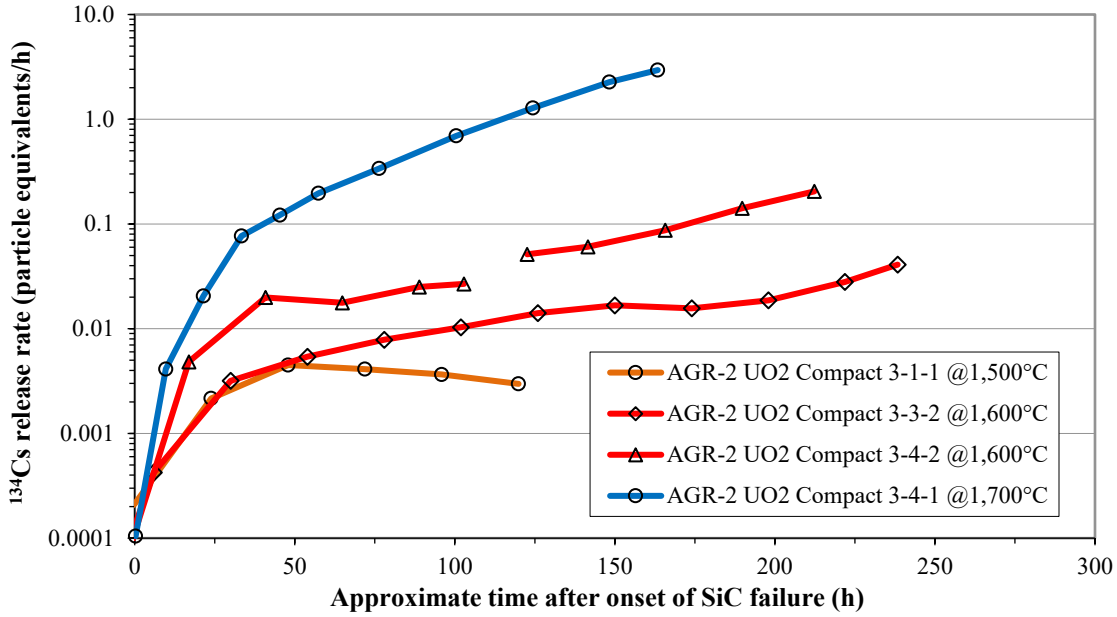

Figure 2. Rate of ^{134}Cs release during safety testing of four AGR-2 UO2 compacts.

2.1.1.2 Summary of DLBL and Microstructural Analysis

Additional insight regarding particle failure was provided by deconsolidation and leach-burn-leach (DLBL) analyses, followed by an IMGA survey and microstructural analysis of individual particles. Table 3 is a compilation of the ^{238}U detected in each leach solution during the DLBL analysis of the six AGR-2 UO_2 compacts. The particle equivalents of ^{238}U detected in the acid solutions collected at the end of each DLBL step indicated whether kernels were exposed to the acid and at what stage the exposure occurred. Similar results, as reported in ORNL/TM-2020/1612 (Hunn et al. 2020), were obtained for other key indicators for exposed kernels (e.g., ^{235}U, ^{236}U, and ^{144}Ce). There were <0.13 particle equivalents of ^{238}U detected during DLBL of as-irradiated Compact 3-3-1. This indicated that no kernels were exposed in this compact because no particles with failed TRISO coatings were found. Failed TRISO particles would have resulted in significant dissolved uranium in the preburn leaches. Furthermore, no particles with failed SiC layers were found, which would have resulted in dissolved uranium in the postburn particle leaches. The relative amounts of ^{238}U in each leach solution indicated that the uranium was primarily in the Compact 3-3-1 matrix.

The acid from the deconsolidation of the as-irradiated Compact 3-1-2 was included in the first preburn leach acid. There were 0.043 particle equivalents of ^{238}U in the first preburn leach acid, which was about double what was detected during the deconsolidation and first preburn leach of Compact 3-3-1 but still low enough to rule out the presence of particles with failed TRISO coatings. However, the amount of ^{238}U in the second preburn leach was higher (0.113 particle equivalents), which suggested that a kernel had been exposed at some point during that stage. During the pot boil to further digest the matrix debris before sieving out the particles, 1.05 particle equivalents of ^{238}U were detected, which indicated that at least one kernel was exposed and leached prior to sieving. In accordance with the DLBL procedure (Hunn and Montgomery 2020), the pot boil acid was distilled off prior to the matrix burn, and the ^{238}U in that acid was included in the 1.02 particle equivalents of ^{238}U detected in the postburn matrix leaches, which was consistent with the value measured in the digestion acid and related to the same exposed kernel. There were 4.466 particle equivalents of ^{238}U in the first postburn particle leach, and 0.016 particle equivalents of ^{238}U in the second postburn particle leach, which indicated that the exposed uranium had been effectively dissolved in the first leach. The uranium detected in the postburn particle leaches was likely related to exposed kernels and kernel fragments from particles fractured during IMGA, due to operational problems during the Compact 3-1-2 survey, as discussed in ORNL/TM-2020/1612 (Hunn et al. 2020).

Table 3. ^{238}U detected in DLBL solutions.

DLBL Step	3-1-2	3-3-1	3-1-1	3-3-2	3-4-2	3-4-1
Deconsolidation acid [a]	—	8.18E-6 (0.013)	3.75E-6 (0.0058)	2.24E-6 (0.0035)	1.93E-6 (0.0030)	—
Preburn leach 1	2.82E-5 (0.043)	4.68E-6 (0.0072)	1.17E-6 (0.0018)	1.38E-3 (2.137)	4.49E-4 (0.692)	—
Preburn leach 2 [b]	7.34E-5 (0.113)	2.93E-6 (0.0045)	6.72E-6 (0.010)	8.00E-4 (1.235)	1.26E-3 (1.938)	—
Postburn matrix leach 1 [c]	6.55E-4 (1.011)	5.52E-5 (0.085)	6.85E-4 (1.058)	4.15E-4 (0.640)	1.41E-3 (2.170)	2.96E-3 (4.562)
Postburn matrix leach 2	3.77E-6 (0.0058)	2.40E-6 (0.0037)	6.68E-6 (0.010)	1.15E-5 (0.018)	1.01E-4 (0.156)	1.78E-6 (0.0027)
Postburn particle leach 1	2.89E-3 (4.466)	6.37E-6 (0.0098)	1.49E-5 (0.023)	6.74E-6 (0.010)	4.74E-3 (7.314)	1.47E-3 (2.263)
Postburn particle leach 2	1.06E-5 (0.016)	1.87E-6 (0.0029)	4.62E-6 (0.0071)	1.89E-6 (0.0029)	4.56E-6 (0.0070)	4.96E-6 (0.0077)

DLBL Step	3-1-2	3-3-1	3-1-1	3-3-2	3-4-2	3-4-1
Subtotal of ^{238}U removed before IMGA survey	7.61E-4 (1.174)	7.34E-5 (0.113)	7.04E-4 (1.086)	2.61E-3 (4.032)	3.21E-3 (4.960)	2.96E-3 (4.565)
Total	3.67E-3 (5.656)	8.17E-5 (0.126)	7.23E-4 (1.116)	2.62E-3 (4.046)	7.96E-3 (12.281)	4.43E-3 (6.835)

Note: Values are reported as compact inventory fractions and particle equivalents (in parentheses).
[a] The deconsolidation acid from Compact 3-1-2 was combined with the first preburn leach acid.
[b] The second preburn leach values for Compacts 3-3-2 and 3-4-2 include analyses of a subsequent water rinse.
[c] The first postburn matrix leach values for Compact 3-4-1 include analyses of prior leach solutions.

The Compact 3-1-2 particle whose kernel was leached during DLBL (Particle 312-SP02) was detected and sorted from the main population during the IMGA survey because of its low measured vs. calculated (M/C) value for ^{137}Cs (Figure 3). The M/C value was derived from the measured particle activities (A_i) and the calculated average particle activity (A_{calc}), as shown in the equation in Figure 3 and described in ORNL/TM-2020/1612 (Hunn et al. 2020). Particles 312-SP01, 312-SP03, 312-SP05, and 312-SP06 were also identified by their unusual ^{137}Cs M/C values (Figure 3), but these unusual values were not related to abnormal TRISO particle performance, as discussed further in ORNL/TM-2020/1612 (Hunn et al. 2020). The reason for the leached kernel in Particle 312-SP02 was revealed by XCT. The larger fractures in the buffer and inner pyrolytic carbon (IPyC) layer evident in the two XCT images shown in Figure 4 were related and part of one connected crack. The buffer and IPyC fractures were aligned where the two layers were still attached on one side of the fractures, and the fractures were presumably related to the stress along this boundary between attached and detached buffer/IPyC. At these locations, the IPyC was also detached from the SiC and the connected buffer/IPyC structure was curled inward. This type of behavior has been observed in other AGR particles and indicated that the fracture probably occurred during irradiation, as it was apparently followed by additional radiation-induced dimensional changes in the buffer and IPyC. Partial fractures in the SiC were evident along the boundary of where the IPyC layer had pulled away from the SiC, which would have been a location of elevated stress on the SiC. At one location along this boundary, there was a circumferential fracture in the SiC. This fracture had not propagated more than about 5 µm from the IPyC/SiC interface. There were also two radial cracks through the SiC layer. One of these was located in the region of the circumferential crack and was aligned with a crack through the outer pyrolytic carbon (OPyC). The radial cracks in the SiC and OPyC probably occurred at the same time, namely, after irradiation and sometime at the end of the second preburn leach or during the digestion step, when kernel leaching initiated during DLBL.

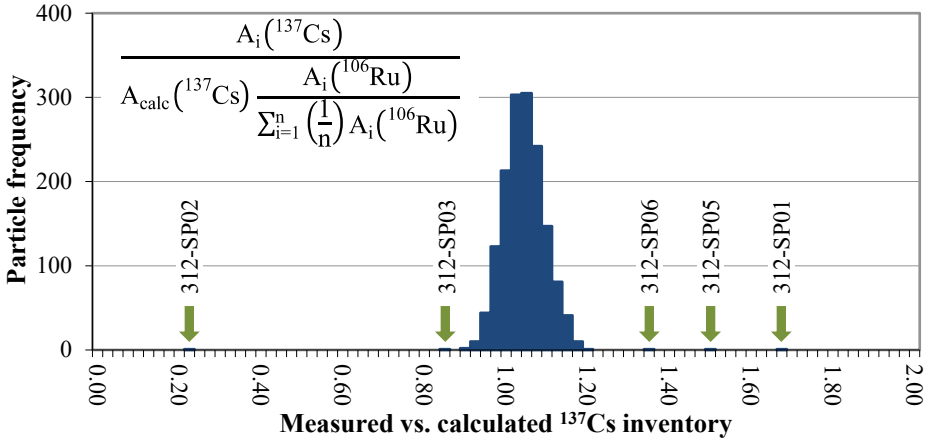

Figure 3. Measured vs. calculated ^{137}Cs inventory in 1,527 particles from Compact 3-1-2, adjusted for particle variability using ^{106}Ru.

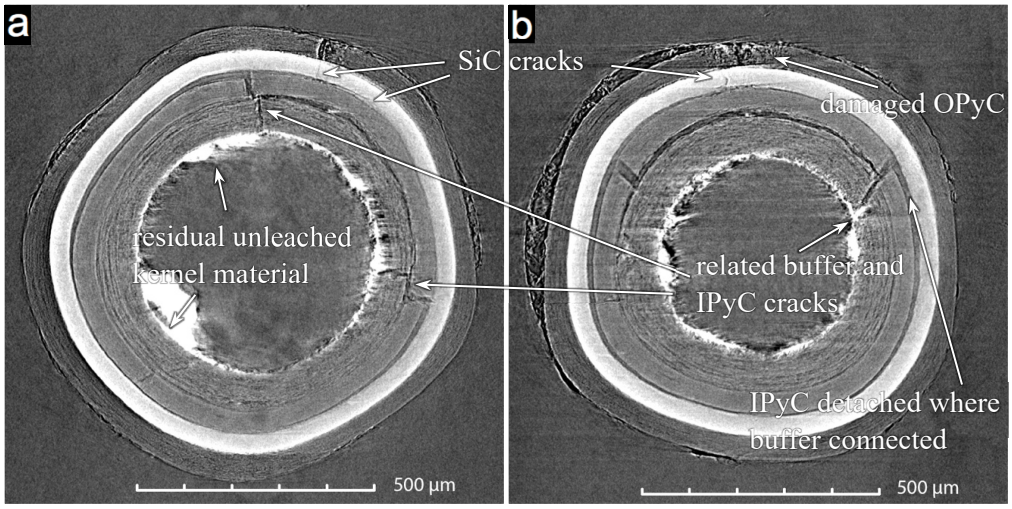

Figure 4. (a) X-ray tomogram through the center of Particle 312-SP02 and (b) off-midplane X-ray tomogram showing the plane orthogonal to Figure 4a.

The amounts of ^{238}U in the deconsolidation acid and first preburn leach of the particles and matrix debris from 1500°C safety-tested Compact 3-1-1 were both <0.006 particle equivalents (Table 3). This confirmed that no kernels were exposed, as expected from the low ^{85}Kr release during safety testing. The amount of ^{238}U in the second preburn leach was 0.010 particle equivalents. While this was a small amount, the fact that the second leach was not lower than the first indicated conditions may have changed. The first postburn leach of the matrix debris contained 1.06 particle equivalents of ^{238}U, and this level of uranium was also detected in the digestion acid prior to sieving. This level of ^{238}U in the deconsolidation acid indicated that a kernel was exposed and leached during, or just before, that step in the procedure. No particles with low cesium were identified and separated out during the IMGA survey. Therefore, the one exposed kernel detected during DLBL was likely from the particle with failed SiC that released cesium during safety testing. The kernels in particles with failed SiC are sometimes leached during the preburn DLBL stages as a result of the fracture of an intact OPyC layer, which would have previously prevented release of fission gases. These particles are sometimes recovered for analysis, but it is not unusual for the particle coatings to fragment into pieces, which is apparently what happened in this case. The small uptick of ^{238}U observed in the second preburn leach suggests that the kernel was exposed at the end of the second preburn leach, perhaps when the particles and matrix debris in the Soxhlet thimble were rinsed to collect residual acid after removing the thimble from the Soxhlet extraction apparatus. This would have resulted in a small amount of uranium dissolving in the rinse solution. The total amount of ^{238}U in the postburn particle leaches was 0.03 particle equivalents, which indicated that no particles with failed SiC were missed during the IMGA survey and included in the particle burn-leach.

The deconsolidation acids from 1600°C safety-tested Compacts 3-3-2 and 3-4-2 showed negligible concentrations of ^{238}U (Table 3). This supported the safety test conclusions that there were no particles with failed TRISO in these compacts. However, subsequent leaching of the particles from these two compacts indicated that kernels were exposed at various stages of the DLBL. There were 4.03 particle equivalents of ^{238}U detected in the DLBL analysis of the particles and matrix debris before the IMGA survey of the Compact 3-3-2 particles (i.e., the total in all DLBL solutions except from the two postburn particle leaches). Four particles associated with this dissolved uranium were identified during the IMGA survey because of their low ^{144}Ce activities (see Figure 5), and XCT showed that most of their kernel material was absent in each particle (Figure 6–Figure 9). Particle 332-SP01 had extensive fracturing in the pyrocarbon and SiC layers. The other three particles had circular, low-density regions penetrating the SiC where the local IPyC fracture had exposed the SiC to extensive carbon monoxide (CO) corrosion. Evidence for CO corrosion from an SEM and EDS analysis included the depletion of silicon at the SiC corrosion site, large SiO_2 precipitates in the gap between the buffer and IPyC layers, Si-O deposits in the banded porosity within the buffer layer, and intergranular corrosion (Figure 10 and Figure 11).

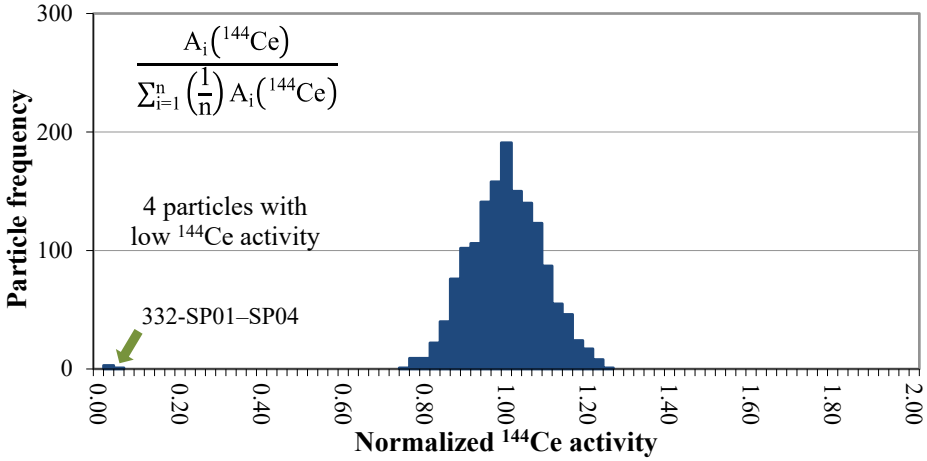

Figure 5. Normalized ^{144}Ce activity in 1510 particles from Compact 3-3-2.

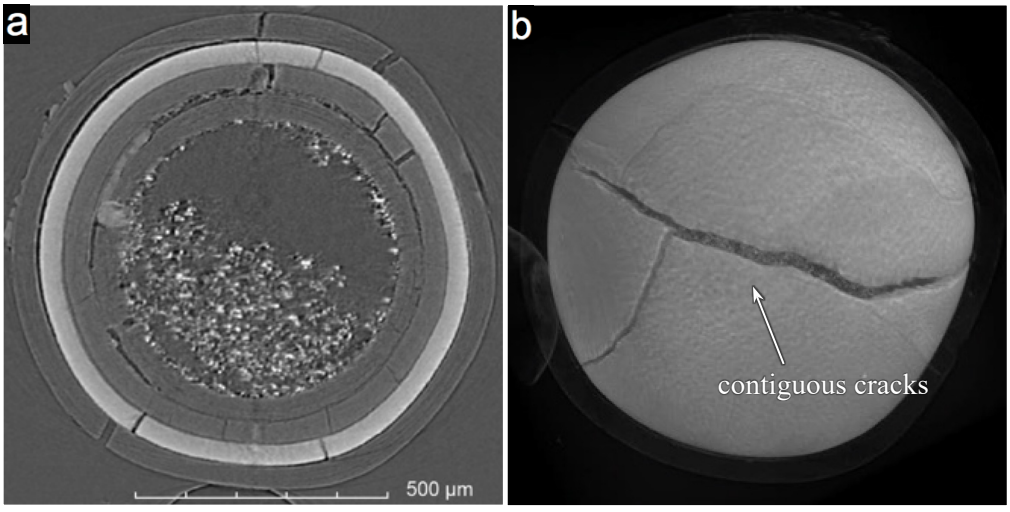

Figure 6. (a) X-ray tomogram of Particle 332-SP01 and (b) 3D representation of the SiC surface.

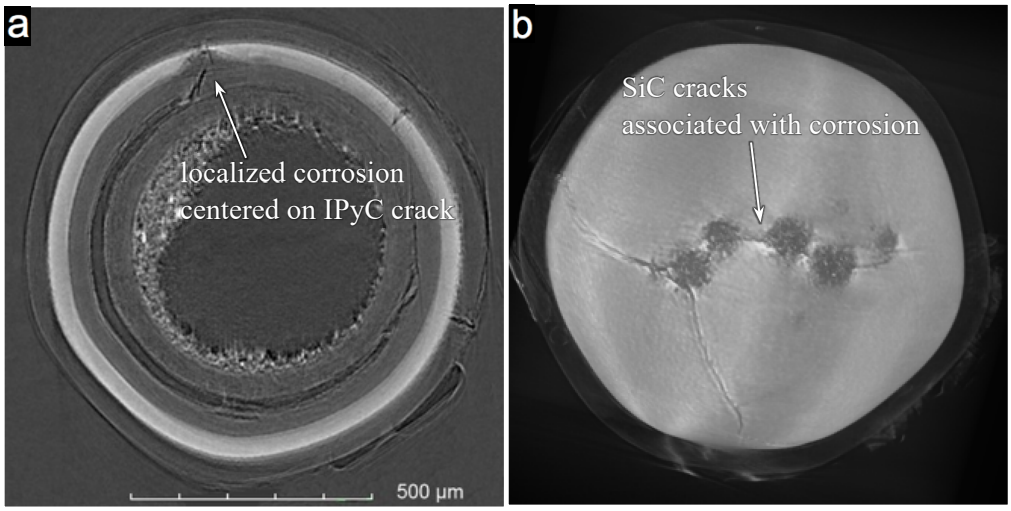

Figure 7. (a) X-ray tomogram of Particle 332-SP02 and (b) 3D representation of the SiC surface.

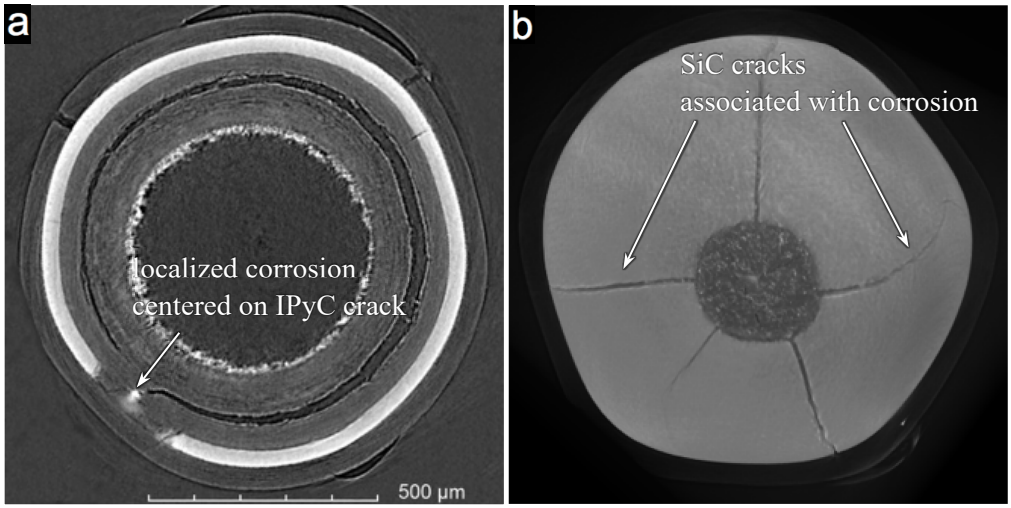

Figure 8. (a) X-ray tomogram of Particle 332-SP03 and (b) 3D representation of the SiC surface.

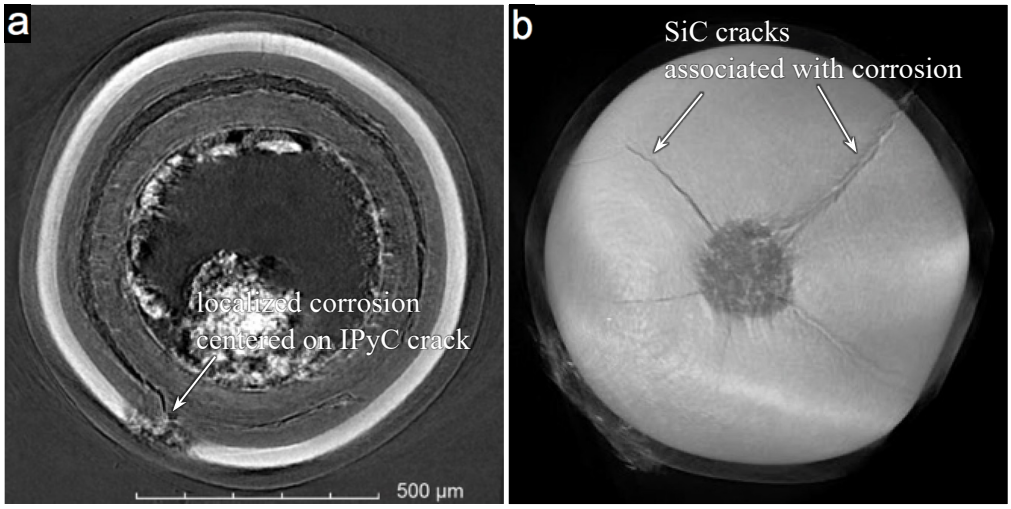

Figure 9. (a) X-ray tomogram of Particle 332-SP04 and (b) 3D representation of the SiC surface.

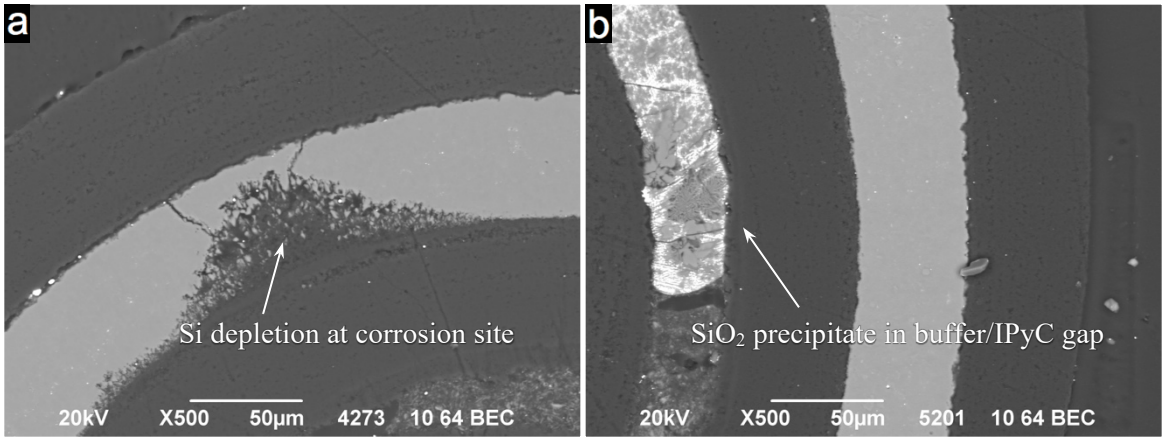

Figure 10. Backscattered electron composition (BEC) images of regions of interest in Particle 332-SP02.

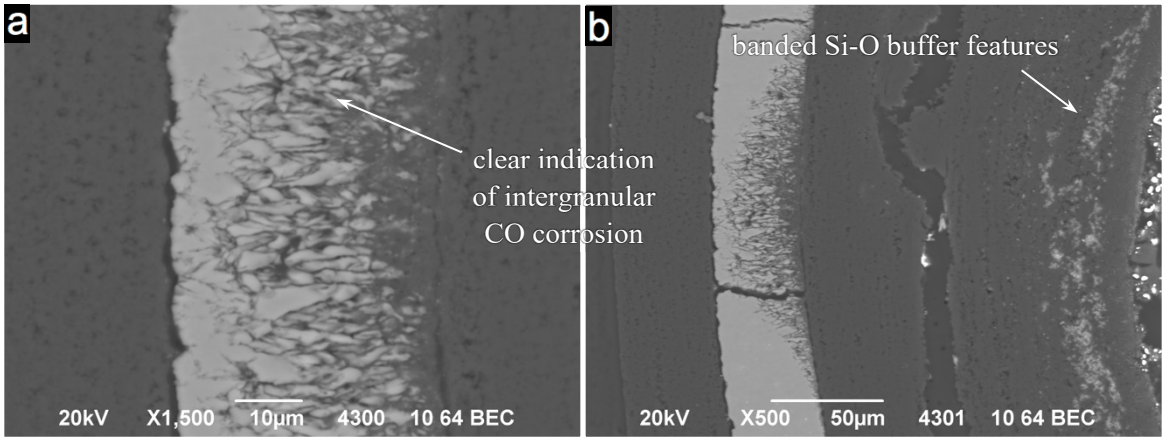

Figure 11. BEC images of corroded SiC in Particle 332-SP04.

There were 4.96 particle equivalents of ^{238}U detected in the pre-IMGA DLBL analysis of the particles and matrix debris from Compact 3-4-2. IMGA survey found four particles whose kernel material had been mostly removed and one particle (Particle 342-SP06) that had partial kernel leaching. This left around one particle equivalent of uranium unaccounted for; therefore, it is possible that there was a Compact 3-4-2 particle with failed SiC that was broken during DLBL and not recovered. Analysis with XCT, SEM, and EDS showed extensive corrosion and SiC fracture in the leached particles (Figure 12–Figure 16), similar to that observed in the Compact 3-3-2 particles with SiC failure. As expected from the amount of cesium released in the CCCTF during safety testing of Compacts 3-4-2, an IMGA survey also revealed additional particles with reduced ^{137}Cs M/C values (Figure 17). These particles had a lower fractional release that indicated a less extensive SiC failure. The microstructural analysis of these particles is discussed in ORNL/TM-2020/1612 (Hunn et al. 2020). There were 7.32 particle equivalents of ^{238}U dissolved during the postburn leaches of the Compact 3-4-2 particles. This uranium may have been from particles with failed SiC that were not sorted out by the IMGA survey because their cesium release was not high enough to segregate them from the normal particles.

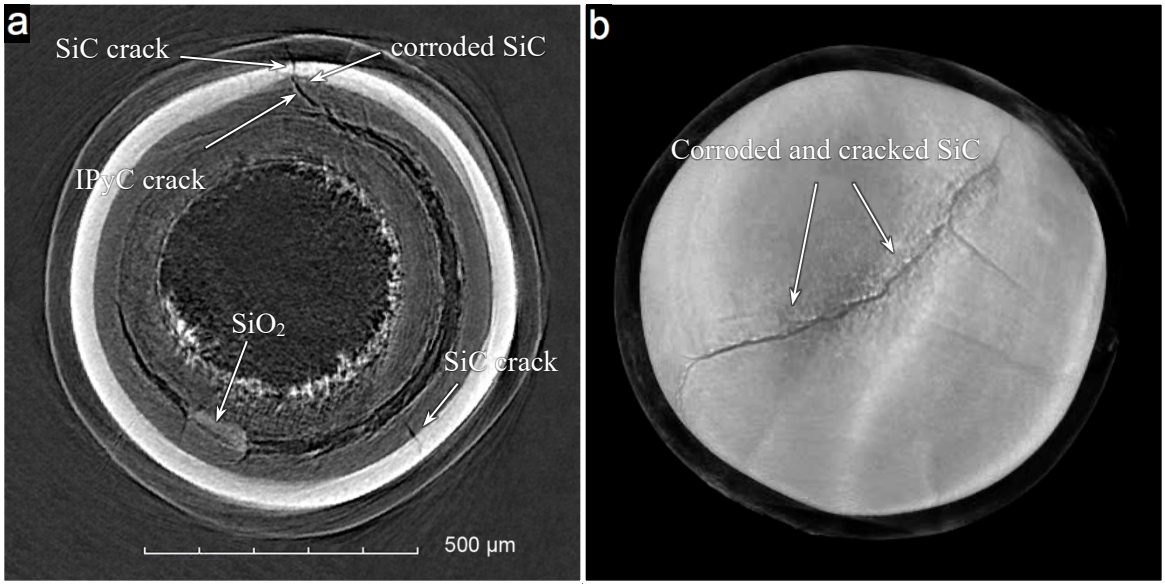

Figure 12. X-ray tomograms of Particle 342-SP01 showing corroded and cracked SiC.

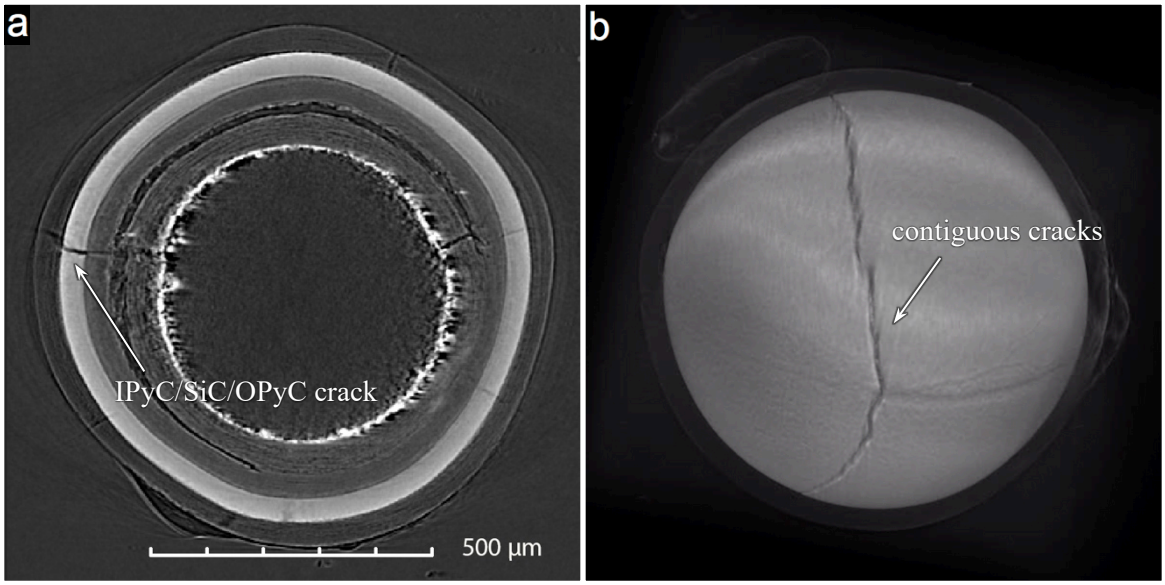

Figure 13. (a) X-ray tomogram of Particle 342-SP02 and (b) 3D representation of the SiC surface.

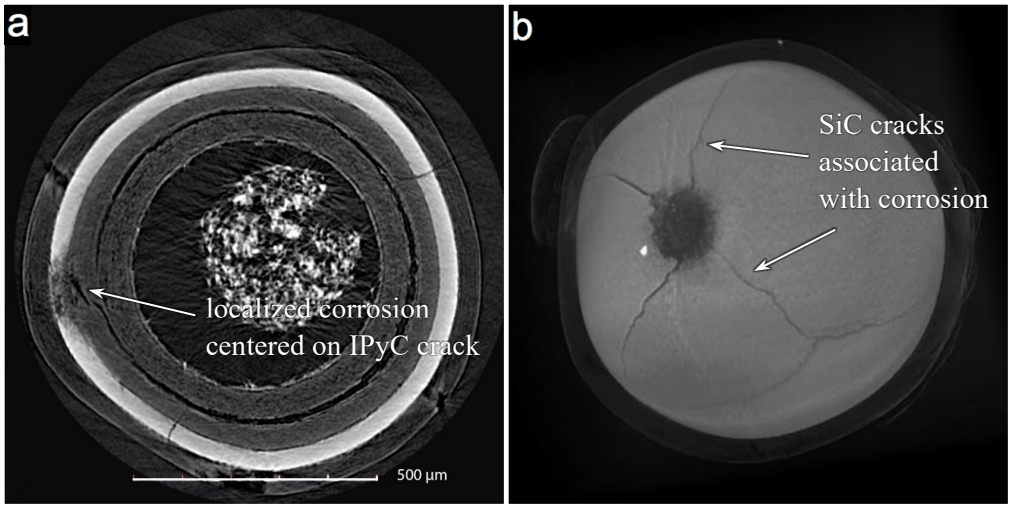

Figure 14. (a) X-ray tomogram of Particle 342-SP04 and (b) 3D representation of the SiC surface.

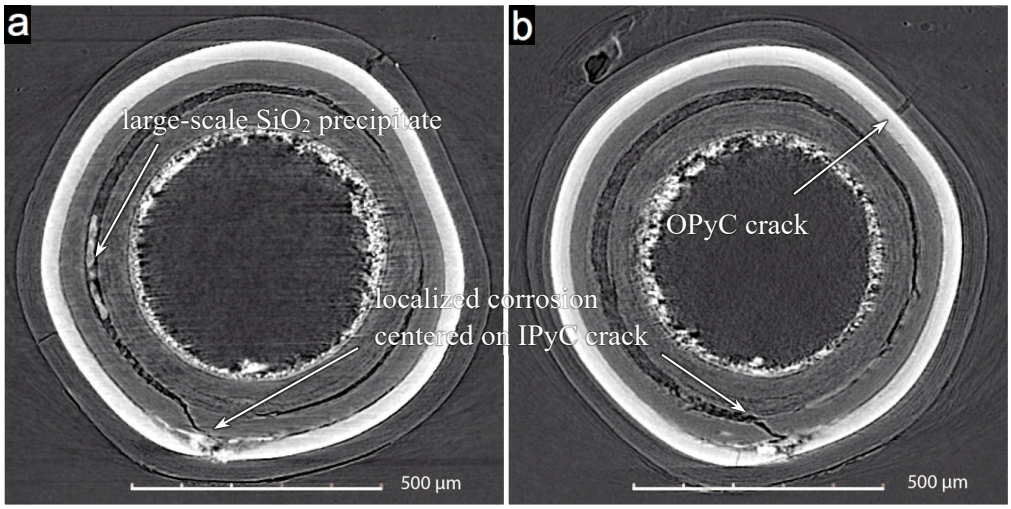

Figure 15. X-ray tomograms of Particle 342-SP05.

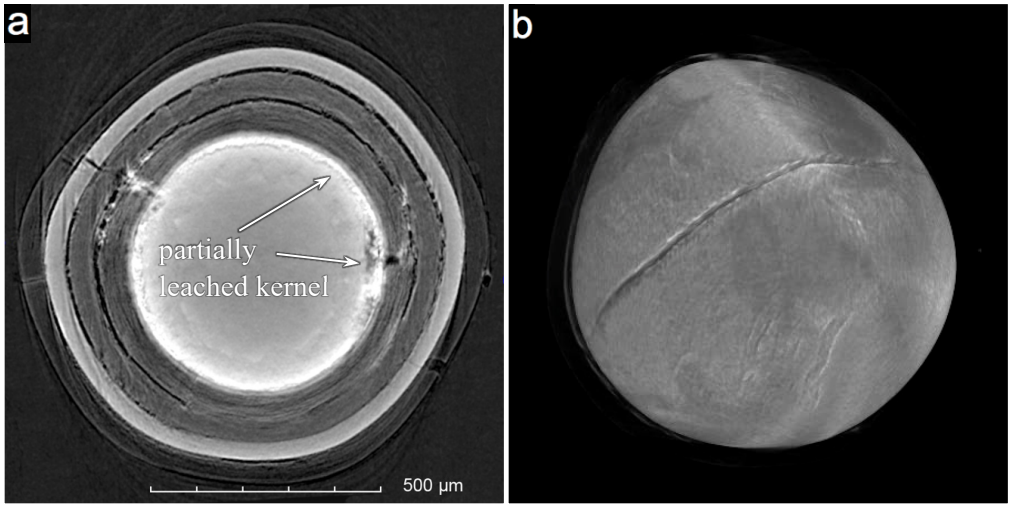

Figure 16. (a) X-ray tomogram of Particle 342-SP06 and (b) 3D representation of the SiC surface.

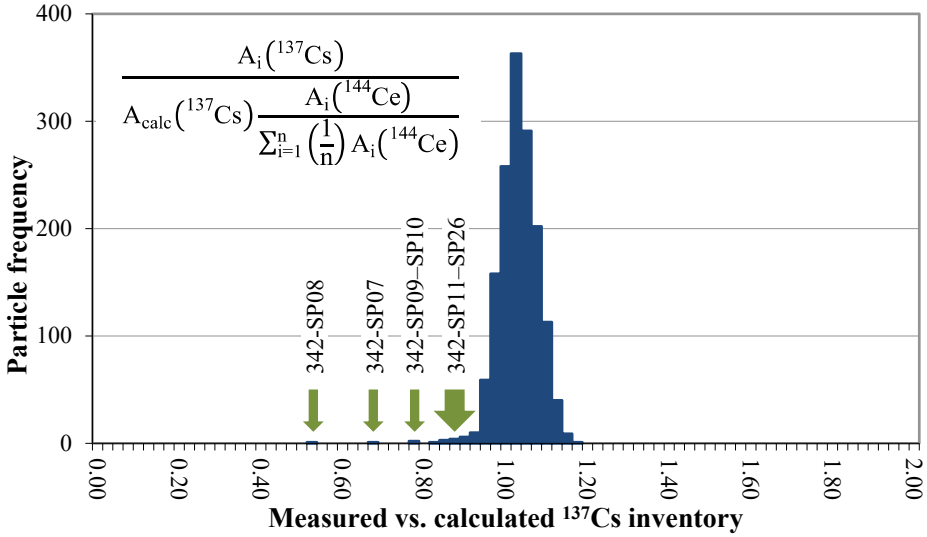

Figure 17. Measured vs. calculated ^{137}Cs inventory in 1,528 particles from Compact 3-4-2.

Because of the number of expected particles with failed SiC in 1700°C safety-tested Compact 3-4-1, the standard DLBL procedure was modified to minimize the steps before sieving out particles for an IMGA survey, as discussed in ORNL/TM-2020/1612 (Hunn et al. 2020). However, the 4.56 particle equivalents of ^{238}U measured in the first matrix postburn leach (Table 3) indicated that kernels were still exposed during the deconsolidation and acid digestion of the matrix. Five particles with obviously missing kernel material were found with the IMGA survey. X-ray tomograms of two of these particles are shown in Figure 18. In general, Compact 3-4-1 particles with leached kernels exhibited the same extensive CO corrosion and SiC cracking with the most extensive corrosion typically localized at an IPyC crack. The higher 1700°C safety test temperature resulted in a more extensive corrosion of the SiC and a greater volume of SiO_2 byproduct, as compared to the particles safety tested at 1600°C.

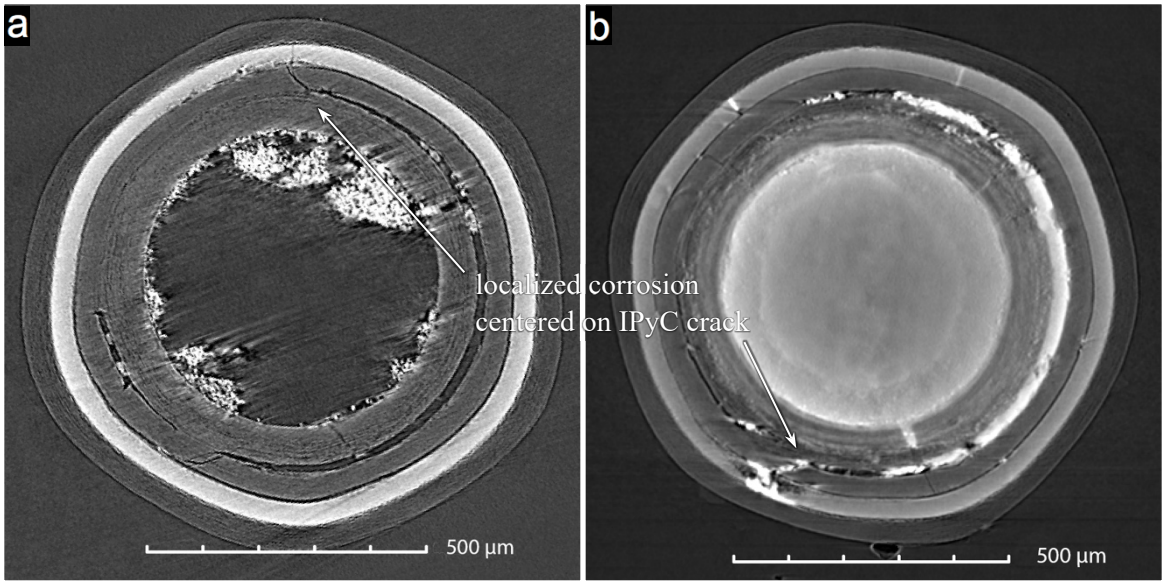

Figure 18. X-ray tomograms of (a) Particle 341-SP02 and (b) Particle 341-SP03.

Figure 19 shows the results of the IMGA survey of particles from Compact 3-4-1. The ^{137}Cs M/C histogram shows a large fraction of the particles had released ^{137}Cs. Five particles with normalized ^{137}Cs activities of 0.44–0.74 particle equivalents were imaged with XCT, as reported in ORNL/TM-2020/1612 (Hunn et al. 2020). Four had fractured IPyC, and two of these four showed clear evidence for general CO corrosion of the inside surface of the SiC layer. However, no obvious through-layer damage was observed. It is likely that the SiC layers in these particles had internal corrosion like that shown in Figure 20, which would have been below the ability of the XCT to resolve. Post-IMGA DLBL of the particles from Compact 3-4-1 resulted in the leaching of 2.27 particle equivalents of ^{238}U, which may have come from particles with failed SiC. However, many more particles with failed SiC were expected in the postburn particle leaches, based on the cesium release in the CCCTF and the cesium retained in the particles surveyed with the IMGA. Particles that release a significant fraction of their cesium inventory are classified as having *failed SiC*. However, some Compact 3-4-1 particles with SiC that was sufficiently degraded to release cesium may not have had damaged structures that were susceptible to oxidation during the burn. This appeared to be the case for many low-cesium particles analyzed from Compact 3-4-1.

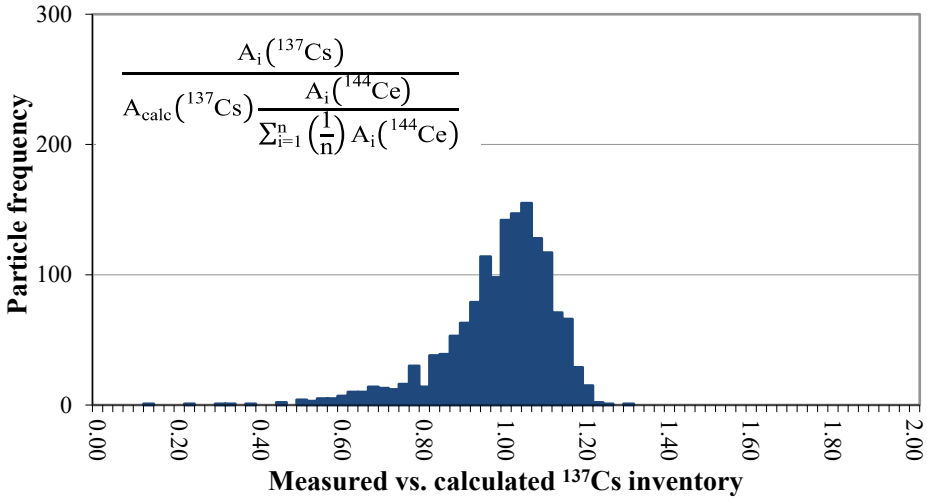

Figure 19. Measured vs. calculated ^{137}Cs inventory in 1,509 particles from Compact 3-4-1.

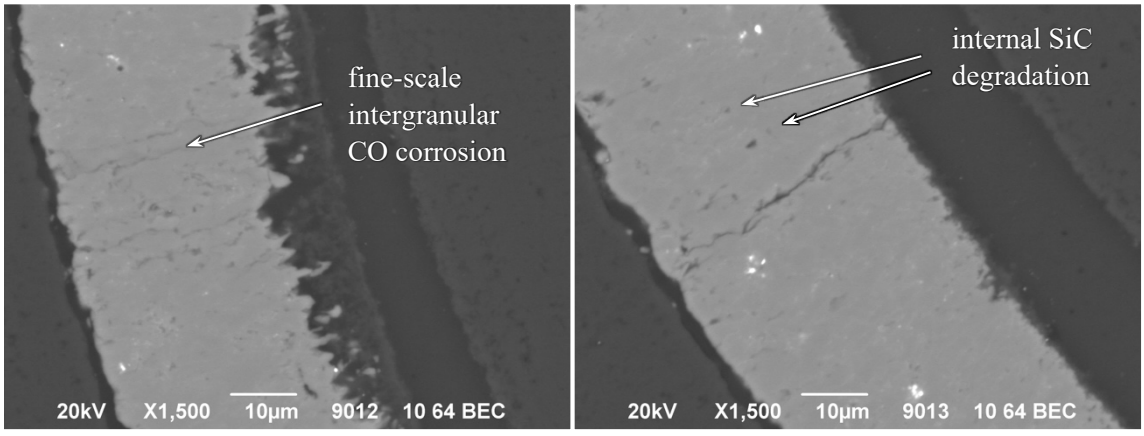

Figure 20. BEC images of SiC corrosion and degradation in Particle 341-SP01.

2.1.1.3 Conclusions

Safety testing and destructive PIE have been completed on six of the AGR-2 Capsule 3 UO_2 compacts. Compacts 3-1-2 and 3-3-1 were examined in the as-irradiated state. The DLBL analysis of the as-irradiated compacts indicated that there were no particles with defective or radiation-failed SiC or TRISO. A particle in Compact 3-1-2 was leached partway through the DLBL process, which indicated damage to the TRISO coating due to the analysis. Nondestructive three-dimensional imaging of this particle with XCT suggested that the SiC and OPyC layers had been broken because they were weakened by the fracture in the buffer and IPyC layers during irradiation. Separation of the IPyC from the SiC during irradiation had introduced cracks in the SiC that did not penetrate the layer; however, these cracks likely made the SiC more susceptible to handling damage during PIE. No particles were damaged during the DLBL of Compact 3-3-1, so this compact provided a good baseline for exposed actinides and fission products in the as-irradiated fuel.

Compact 3-1-1 was safety tested by heating in helium to 1500°C and holding at that temperature for ~400 hours, in which the planned 300-hour test was extended by 100 hours because of an uptick in the previously negligible cesium release rate after 256 hours at 1500°C. The amount of cesium that was released during the Compact 3-1-1 safety test and the time dependence of the cesium release rate were consistent with the presence of one particle with failed SiC. Compacts 3-3-2 and 3-4-2 were safety tested at 1600°C for ~300 hours. The fraction of particles with failed SiC was dramatically higher at 1600°C than at 1500°C. The SiC failure fractions in these two UO_2 compacts were also noticeably higher than AGR-1 and AGR-2 UCO compacts tested under similar conditions (Demkowicz et al. 2016; Hunn et al. 2018). In fact, UO_2 compact failure fractions were closer to the UCO compact failure fractions observed in AGR-1 fuel at 1800°C. Compact 3-4-1 was originally planned for safety testing at 1800°C, but concern about the higher UO_2 compact failure fractions at 1600°C resulted in a decision to reduce the test temperature to 1700°C. Cesium release began soon after reaching 1700°C, and a dramatically escalating rate of release, which reached one particle equivalent of ^{134}Cs per hour after ~100 hours, indicated wholesale SiC failure that forced a premature termination of the test. The release of other fission products typically monitored during safety testing (^{90}Sr, ^{110m}Ag, and ^{154}Eu) was dominated by a SiC failure at 1,600 and 1700°C. At 1500°C, the ^{110m}Ag release was consistent with the release of silver previously released through good SiC during irradiation, in which the silver had been temporarily sequestered in the matrix or OPyC until heating above the irradiation temperature during safety testing.

It was notable that no ^{85}Kr release from TRISO failure was observed in conjunction with the numerous SiC failures in the AGR-2 UO_2 compacts safety tested at 1600 and 1700°C. A similar situation was observed in AGR-1 PIE, even during 1800°C safety testing, in which as many as 11 particles in AGR-1 UCO Compact 3-2-3 exhibited cesium release from SiC failure (Hunn et al. 2014a). In AGR-1 PIE, krypton retention in particles with failed SiC was credited to intact OPyC layers. That appeared to be the case for the UO_2 fuel as well. In many of the failed SiC particles that later experienced kernel leaching during DLBL, the leaching appeared to be related to the post-test fracture of the OPyC, and the OPyC cracks often appeared remote and unrelated to the cracks in the underlying SiC.

The IMGA survey of particles from the safety-tested compacts identified and separated many of the particles with failed SiC from particles with intact SiC, including those missing most of their kernel material due to acid infiltration during DLBL. In those particles, although most of the kernel was removed, the particle layers remained in one piece because cracks in the coatings did not circumnavigate the entire particle sphere. Particles with leached kernels tended to be those with the most advanced SiC failure. Failure was localized, and in almost every instance SiC degradation could be directly associated with an IPyC crack that had exposed the inner surface of the SiC. These IPyC cracks did not appear to be caused by inherent insufficiencies in the IPyC layer, but were rather related to cracks propagating from, or initiated by, the detachment of the buffer near the buffer/IPyC interface. These connected events were previously identified as the primary failure mechanism in AGR-1 UCO TRISO fuel (Hunn et al. 2014b), with one exception. Degradation of the exposed SiC layer in UCO fuel was dominated by palladium

silicide formation, while degradation of the exposed SiC layer in UO_2 fuel was dominated by CO corrosion. The absence of CO corrosion in the UCO fuel was due to the addition of uranium carbide to the kernel, which reduced CO formation because the oxidation potential of uranium carbide is lower than carbon (Homan et al. 1977).

CO corrosion was clearly identified during SEM/EDS analysis of failed particles by the presence of intergranular corrosion and the formation of SiO_2 precipitates, which tended to agglomerate in the void space within the particles (e.g., the buffer/IPyC gap). In addition to localized CO corrosion through the entire thickness of the SiC layer, general CO corrosion was often observed in safety-tested particles that had a separation between the IPyC and SiC layers. In some cases, the detachment of the IPyC layer could be related to the layer mechanically pulling away from the SiC as a result of IPyC fracture adjacent to attached buffer, in which the continued shrinkage in the buffer pulled the IPyC inward. However, it could also be argued that the SiC corrosion may have occurred before, or in conjunction with, the IPyC separation. The connection between the IPyC and SiC layers is usually strong in TRISO particles due to a mechanical stitching of the two layers, in which fingers of SiC penetrate into the open porosity at the IPyC surface during the SiC deposition. Chemical corrosion at this interface could have either caused an eventual separation as the reaction progressed or weakened the interface bond to the point where it became susceptible to mechanical separation.

The connection between CO corrosion and particles with failed SiC was obvious for those particles with advanced locally corroded SiC, in which the corroded region fully penetrated the layer, or thinned it to a state where it eventually cracked. General corrosion was not as obviously related to SiC failure but likely compromised the SiC and apparently led to fracture in some particles. However, not every special particle with a preferential loss of cesium during safety testing had obvious through-layer cracks or enough corrosion of the SiC to allow observation of the cesium release pathway, especially those particles from Compacts 3-4-2 and 3-4-1 with lower cesium release. Nevertheless, particles with a preferential loss of cesium were commonly found to have abnormal microstructures and indicators of corrosion, which suggested there was a correlation between the cesium release and observed abnormal microstructures that was not coincidental.

2.1.1.4 References

Demkowicz, Paul A., Edward L. Reber, Dawn M. Scates, Les Scott, and Blaise P. Collin. 2015. "First High Temperature Safety Tests of AGR-1 TRISO Fuel with the Fuel Accident Condition Simulator (FACS) Furnace." *J. Nucl. Mater.* 464: 320–330.

Demkowicz, Paul A., John D. Hunn, David A. Petti, and Robert N. Morris. 2016. "Key results from irradiation and post-irradiation examination of AGR-1 UCO TRISO fuel." *Proc. 8th International Topical Meeting on High Temperature Reactor Technology (HTR-2016)*. Las Vegas, November 6–10, 2016. Also published in *Nucl. Eng. Des*. 329: 102–109.

Hawkes, Grant L. 2014. *AGR-2 Daily As-Run Thermal Analyses.* INL/ECAR-2476, Revision 1. Idaho Falls: Idaho National Laboratory.

Homan, Franklin J., Terrence B. Lindemer, Ernest L. Long, Jr., Terry N. Tiegs, and Ronald L. Beatty. 1977. "Stoichiometric Effects on Performance of High-Temperature Gas-Cooled Reactor Fuels from the U-C-O System." *Nucl. Tech.* 35: 428–441.

Hunn, John D., Fred C. Montgomery, and Peter J. Pappano. 2010. *Data Compilation for AGR-2 UO_2 Compact Lot LEU11-OP2-Z.* ORNL/TM-2010/055, Revision 1. Oak Ridge: Oak Ridge National Laboratory.

Hunn, John D., Robert N. Morris, Charles A. Baldwin, Fred C. Montgomery, and Tyler J. Gerczak. 2014a. *PIE on Safety-Tested AGR-1 Compacts 5-3-3, 5-1-3, and 3-2-3*. ORNL/TM-2014/484, Revision 0. Oak Ridge: Oak Ridge National Laboratory.

Hunn, John D., Charles A. Baldwin, Tyler J. Gerczak, Fred C. Montgomery, Robert N. Morris, Chinthaka M. Silva, Paul A. Demkowicz, Jason M. Harp, Scott A. Ploger, Isabella J. van Rooyen, and Karen E. Wright. 2014b. "Detection and Analysis of Particles with Failed SiC in AGR-1 Fuel Compacts." *Proc. 7th International Topical Meeting on High Temperature Reactor Technology (HTR-2014)*. Weihai, October 27–31, 2014. Also published in *Nucl. Eng. Des.* 360: 36–46.

Hunn, John D., Robert N. Morris, Fred C. Montgomery, Tyler J. Gerczak, Darren J. Skitt, Charles A. Baldwin, John A. Dyer, Grant W. Helmreich, Brian D. Eckhart, Zachary M. Burns, Paul A. Demkowicz, and John D. Stempien. 2018. "Post-Irradiation Examination and Safety Testing of US AGR-2 Irradiation Test Compacts." *Proc. 9th International Topical Meeting on High Temperature Reactor Technology (HTR-2018)*. Warsaw, October 8–10, 2018.

Hunn, John D., Tyler J. Gerczak, Robert N. Morris, Fred C. Montgomery, Darren J. Skitt, Grant W. Helmreich, Brian D. Eckhart, and Charles A. Baldwin. 2020. *Destructive PIE and Safety-Testing of Six AGR-2 UO_2 Capsule 3 Compacts*. ORNL/TM-2020/1612, Revision 0. Oak Ridge: Oak Ridge National Laboratory.

Hunn, John D., and Fred C. Montgomery. 2020. *Data Acquisition Method: Leach-Burn-Leach Analysis of Irradiated Fuel Compacts Using a Soxhlet Extractor in the 3525 Hot Cell*. AGR-CHAR-DAM-37, Revision 4. Oak Ridge: Oak Ridge National Laboratory.

Sterbentz, James W. 2014. *JMOCUP As-Run Daily Depletion Calculation for the AGR-2 Experiment in the ATR B-12 Position.* ECAR-2066, Revision 2. Idaho Falls: Idaho National Laboratory.

2.1.2 Radial Deconsolidation and LBL of AGR-3/4 Compacts 1-4 and 10-4

Ongoing PIE of the AGR-3/4 compacts includes the radial deconsolidation of individual compacts to segment the compacts into separate collections of particles and matrix debris from concentric cylindrical volumes, each of which can be subjected to a leach-burn-leach (LBL) analysis to quantify the presence of actinides and fission products released by the driver fuel and designed-to-fail (DTF) particles. Table 4 shows the calculated irradiation conditions for two compacts subjected to radial deconsolidation and LBL at ORNL in FY 2020. Detailed results were reported in a FY 2020 deliverable report (Hunn et al. 2020), and excerpts from that report are summarized herein. Compact 1-4 was from the capsule located at the bottom of the test train and experienced burnup and temperatures near the lower end of the ranges for compacts in the AGR-3/4 irradiation test. Compact 10-4 experienced irradiation burnup and temperatures near the middle of the ranges and was safety tested prior to DLBL (Stempien et al. 2018).

Table 4. Irradiation and safety test parameters for two AGR-3/4 compacts subjected to radial DLBL.

Compact [a]	Safety test (°C)	Burnup [b] (% FIMA)	Fast fluence [b] (n/m^2)	Temperature [c] (°C)		
				TAVA	TA_{min}	TA_{max}
AGR-3/4 Compact 1-4	none	6.85	2.10×10^{25}	929	866	972
AGR-3/4 Compact 10-4	1400	11.43	3.75×10^{25}	1168	1079	1231

[a] The compact identification denotes the compact's location in the irradiation test train: *capsule-level*.

[b] Compact average burnups and fast neutron fluences ($E_n > 0.18$ MeV) are based on daily depletion calculations (Sterbentz 2015).

[c] Compact temperatures are based on thermal calculations (Hawkes 2016).

2.1.2.1 Compact 1-4

Compact 1-4 was radially deconsolidated in three stages to remove three cylindrical rings of driver fuel particles and matrix, leaving a cylindrical core encompassing the DTF particles. The core was then axially deconsolidated. At the end of each radial deconsolidation, images were acquired of the compact to measure the residual diameter. At least 50 photos were acquired of the rotating compact. The number of photos was based on analysis of the distribution of rotations presented to the camera, in which 40–50 images acquired at a varying capture rate was determined to provide sufficient randomness in the compact orientation. Table 5 shows the segment dimensions and volumes as determined by an automated image analysis of the photos, as discussed in ORNL/TM-2020/1707 (Hunn et al. 2020).

Table 5. Segment results for Compact 1-4 measured with automated photo analysis.

Quantity	Segment 1	Segment 2	Segment 3	Segment 4
Initial diameter (mm)	12.23	11.02	9.28	6.55
Residual diameter (mm)	11.02	9.28	6.55	0
Segment thickness (mm)	0.60	0.87	1.37	solid
Segment volume (cm^3)	0.274	0.346	0.423	0.420

Photos of the compact at each stage in the process are shown in Figure 21. Material removal was relatively uniform along the length and around the circumference of the compact with respect to the average driver fuel particle diameter of 0.819 mm (Hunn and Lowden 2007). The residual diameter of the compact after the radial deconsolidation of Segment 3 was close to the outer diameter of the stainless-steel tube used as a drive axle for compact rotation. The axle diameter of 6 mm presented a practical limit to the outer diameter of the solid core segment. This diameter was more than sufficient to ensure that any residuals of the DTF particles that remained in their original location (<1.5 mm from the compact axis) were located within the core (Hunn et al. 2012).

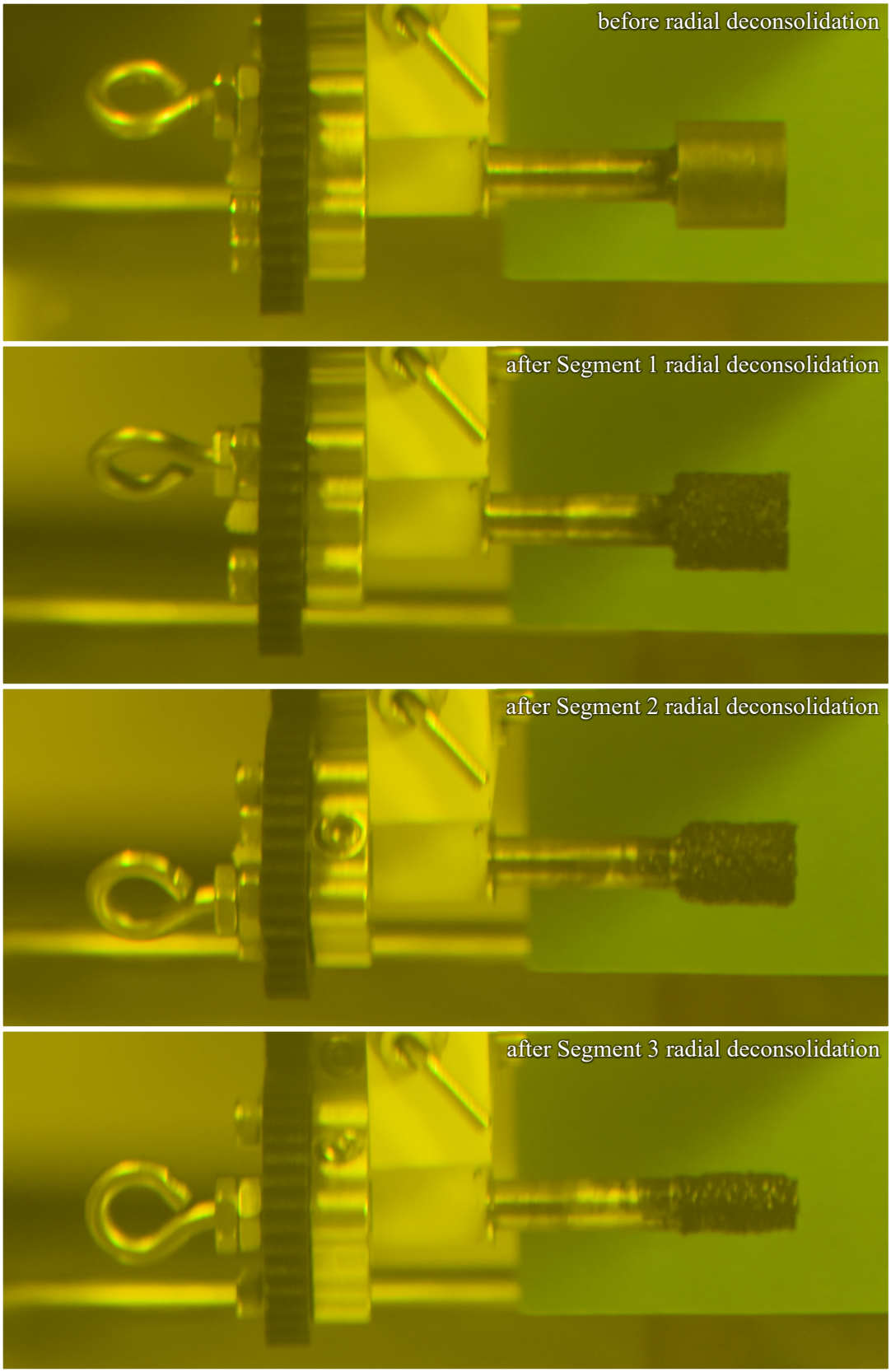

Figure 21. Compact 1-4 at each stage of radial deconsolidation.

After completion of the radial deconsolidation of each compact segment, the particles, matrix debris, and acid were transferred to a labeled storage vial. The beaker was rinsed several times, and the rinse was also added to the storage vial. The contents of each storage vial were sequentially analyzed using the equipment and methods for LBL with a Soxhlet extractor developed for AGR-1 PIE (Hunn et al. 2013). The DLBL data for select actinides and fission products (both radionuclides and stable nuclides) are provided for each primary leach solution in ORNL/TM-2020/1707 (Hunn et al. 2020). Table 6 shows the particle equivalents of ^{144}Ce detected in each DLBL solution. The first postburn particle leach from Compact 1-4 Segment 1 had 1.07 particle equivalents of ^{144}Ce, which indicated that a kernel from a driver fuel particle was exposed, possibly due to damage to the TRISO coating during particle handling in the IMGA. The actinides and fission products from this exposed kernel dominated the Segment 1 first postburn particle leach results for the actinides and radionuclides. Therefore, the data from the Compact 1-4 Segment 1 postburn particle leaches should not be included in analyses focused on distribution of fission products from the DTF particles. The total ^{144}Ce detected in the DLBL, not including the Segment 1 postburn particle leaches, was 19.9 particle equivalents. This was consistent with the presence of 20 DTF particles, as expected for the AGR-3/4 compacts (Hunn et al. 2012). Most of the ^{144}Ce in each segment was detected in the deconsolidation acid, and there was a clear trend in the total amount detected in each concentric cylindrical segment, which progressively decreased moving away from the core segment. This progression is shown graphically in Figure 22 in terms of the number of DTF particle equivalents detected in each segment.

Table 6. Particle equivalents of ^{144}Ce detected in Compact 1-4 DLBL solutions.

DLBL Step	Segment 1	Segment 2	Segment 3	Segment 4	Total
Deconsolidation acid	(0.075)	(0.655)	(0.938)	(17.332)	(19.000)
Preburn leach 1	<(0.0041)	<(0.0031)	<(0.0047)	(0.143)	(0.143)
Preburn leach 2	<(0.006)	<(0.007)	<(0.015)	(0.054)	(0.054)
Postburn matrix leach 1	(0.0064)	(0.0067)	(0.0047)	(0.165)	(0.183)
Postburn matrix leach 2	<(0.0017)	<(0.003)	<(0.0032)	(0.0047)	(0.0047)
Postburn particle leach 1	(1.073)	<(0.037)	<(0.020)	(0.553)	(1.626)
Postburn particle leach 2	<(0.0081)	<(0.0068)	<(0.0083)	<(0.0086)	(0.000)
Pre-IMGA subtotal	(0.081)	(0.662)	(0.943)	(17.700)	(19.385)
Post-IMGA subtotal	(1.073)	(0.000)	(0.000)	(0.553)	(1.626)
Total	(1.154)	(0.662)	(0.943)	(18.253)	(21.011)
Total without shaded values	(0.081)	(0.662)	(0.943)	(18.253)	(19.938)

Note: Shaded values were associated with an exposed kernel from a driver fuel particle.

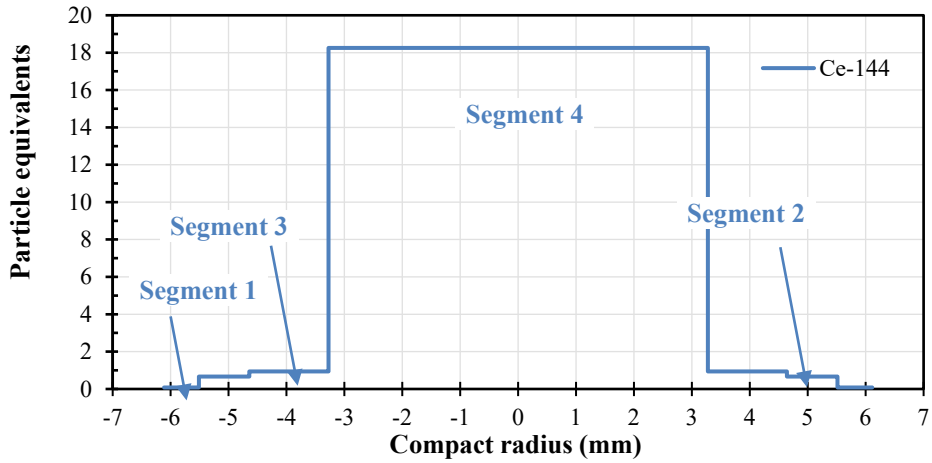

Figure 22. Distribution of ^{144}Ce from DTF particles in Compact 1-4.

For the analysis of the diffusion of each nuclide, it is useful to convert the data into average concentration in each segment by dividing the nuclide quantity in each segment by the segment volume. Figure 23 shows the ^{144}Ce data from Figure 22 scaled by the segment volumes in Table 5 and plotted on a logarithmic scale. The arbitrary trend line shows that the diffusion exhibited a roughly exponential nature, as might be expected, but the mathematical form of the concentration as a function of radius and the radial position in each segment that corresponded to the measured average concentration would have to be determined by further analysis beyond the scope of this report. The ^{144}Ce concentrations in Segment 2 and Segment 3 were similar, and Segment 2 did not align with the trend line in Figure 23. Figure 24 shows that the ^{137}Cs and ^{154}Eu concentrations exhibited the same peculiarity. Compared with ^{144}Ce, the ^{137}Cs and ^{154}Eu concentrations were higher in the outer three segments. This was consistent with expectations that cesium and europium should be more mobile at the irradiation temperatures experienced by Compact 1-4 (Table 1). Figure 25 provides a comparison of the ^{144}Ce, ^{235}U, and ^{239}Pu profiles. Cerium and uranium had similar profiles, while the plutonium transport out of Segment 1 appeared to be relatively slower.

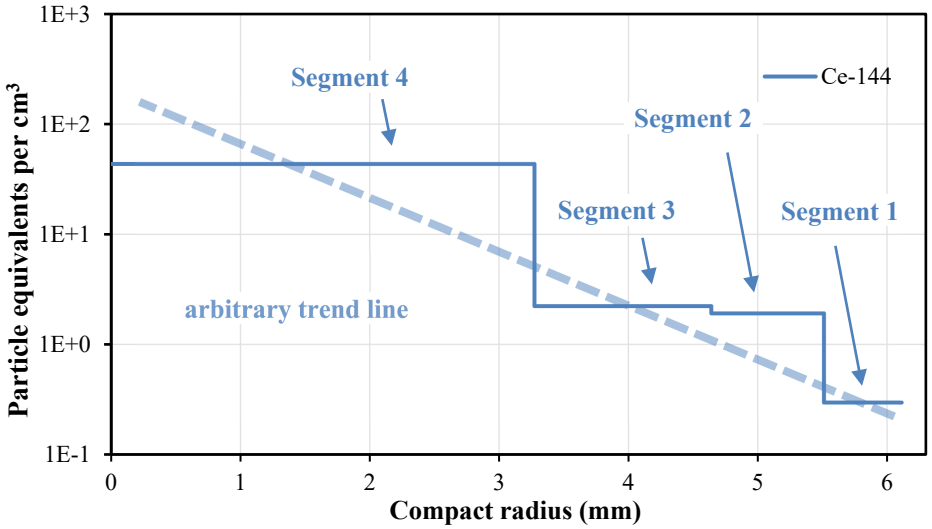

Figure 23. Concentration gradient of ^{144}Ce from DTF particles in Compact 1-4.

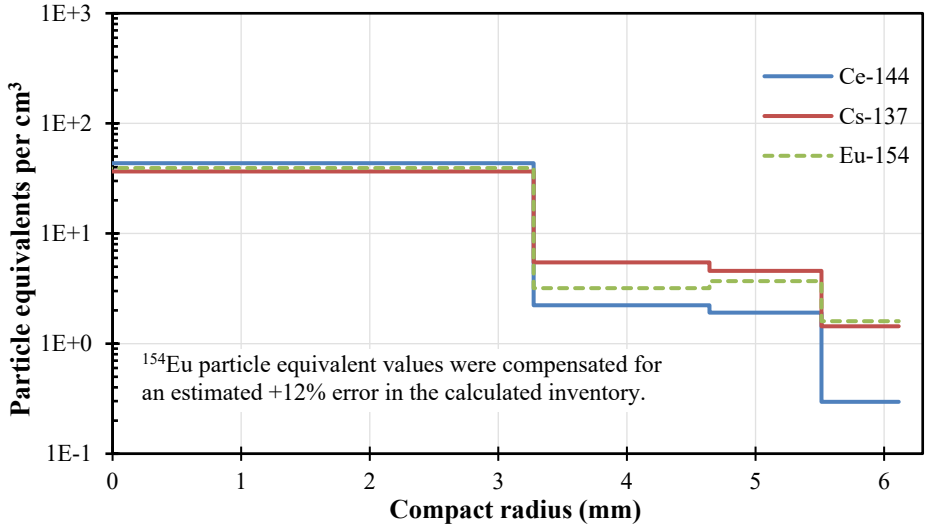

Figure 24. Comparison of ^{144}Ce, ^{137}Cs, and ^{154}Eu diffusion from DTF particles in Compact 1-4.

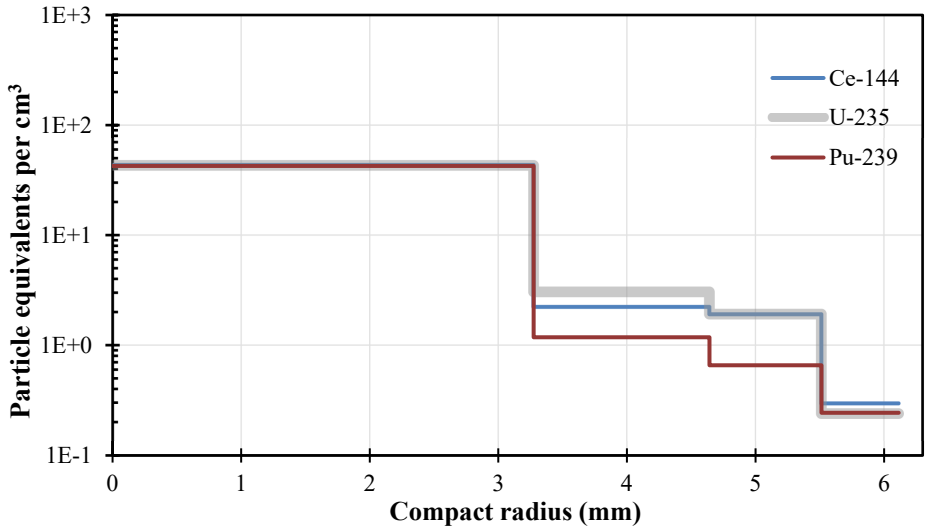

Figure 25. Comparison of ^{144}Ce, ^{235}U, and ^{239}Pu diffusion from DTF particles in Compact 1-4.

2.1.2.2 Compact 10-4

Compact 10-4 was radially deconsolidated in two stages to remove two cylindrical rings of driver fuel particles and matrix, leaving a cylindrical core encompassing the DTF particles, which was then axially deconsolidated. As was done for Compact 1-4, at least 50 photos were acquired of the rotating residual at the end of each radial deconsolidation. Table 7 shows the segment dimensions and volumes as determined by automated image analysis of the photos.

Table 7. Segment results for Compact 10-4 measured with automated photo analysis.

Quantity	Segment 1	Segment 2	Segment 3
Initial diameter (mm)	12.15	9.62	7.14
Residual diameter (mm)	9.62	7.14	0
Segment thickness (mm)	1.26	1.24	solid
Segment volume (cm^3)	0.54	0.41	0.50

Photos of the compact at each stage in the process are shown in Figure 26. As for Compact 1-4, material removal was relatively uniform along the length and around the circumference of the compact. After completion of the radial deconsolidation of each Compact 10-4 segment, the particles and matrix debris were subjected to the same DLBL process applied to the material from Compact 1-4. The DLBL data for select actinides and fission products (both radionuclides and stable nuclides) for each primary leach solution are provided in ORNL/TM-2020/1707 (Hunn et al. 2020). Table 8 shows the particle equivalents of ^{235}U detected in each DLBL solution. The total ^{235}U detected in the DLBL was 21.0 particle equivalents. This was consistent with the presence of 20 DTF particles. There is insufficient data to determine whether the apparent one "extra" particle equivalent was measurement uncertainty or a contribution from the Compact 1-4 driver fuel; it was likely the former, given the variation observed between the ^{235}U and ^{238}U isotopes as discussed in ORNL/TM-2020/1707 (Hunn et al. 2020). Most of the ^{235}U in each segment was detected in the deconsolidation acid, and there was a clear trend in the total amount detected in each concentric cylindrical segment, which progressively decreased moving away from the core segment. This progression is shown graphically in Figure 27 in terms of the number of DTF particle equivalents detected in each segment.

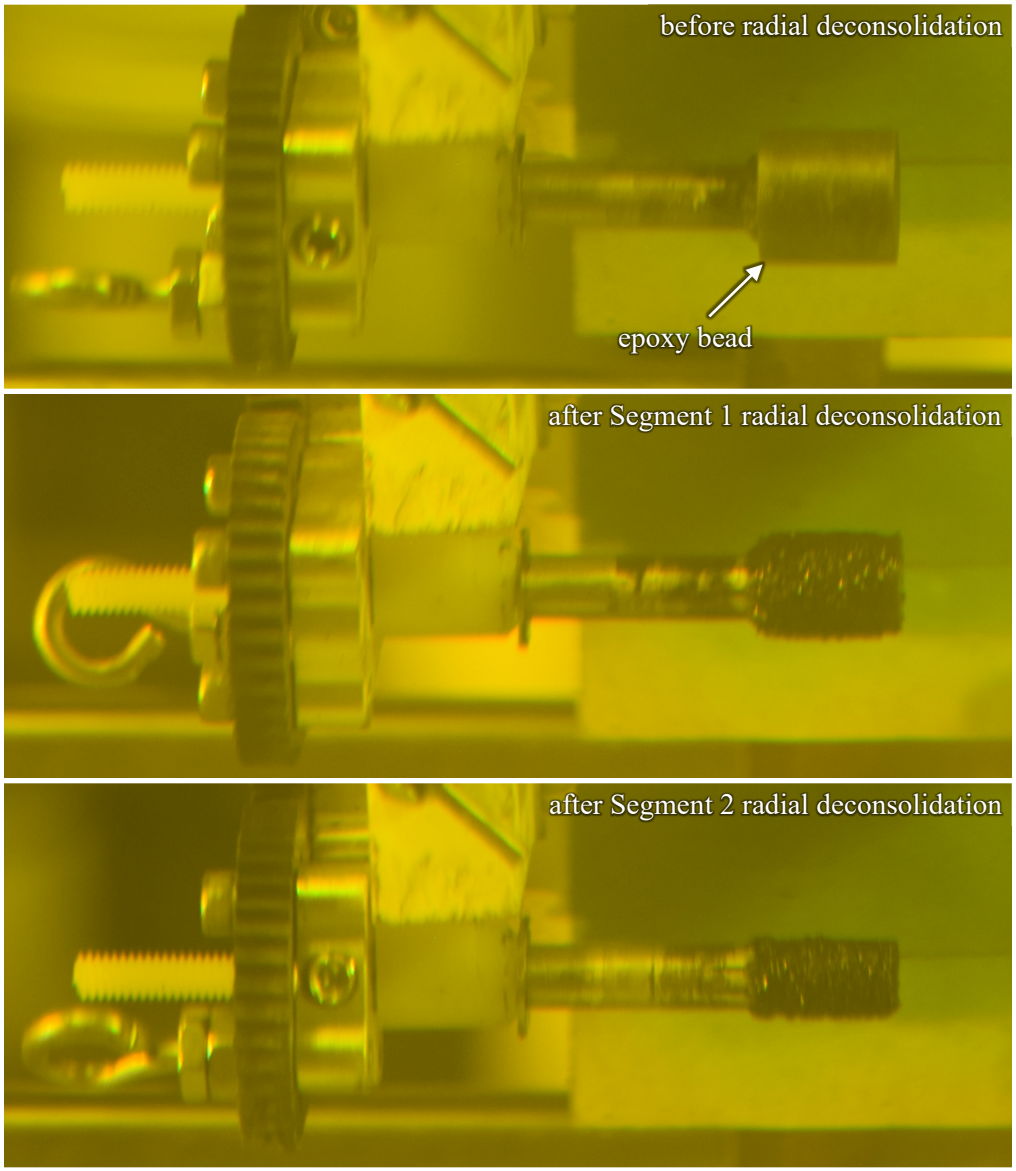

Figure 26. Compact 10-4 at each stage of radial deconsolidation.

Table 8. Particle equivalents of ^{235}U detected in Compact 10-4 DLBL solutions.

DLBL Step	Segment 1	Segment 2	Segment 3	Total
Deconsolidation acid	(0.188)	(0.830)	(19.416)	(20.433)
Preburn leach 1	(0.0013)	(0.016)	(0.342)	(0.360)
Preburn leach 2	(0.0009)	(0.0055)	(0.012)	(0.018)
Postburn matrix leach 1	(0.018)	(0.0083)	(0.050)	(0.077)
Postburn matrix leach 2	(0.0008)	(0.0021)	(0.0019)	(0.0048)
Postburn particle leach 1	(0.022)	(0.021)	(0.042)	(0.085)
Postburn particle leach 2	(0.0031)	(0.0021)	(0.014)	(0.019)
Pre-IMGA subtotal	(0.209)	(0.862)	(19.822)	(20.893)
Post-IMGA subtotal	(0.025)	(0.023)	(0.056)	(0.104)
Total	(0.234)	(0.885)	(19.878)	(20.997)

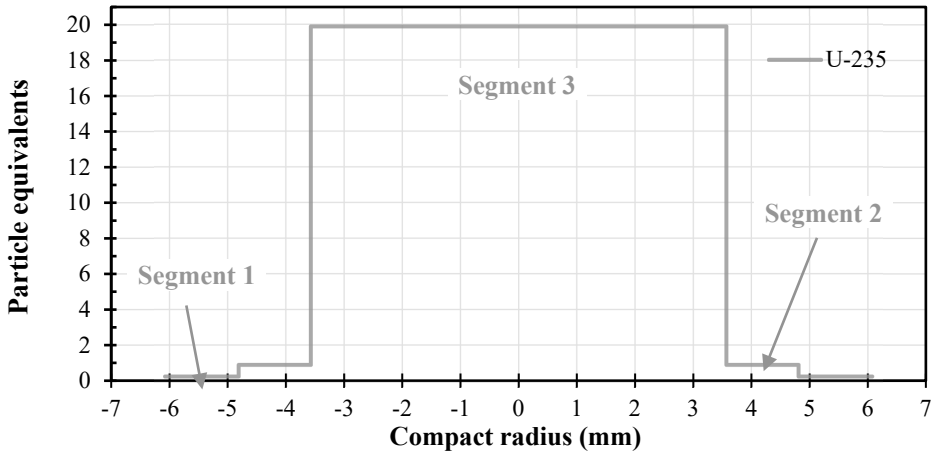

Figure 27. Distribution of ^{235}U from DTF particles in Compact 10-4.

Figure 28 shows the ^{235}U data from Figure 27 scaled by the segment volumes in Table 7 and plotted on a logarithmic scale. Like Compact 1-4, the arbitrary trend line shows that the diffusion exhibited a roughly exponential nature, as might be expected, but the mathematical form of the concentration as a function of radius and the radial position in each segment that corresponded to the measured average concentration would have to be determined by further analysis beyond the scope of this report. Figure 29 provides a comparison of the ^{144}Ce, ^{235}U, and ^{239}Pu profiles. Uranium and plutonium had similar profiles, while cerium transport appeared to be relatively slower. Figure 30 shows that ^{137}Cs and ^{154}Eu exhibited indications of more active diffusion, with a noticeable depletion of their total inventory and higher concentration in the outer two segments. The ^{137}Cs and ^{154}Eu concentrations were also higher in the outer three segments from Compact 1-4 (Figure 24), but the depletion in the core segment was less severe. These differences were most likely related to the fact that Compact 10-4 was irradiated at a higher temperature and safety tested at 1400°C after the irradiation (Table 1). Table 9 shows the particle equivalents of these nuclides measured with DLBL in each segment.

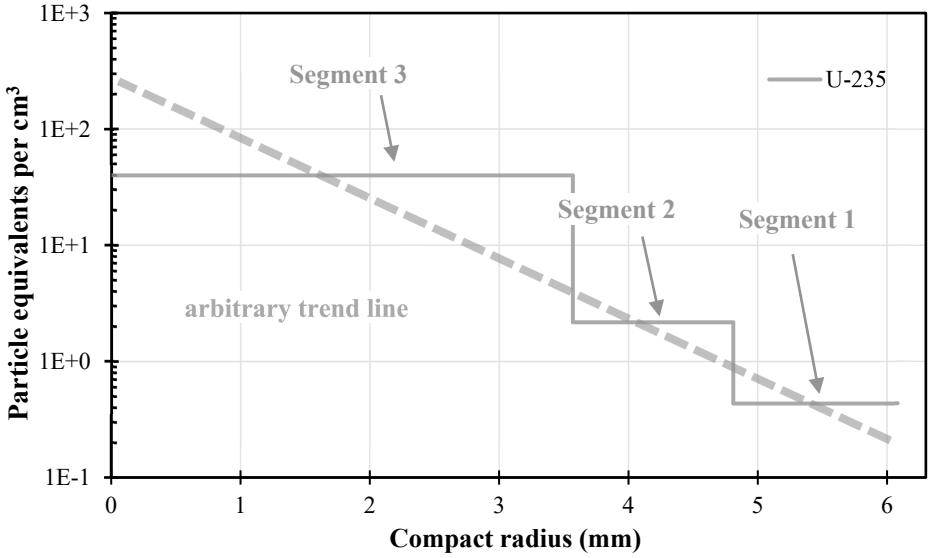

Figure 28. Concentration gradient of ^{235}U from DTF particles in Compact 10-4.

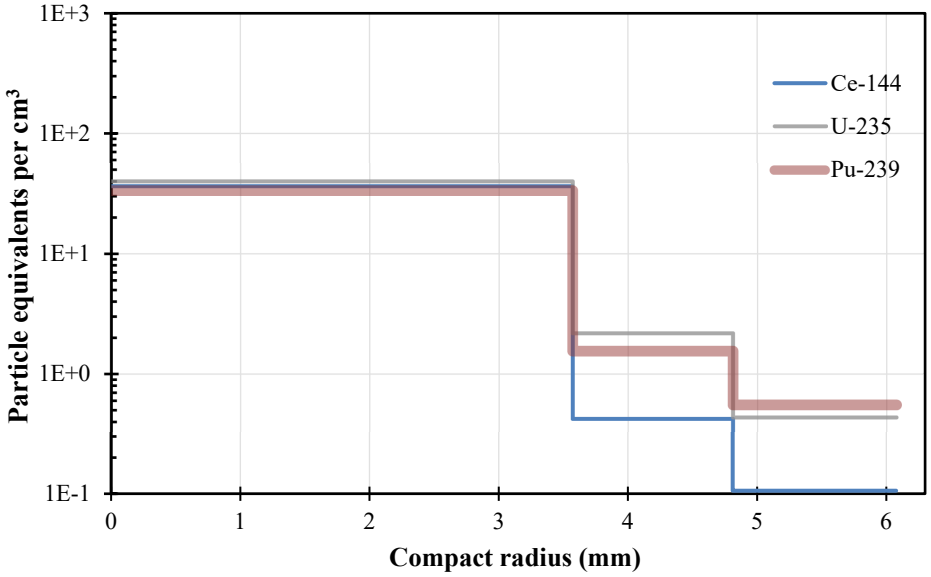

Figure 29. Comparison of ^{144}Ce, ^{235}U, and ^{239}Pu diffusion from DTF particles in Compact 10-4.

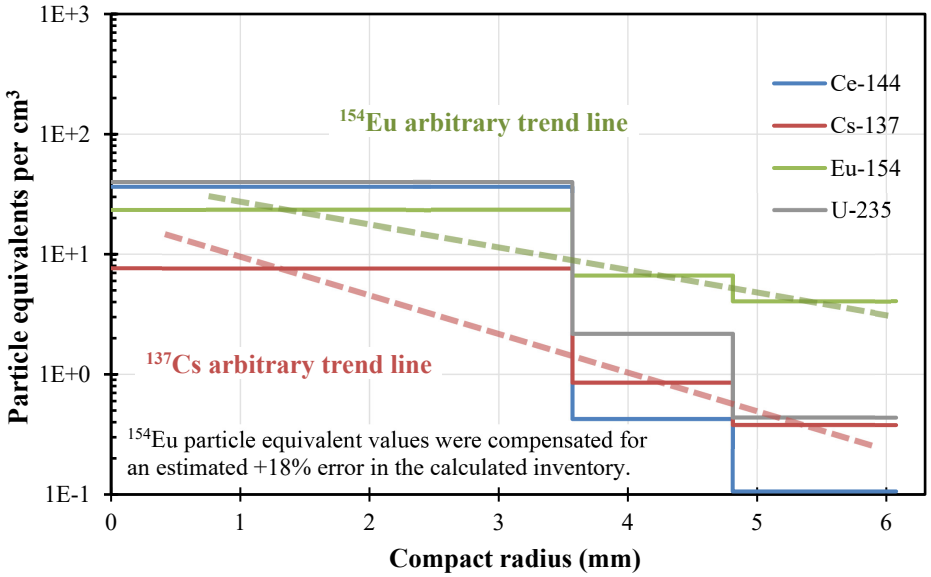

Figure 30. Comparison of ^{144}Ce, ^{137}Cs, and ^{154}Eu diffusion from DTF particles in Compact 10-4.

Table 9. Comparison of particle equivalents of select nuclides in Compact 10-4 segments.

Nuclide	Segment 1	Segment 2	Segment 3	Total
^{235}U	(0.234)	(0.885)	(19.878)	(20.997)
^{144}Ce	(0.057)	(0.172)	(18.139)	(18.368)
^{239}Pu	(0.298)	(0.630)	(16.653)	(17.581)
^{90}Sr	(1.973)	(2.452)	(9.915)	(14.341)
^{154}Eu [a]	(1.850)	(2.291)	(9.834)	(13.975)
^{137}Cs	(0.203)	(0.346)	(3.806)	(4.356)

[a] Values for 154Eu were adjusted for offset in calculated inventory

2.1.2.3 References

Hawkes, Grant L. 2016. *AGR-3/4 Daily As-Run Thermal Analyses.* INL/ECAR-2807, Revision 1. Idaho Falls: Idaho National Laboratory.

Hunn, John D., and Richard A. Lowden. 2007. *Data Compilation for AGR-3/4 Driver Coated Particle Composite LEU03-09T*. ORNL/TM-2007/019, Revision 0. Oak Ridge: Oak Ridge National Laboratory.

Hunn, John D., Richard A. Lowden, James H. Miller, Brian C. Jolly, Michael P. Trammell, Andrew K. Kercher, Fred C. Montgomery, and Chinthaka M. Silva. 2012. "Fabrication and Characterization of Driver Fuel Particles, Designed-to-Fail Fuel Particles, and Fuel Compacts for the US AGR-3/4 Irradiation Test." *Proc. 6th International Topical Meeting on High Temperature Reactor Technology (HTR-2012)*. Tokyo, October 28–November 1, 2012. Also published in *Nucl. Eng. Des.* 271: 123–130.

Hunn, John D., Robert N. Morris, Charles A. Baldwin, Fred C. Montgomery, Chinthaka M. Silva, and Tyler J. Gerczak. 2013. *AGR-1 Irradiated Compact 4-4-2 PIE Report: Evaluation of As-Irradiated Fuel Performance with Leach Burn Leach, IMGA, Materialography, and X-ray Tomography*. ORNL/TM-2013/236, Revision 0. Oak Ridge: Oak Ridge National Laboratory.

Hunn, John D., Fred C. Montgomery, Darren J. Skitt, and Grant W. Helmreich. 2020. *Radial Deconsolidation and Leach-Burn-Leach of AGR-3/4 Compacts 1-4 and 10-4*. ORNL/TM-2020/1707, Revision 0. Oak Ridge: Oak Ridge National Laboratory.

Stempien, John D., Paul A. Demkowicz, Edward L. Reber, and Cad L. Christensen. 2018. "Preliminary Results from the First Round of Post-Irradiation Heating Tests of Fuel Compacts from the AGR-3/4 Irradiation." *Proc. 9th International Topical Meeting on High Temperature Reactor Technology (HTR-2018)*. Warsaw, October 8–10, 2018.

Sterbentz, James W. 2015. *JMOCUP As-Run Daily Depletion Calculation for the AGR-3/4 TRISO Particle Experiment in ATR Northeast Flux Trap.* ECAR-2753, Revision 1. Idaho Falls: Idaho National Laboratory.

2.1.3 UCO Fuel Kernel Examinations by Advanced Microscopic Methods

2.1.3.1 Unirradiated Particles

Two materialographic mounts, each with three unirradiated AGR TRISO particles, were received from ORNL. Particles F52-LEU09 and F51-LEU01-49T are AGR-2 and AGR-1 particles, respectively. These TRISO fuel particles were previously compacted and heat treated at 1800 ºC for one hour before being deconsolidated from the compact matrix and mounted and polished to obtain TEM thin foils from their cross sections. A total of 16 TEM specimens were prepared from various locations of two unirradiated AGR particles. From each particle, five TEM lamellae were lifted out from different locations of the fuel kernel, and three TEM lamellae were taken from the SiC layer and its interfaces. The locations of lamellae taken from the kernel of particle F52-LEU-09 are shown in Figure 31. Among these lamellae, a total of two TEM lamellas, obtained from each particle, have been shipped to the Irradiated Materials Characterization Laboratory for electron energy-loss spectroscopy (EELS) analysis to quantify the low atomic number elements (carbon and oxygen). Another 14 lamellae have been sent to the Center for Advanced Energy Studies for TEM examination focusing on phase analysis and chemical identification.

In this quarterly report, a brief overview will be provided of the TEM data obtained from the lamella taken from the center of the particle F52-LEU-09 fuel kernel (shown in Figure 31). The data analysis mainly focused on extracting both structural and chemical information from the phases present in the TEM lamellae.

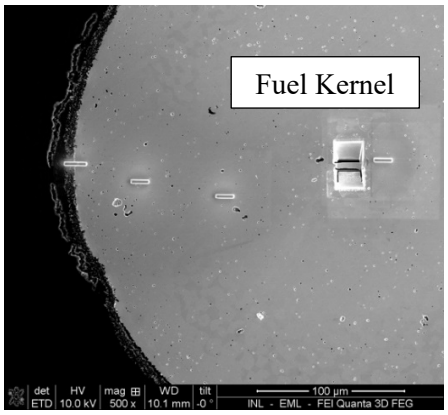

Figure 31. TEM specimen locations from unirradiated AGR TRISO mounts.

TEM of Kernel Center of Unirradiated AGR-2 Particle (F52-LEU-09)

Low magnification scanning transmission electron microscopy (STEM) images collected from this lamella are provided in Figure 32. The TEM sample has two distinct grain types. One kind of grain has pores distributed without any other contrasting features, hereafter referred to as F52-region A. The other kind of grain has bright streak-like features distributed locally, and small pores are only sporadically visible in Figure 32. This location is hereafter referred to as F52-region B. The lamella was tilted to different zone axis conditions for each of these grains to get crystal structure information. Figure 33 shows diffraction patterns from these grains, and circles highlight the corresponding locations from where these patterns were recorded. We note that the area of the circles on the STEM images approximately represent the area covered by the selected area diffraction aperture, indicating that the diffraction pattern has signal contributions from the phases within the circled regions.

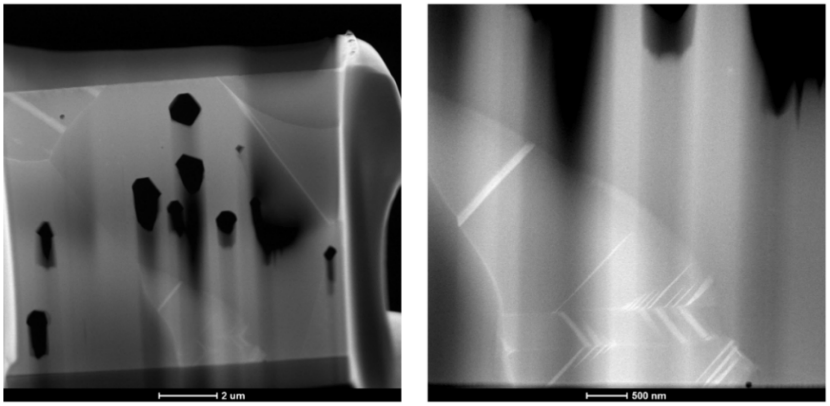

Figure 32. Low magnification STEM images of TEM lamella.

The zone axis diffraction patterns from F52-region A, given in Figure 33, are indexed with [1 0 3] and [1 1 2] diffraction patterns of the face-centered-cubic UO_2 phase for two different tilting conditions. The EDS spectrum profile obtained from this region shows equally strong peaks of O and C in addition to U peaks. It indicates that UO_2 is the main phase present in this region with some C in the structure. Similarly, some representative diffraction patterns recorded from F52-regions B are provided in Figure 34. The sample region outside the bright band-like features is indexed with [1 1 1] zone axis diffraction pattern of a body-centered tetragonal (BCT) UC_2 phase. Furthermore, the diffraction pattern collected only from the bright band-like feature can be indexed the [1 1 1] zone axis pattern of BCT UC_2 phase as shown Figure 34. It shows that the grain matrix and the bright band-like structure have similar BCT UC_2 structure. However, in some instances, they exhibit a twinned structure where the diffracting

points are split for certain crystallographic planes. On the other hand, the diffraction patterns along other orientations [1 1 1] and [1 0 1] collected from the regions with and without the bright features are similar and show no split diffraction points, indicating an absence of crystallographic rotation in the bright feature along these orientations. Some additional analysis is needed to ascertain the characteristics of the twin structure. The EDS spectra collected in F52-region B – both inside and outside the band structure – are similar and reveal major C and U peaks, indicating that there is no compositional difference between them.

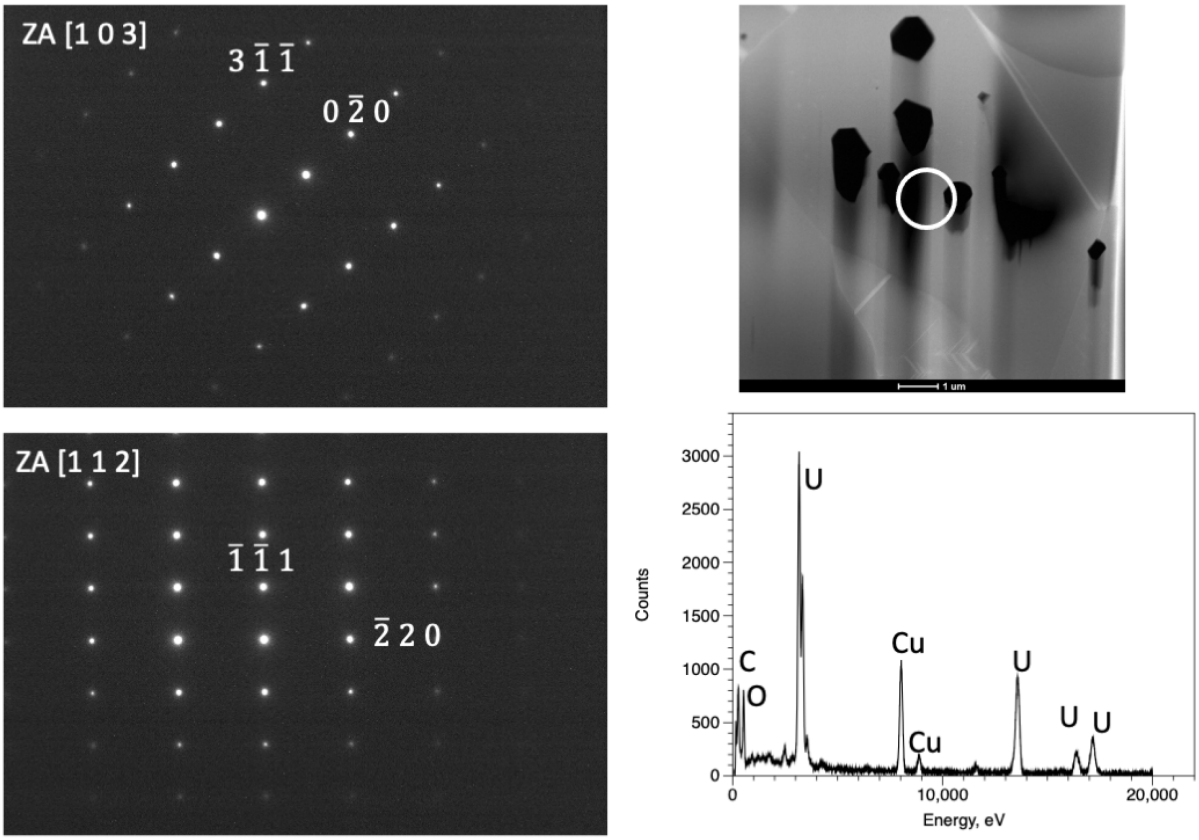

Figure 33. Zone axis diffraction patterns recorded from the circled region of the STEM image in two different sample tilting conditions. The diffraction patterns are indexed with face-centered-cubic UO_2 phase. Also given is EDS spectrum collected from the same region.

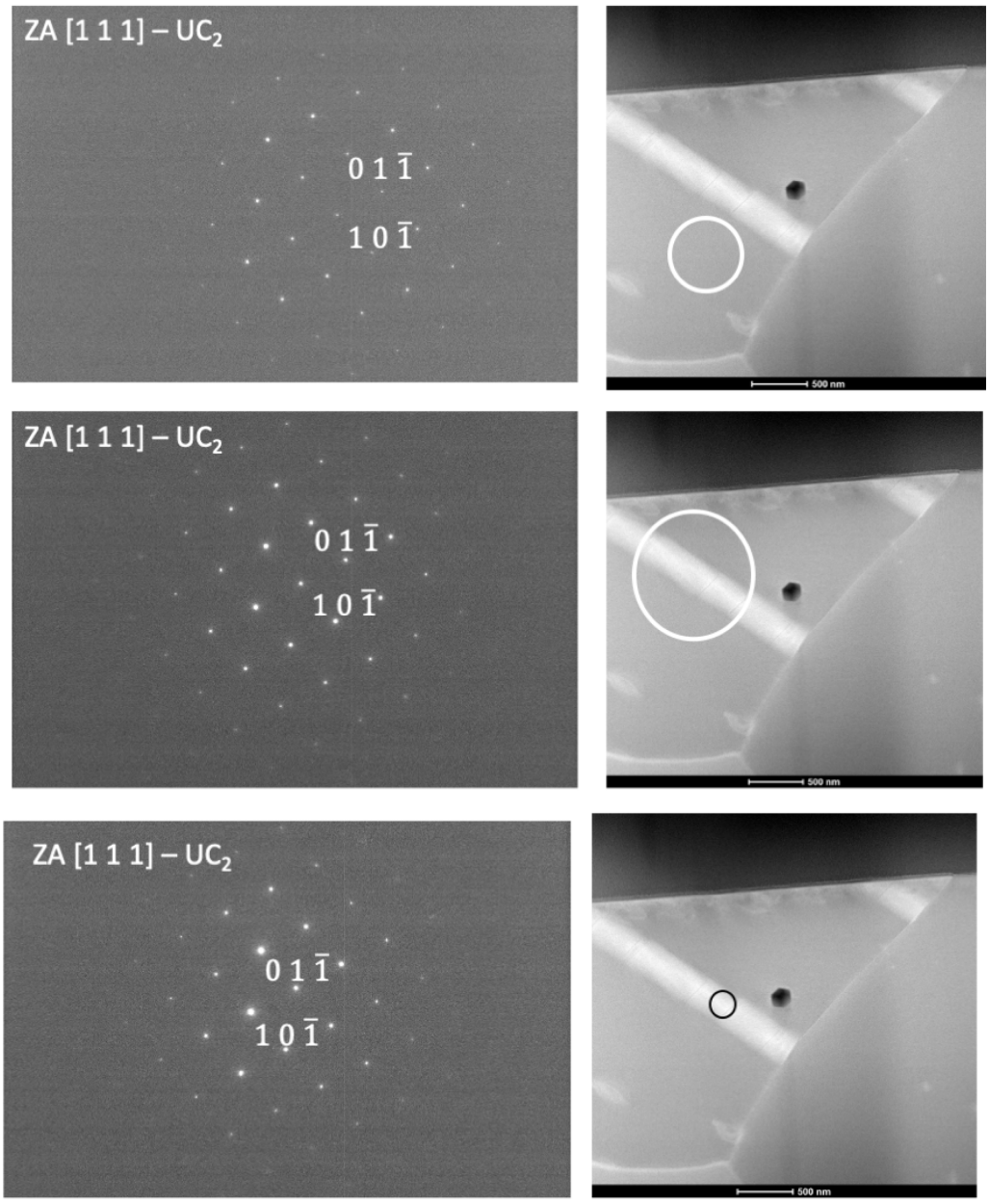

Figure 34. Zone axis diffraction patterns recorded from the circled region of the STEM image in similar sample tilting conditions. The diffraction patterns are indexed with BCT UC_2 phase.

TEM of Irradiated AGR-2 Particle AGR2-222-RS019

The microstructure characterization, elemental analysis, and phase identification were conducted using conventional TEM and STEM imaging, EDS, selected area electron diffraction, and EELS. The whole lamella STEM High Angle Annular Dark Field images were acquired using a Talos F200X STEM/TEM located in the Irradiated Materials Characterization Laboratory at INL. The TEM is equipped with four silicon solid-state detectors that have super sensitive and fast energy dispersive x-ray analysis and mapping down to the atomic scale. Gatan's Enfinium ER (977) spectrometer was used for EELS data collection. EELS analysis was conducted to quantify the relative amounts of C and O in phases of interest. The data analysis is ongoing, and results will be reported soon. Selected results of particle AGR2-222-RS019 (burnup 12.55 % FIMA, 1287°C TAVA irradiation temperature, safety-tested at 1600°C) are discussed in the following section.

AGR2-222-RS019: Fuel Center

Figure 35 shows TEM images and TEM diffraction patterns from selected phases in the AGR2-222-RS019 fuel kernel center lamella. Figure 36 shows the EDS maps and a line scan across phases of UO_2(C)-U_2RuC_2-UC(O)-$UMoC_2$. Based on the EDS maps and TEM diffraction patterns, there are four primary phases in fuel kernel center, which is consistent with what was observed in the particle AGR2-222-RS36 kernel. The EDS line scan in Figure 36 shows that the selected Ru-rich phase is U_2RuC_2. It has a tetragonal structure (point group 4/mmm) as confirmed by the diffraction patterns in Figure 35. The U_2RuC_2 phase (soluble with a small fraction of U_2RhC_2) was found to consistently precipitate next to Zr-rich UC phases. The Mo-rich phase proved to be a $UMoC_2$ precipitate with an orthorhombic structure (mmm point group).

It was also found that the UC phase is depleted of Pd and other rare earth elements (e.g., Nd and Pr). The rare earth elements probably formed oxides in the UO phase, similar to that shown in a typical light-water reactor UO_2 fuel. Some sub-micron-size particles (Zr-rich or Mo-rich) were found decorating the grain boundary of the UO phase. Fission gas bubbles were highly concentrated in the $UMoC_2$ phase rather than in the UC phase. However, in our previous study of a non-safety-tested fuel kernel, the fission gas bubbles were found to mainly be in the UC phase.

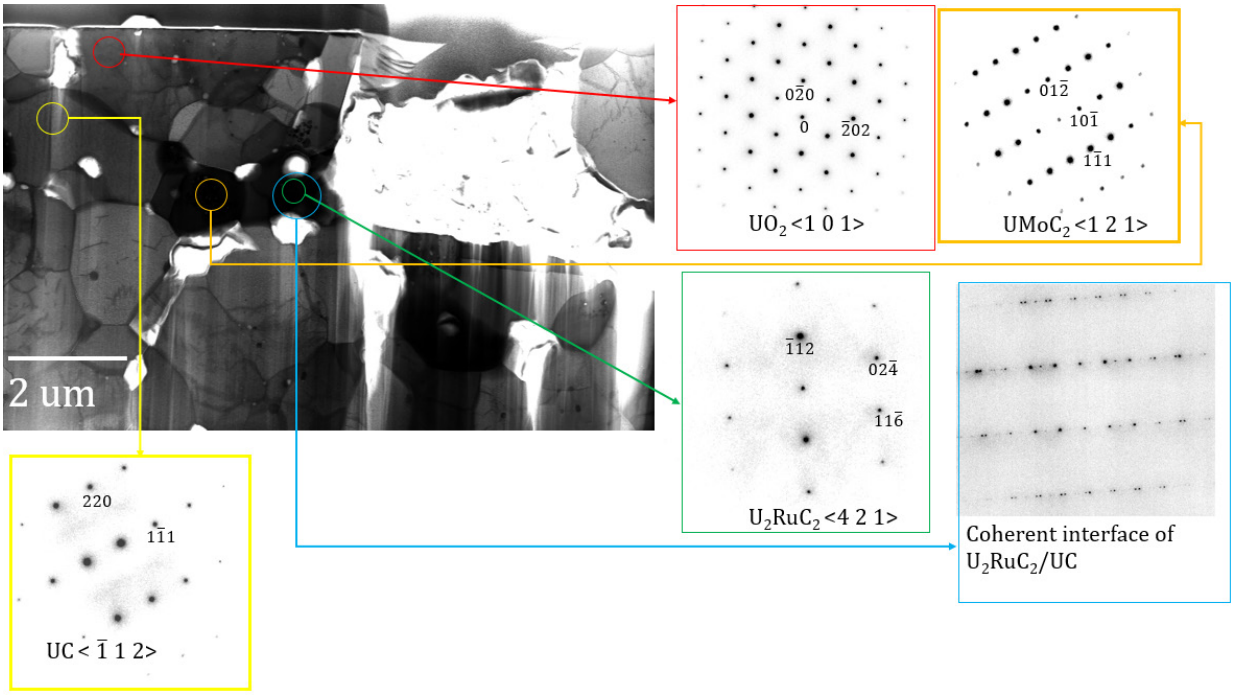

Figure 35. Overview TEM image of AGR2-222-RS019 fuel center lamella and diffraction patterns from selected phases.

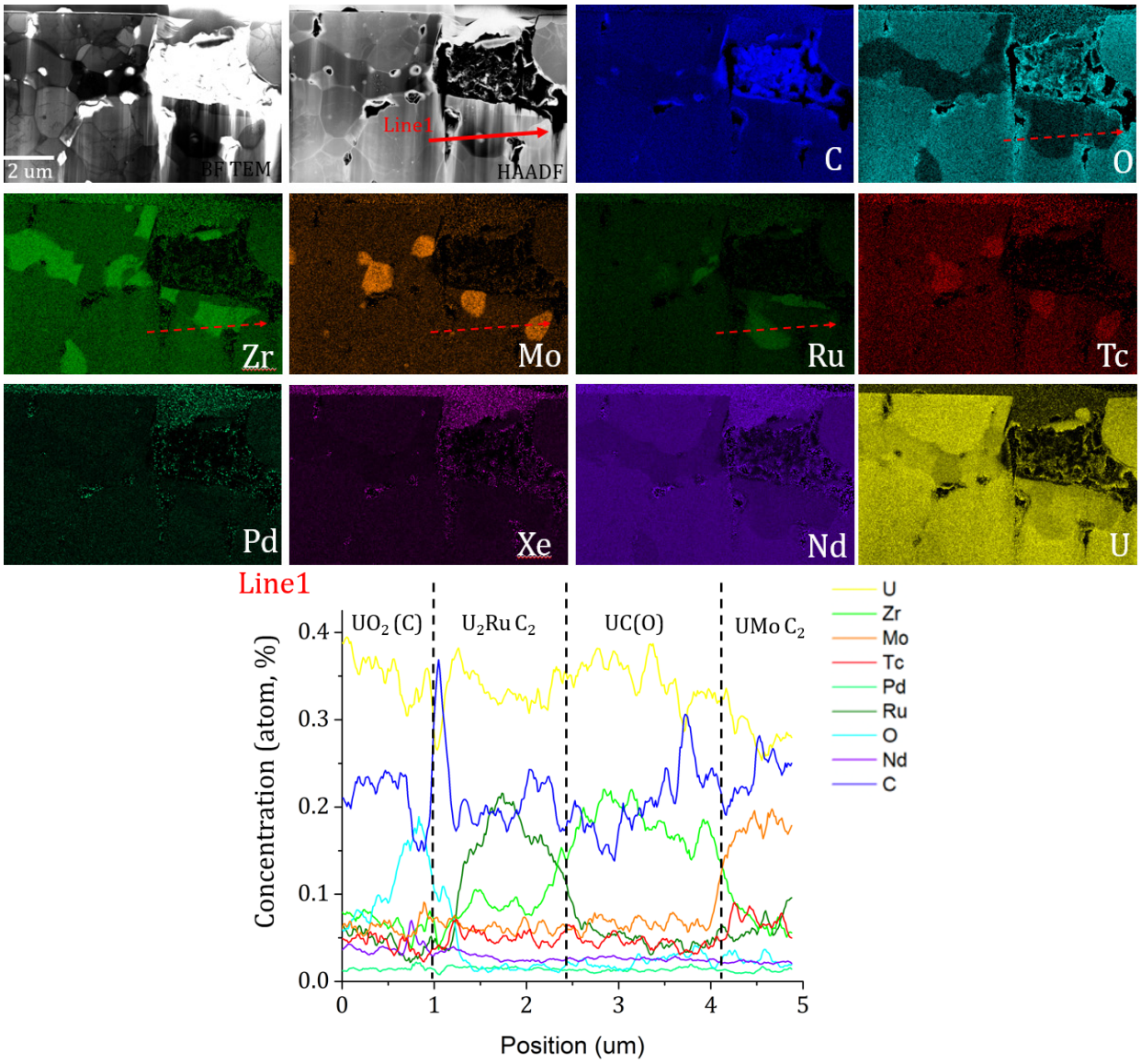

Figure 36. EDS elemental maps (atomic concentration) with line scan from fuel center lamella.

AGR2-222-RS019: Fuel kernel edge zone

Figure 37 and Figure 38 show TEM images, diffraction patterns from selected phases, EDS maps, and EDS line-scans of the fuel kernel edge lamella. A relatively large UC_2 phase is clearly identified, and EDS maps and line scan show that, unlike UC, UC_2 doesn't contain any significant concentrations of Zr. Consistently, rare earth elements are depleted from the UC, U_2RuC_2, and $UMoC_2$ phases. There are no Ag or Pd precipitates observed, based on EDS maps.

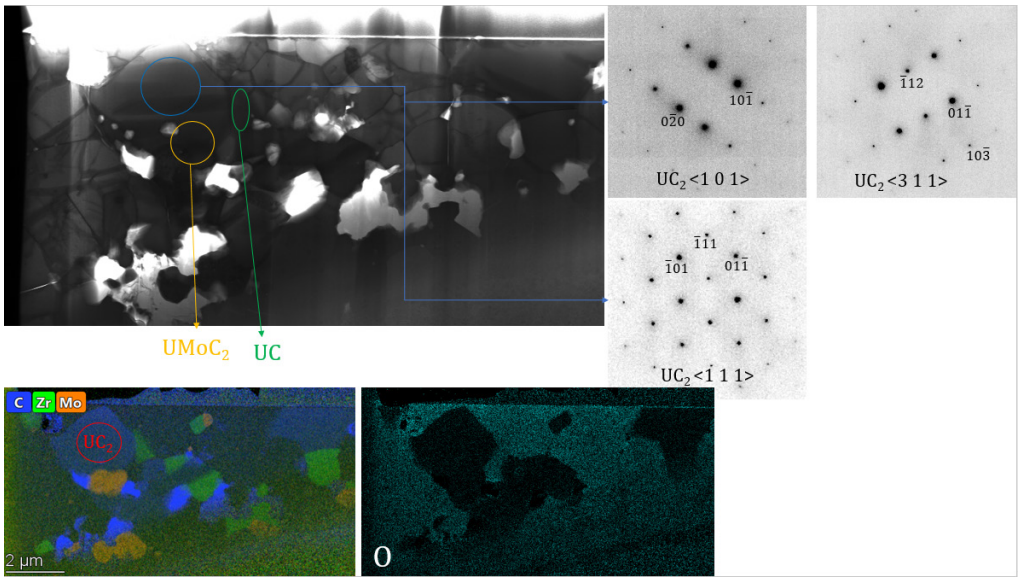

Figure 37. Overview TEM image and EDS maps of fuel recoil zone lamellae along with diffraction patterns from selected phases.

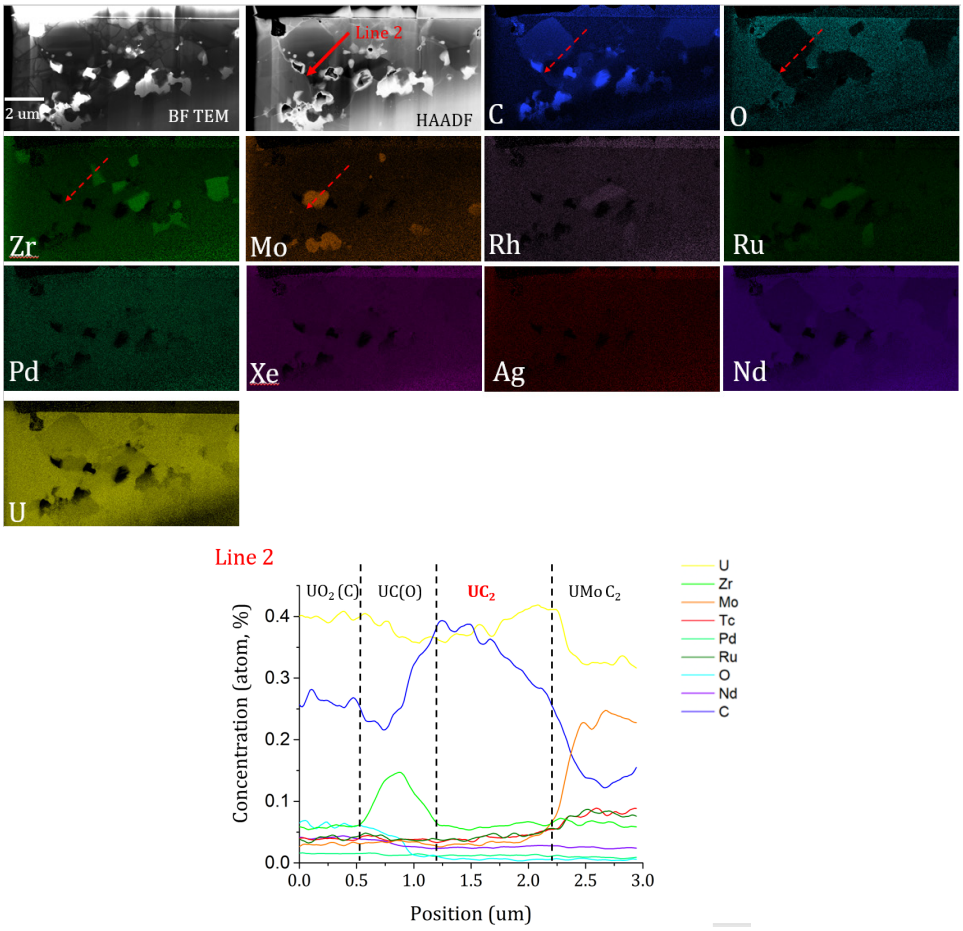

Figure 38. EDS elemental maps (atomic concentration) and line scan.

Fuel kernel-buffer interface.

Figure 39, Figure 40, and Figure 41 show TEM images and EDS maps of the kernel-buffer interface, the buffer layer, and the fuel side of the fuel kernel-buffer interface, respectively. Figure 39 shows that there is a layer enriched with C, O, Xe, Rh, Nd, and Te at the interface. Although it seems to be amorphous from the TEM images, diffraction patterns will be collected to determine its crystal structure. In Figure 40, the TEM images and EDS maps from the fuel kernel side of the buffer show locations of uranium fuel along with Zr, Mo, Ru, Xe, Rh, and Pd readily migrated through the interface, and the buffer layer is also decorated with Mo-rich precipitates tens of nanometers in size. The fuel kernel sides manifest as a porous structure, and the pores are filled with free carbon. There are relatively higher contents of Ag and Pd in this region than in the fuel center or half center. More quantitative results will be included in future reports.

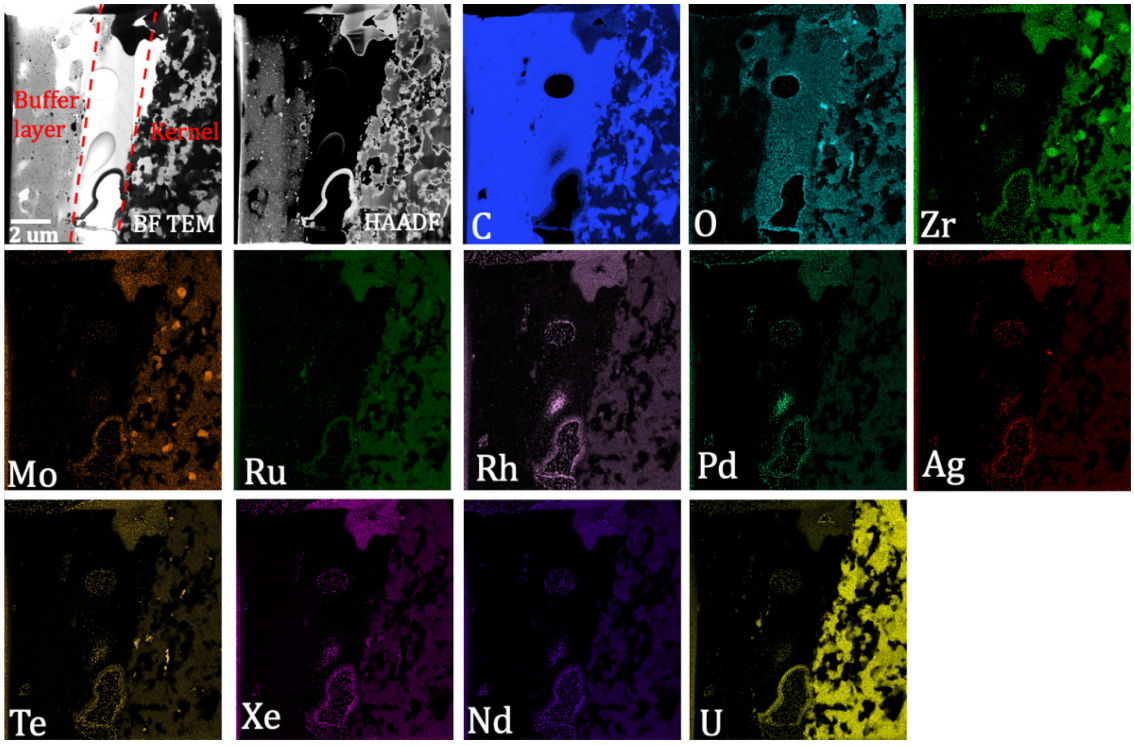

Figure 39. Overview image and EDS maps of the lamella at the fuel kernel-buffer layer interface.

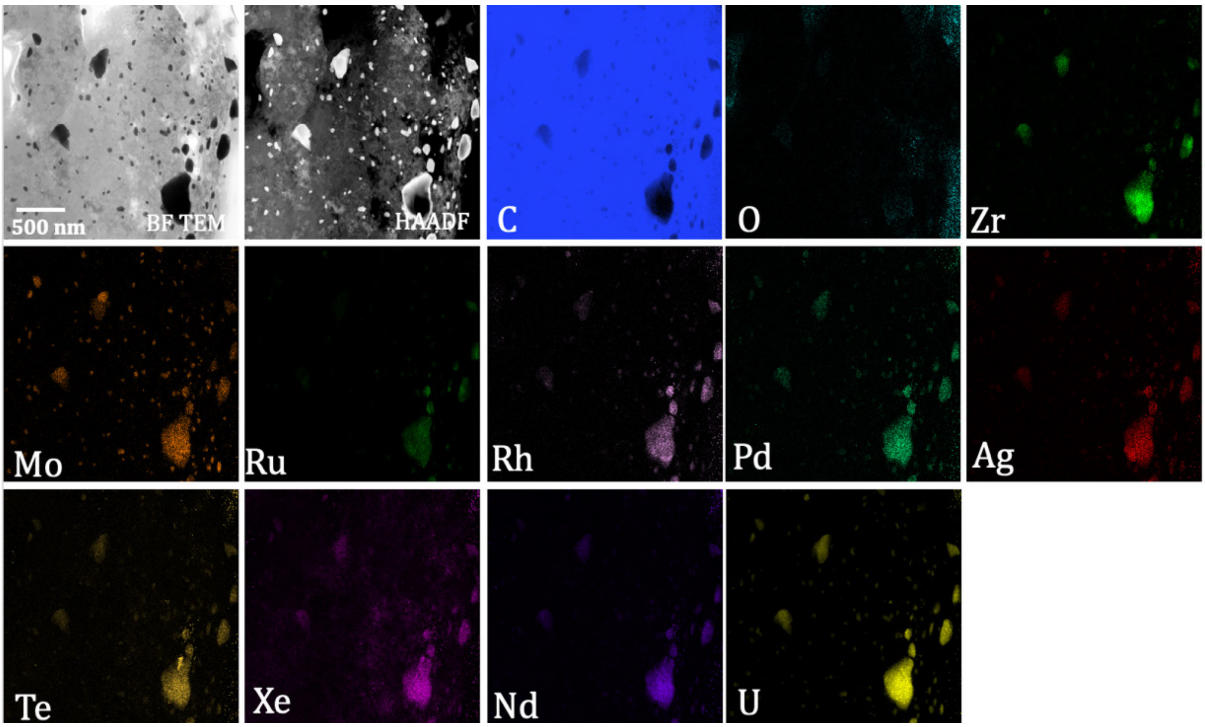

Figure 40. TEM and EDS maps of the buffer layer, showing the migration of U and fission products into the buffer layer.

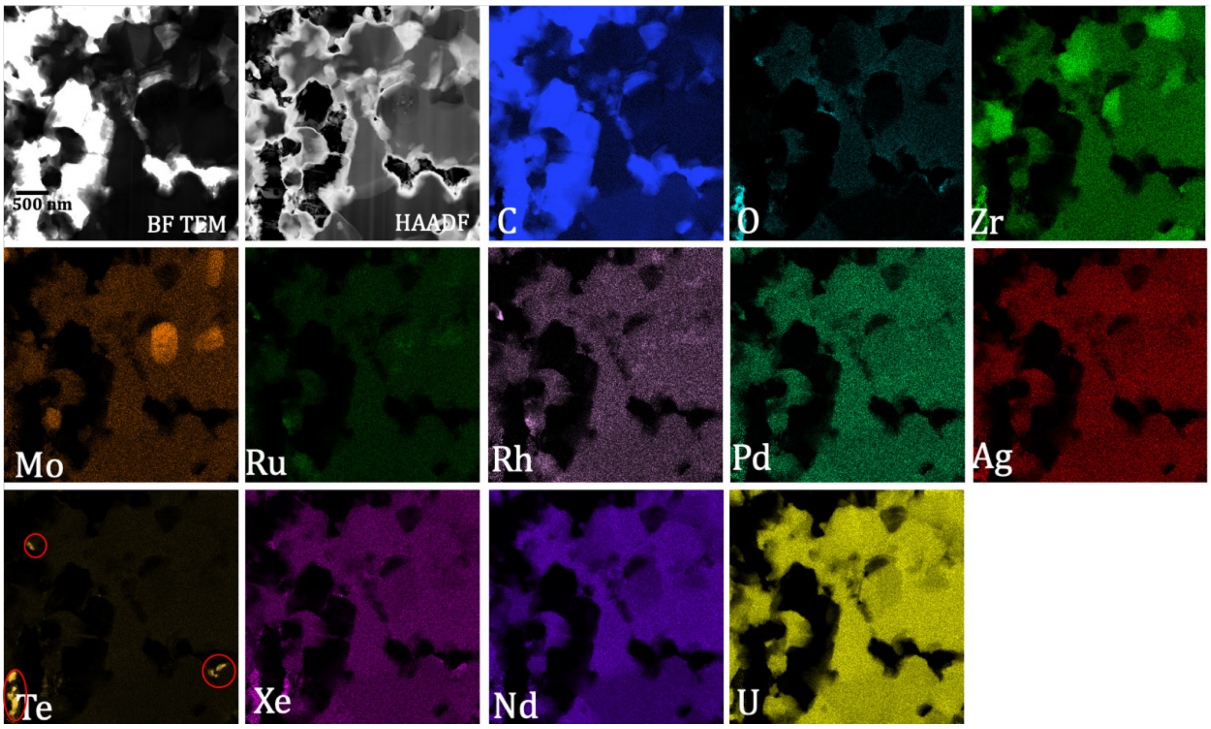

Figure 41. TEM images and EDS maps of the fuel kernel side of the interfacial TEM lamella, showing Te-rich particles.

2.2 High-Temperature Materials

This quarter, an INL staff member presented the High-Temperature Materials Development research at the 2020 ART GCR Campaign Program Review. INL staff members also participated in the August 2020 ASME BPVC Week meeting, which was held virtually. This participation included leadership roles as chair and secretary for both the Working Group (WG) on Allowable Stress Criteria and Task Group on Division 5 Advanced Manufacturing Components as well as attending other committee meetings as members and visitors.

A single smooth bar SMT was performed at INL this quarter. Software controls were used to simulate the bar, which remained in the elastic regime. Alloy 617 was tested at 950°C with a constant elastic follow-up factor of 3. For a few cycles a piece, the virtual strain was 0.4%, 0.7%, and 1.34% during the test. The stress-strain hysteresis loop from the second cycle for each virtual strain is shown in Figure 42 below. Benefits of the SMT include that the creep-fatigue interaction does not need to be separated into individual creep and fatigue components and the need for the overly conservative D-diagram is eliminated. A report on this work titled “Single-bar SMT testing on Alloy 617 using software controls,” was drafted and issued. This report was the deliverable for Milestone M4AT-20IN030502042.

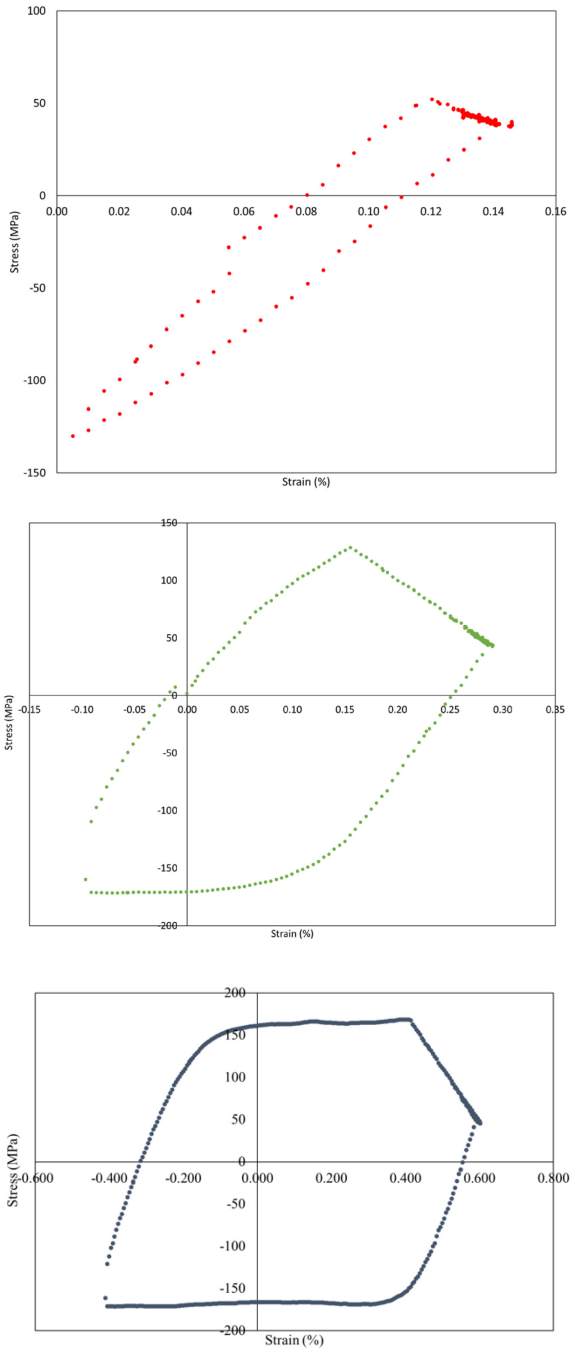

Figure 42. The stress versus strain hysteresis loop from the second cycle for a virtual strain of 0.4% (top), 0.7% (middle), and 1.34% (bottom) for an Alloy 617 SMT performed at 950°C with a constant elastic follow-up factor of 3.

Prior research legitimized the practice of using uniaxial-creep data to constitute short-term design rules. A presentation on these findings was pre-recorded for attendees of the virtual ASME 2020 Pressure Vessels and Piping Conference to watch. Attendees also have access to a conference proceeding on this research. This conference began on August 3 and will end November 1.

This quarter, two Alloy 617 U-notch tests finished. One of these specimens was comprised of weld metal with a small-radius U-notch. The completion of this test wrapped up testing designated as short term. The other specimen was comprised of base metal with large-radius U-notches. This specimen is part of the test program investigating intermediate-length rupture behavior. The Alloy 617 creep-rupture Larson-Miller plot updated with these two tests is shown in Figure 43. The markers for these tests are outlined in red. All completed base- and weld-metal V-notch, large-radius U-notch, and small-radius U-notches tests are also included in the figure as well as uniaxial data for base- and weld-metal specimens fabricated from the same material heats used for notch testing, uniaxial data from base-metal specimens fabricated from various product forms and heats, and a curve fit to 296 uniaxial data points for base-metal specimens fabricated from various product forms and heats (Wright, 2015). The results from the two tests completed this quarter are consistent with previous findings. Specifically, creep-rupture tests with a multiaxial-stress state have a similar or longer creep-rupture life compared to tests with a uniaxial-stress state.

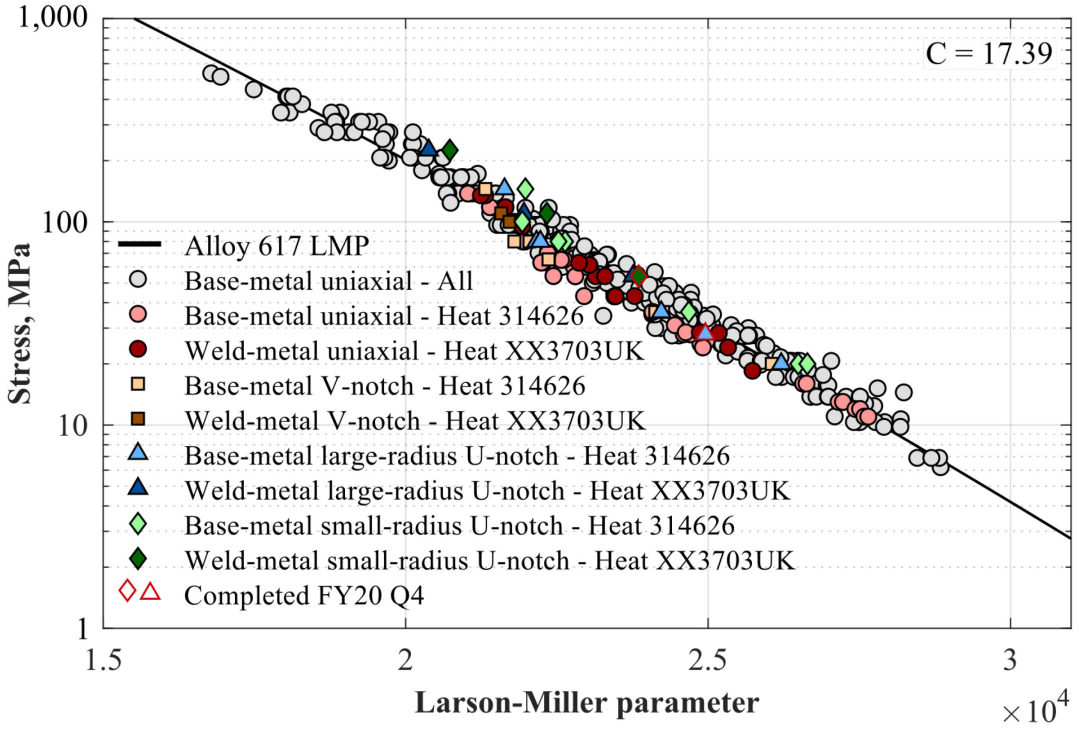

Figure 43. Alloy 617 creep-rupture Larson-Miller plot with all completed V- and U-notch tests fabricated from both base and weld metal. Tests completed this quarter are outlined in red. The uniaxial data for base- and weld-metal specimens fabricated from the same material heats used for notch testing, uniaxial data from base-metal specimens fabricated from various product forms and heats, and a curve fit to 296 uniaxial data points for base-metal specimens fabricated from various product forms and heats are also included.

There are five Alloy 617 intermediate-length U-notch creep-rupture tests and two Alloy 617 long-term V-notch creep-rupture tests in progress. The estimated rupture life for these tests are 12,000 to 16,000 and 100,000 hours, respectively. Intermediate-length and long-term creep-rupture testing is important because notch-rupture behavior is dependent on stress and temperature (Voorhees, 1962) (Delph, 1979). The results from weld-metal testing were summarized in a report titled “Effect of Notches on the Intermediate Creep-Rupture Life of Alloy 617 Weldment,” which was the deliverable for Milestone M3AT-20IN030502041.

It is not viable to wait 100,000 hours, over 10 years, to learn the outcome of a test. Consequently, XCT is being employed to periodically characterize the long-term specimens nondestructively with the goal of identifying the failure location prior to rupture. To accomplish this, shorter baseline testing is necessary to establish the relationship between creep damage and rupture life. This quarter, XCT data was collected from both the notch and straight gauge of an Alloy 617 specimen tested at 800°C and 65.3 MPa that ruptured at the straight gauge. This specimen was previously characterized at 71 and 89 percent life. XCT data was also collected from the notch and straight gauge for an Alloy 617 specimen that is being tested at 800°C and 60 MPa. This data was collected 1,000 hours into the test, which is estimated to have an approximately 8,000-hour rupture life. Cavitation was not observed in the notch nor the straight gauge. Cavitation smaller than the resolution the XCT scan was collected at may be present. The smallest feature that can be identified is 270 μm^3. This test has been restarted and will be interrupted after approximately 1,000 hours of additional testing.

A creep-rupture test at 800°C and 80 MPa was started this quarter for an Alloy 617 base-metal specimen comprised of two V-notches. This test condition was selected because it was also used for uniaxial and V-notch Alloy 617 base-metal testing. These tests had an approximate 1,000-hour rupture life. All completed Alloy 617 V-notch tests have ruptured in the straight gauge with little to no creep damage observed in the V-notch. The double V-notch specimen geometry enables:

- The characterization of the distribution of creep damage at and just prior to specimen rupture by analyzing the ruptured and unruptured notch, respectively
- The quantification of the notch strengthening effect
- The establishment, through baseline testing, of the relationship between creep damage and rupture life in the V-notch
- The comparison of the experimental results to finite-element simulations.

A creep-rupture test of a cross weld with Alloy 800H base metal and Alloy 617 filler finished this quarter. The updated creep-rupture Larson-Miller curve is shown in Figure 44. The test completed this quarter is colored purple. The rest of the Alloy 800H cross welds with Alloy 617 filler are marked by the black squares. The red circles represent the Alloy 800H cross welds with Alloy 82 filler. Filled circles were performed at INL. The blue line is the Alloy 800H parametric curve. The non-INL Alloy 800H cross welds with Alloy 82 filler data and the Alloy 800H parametric constant and stress coefficients are from "A Review of Available Tensile and Creep-Rupture Data Sources and Data Analysis Procedures for Deposited Weld Metal and Weldments of Alloy 800H" (Swindeman 2007). The test completed this quarter fell on the Alloy 800H parametric curve and therefore had the same rupture life as Alloy 800H base metal. Three Alloy 800H cross-weld creep-rupture tests with Alloy 617 filler are ongoing.

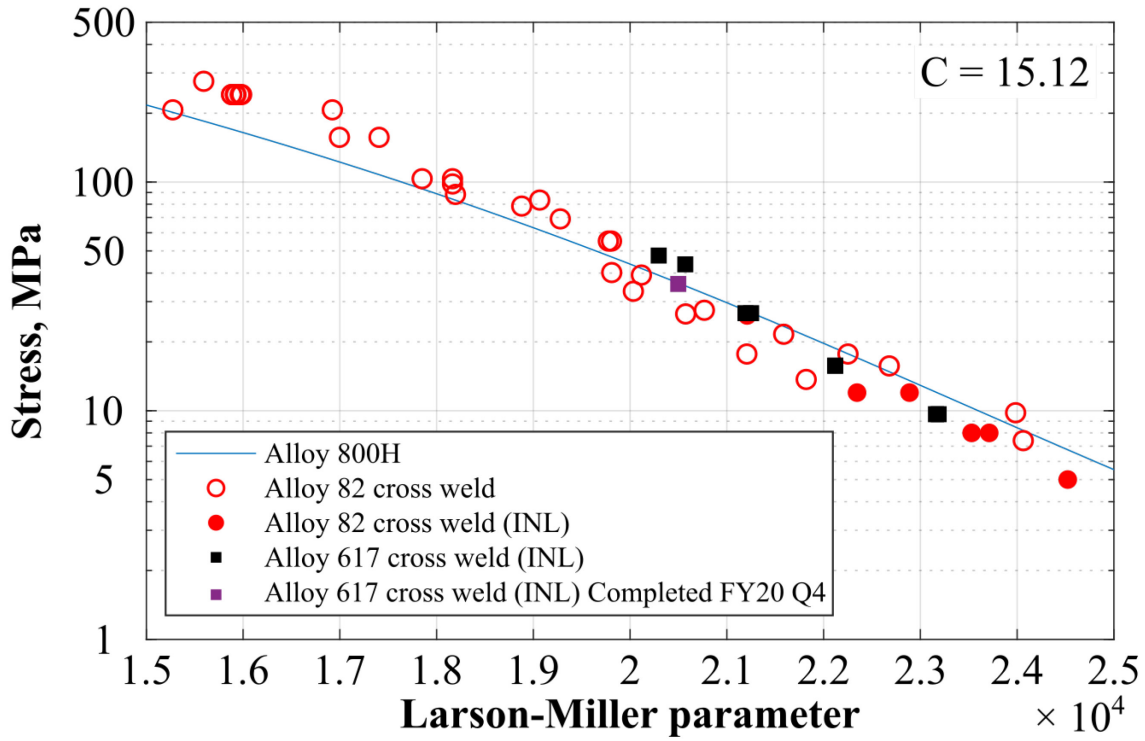

Figure 44. Creep-rupture Larson-Miller plot of the Alloy 800H parametric curve with Alloy 800H cross-weld data with Alloy 82 and Alloy 617 filler. The test completed this quarter is indicated by the purple rectangle.

This quarter we characterized the hardness across the as-received Alloy 800H cross weld with Alloy 617 filler. The results are shown in Figure 45 with the Vickers hardness as a function of the approximate distance from the weld edge. Each rectangle is the average of a minimum of two but typically three measurements. The maximum and minimum error bars are the maximum and minimum values measured, respectively. The gap in the data is a consequence of the welded plate being sectioned for mounting into an epoxy puck. The exact amount of material lost to sectioning is unknown. The dashed lines show the average of six measurements taken from the weld and base metal.

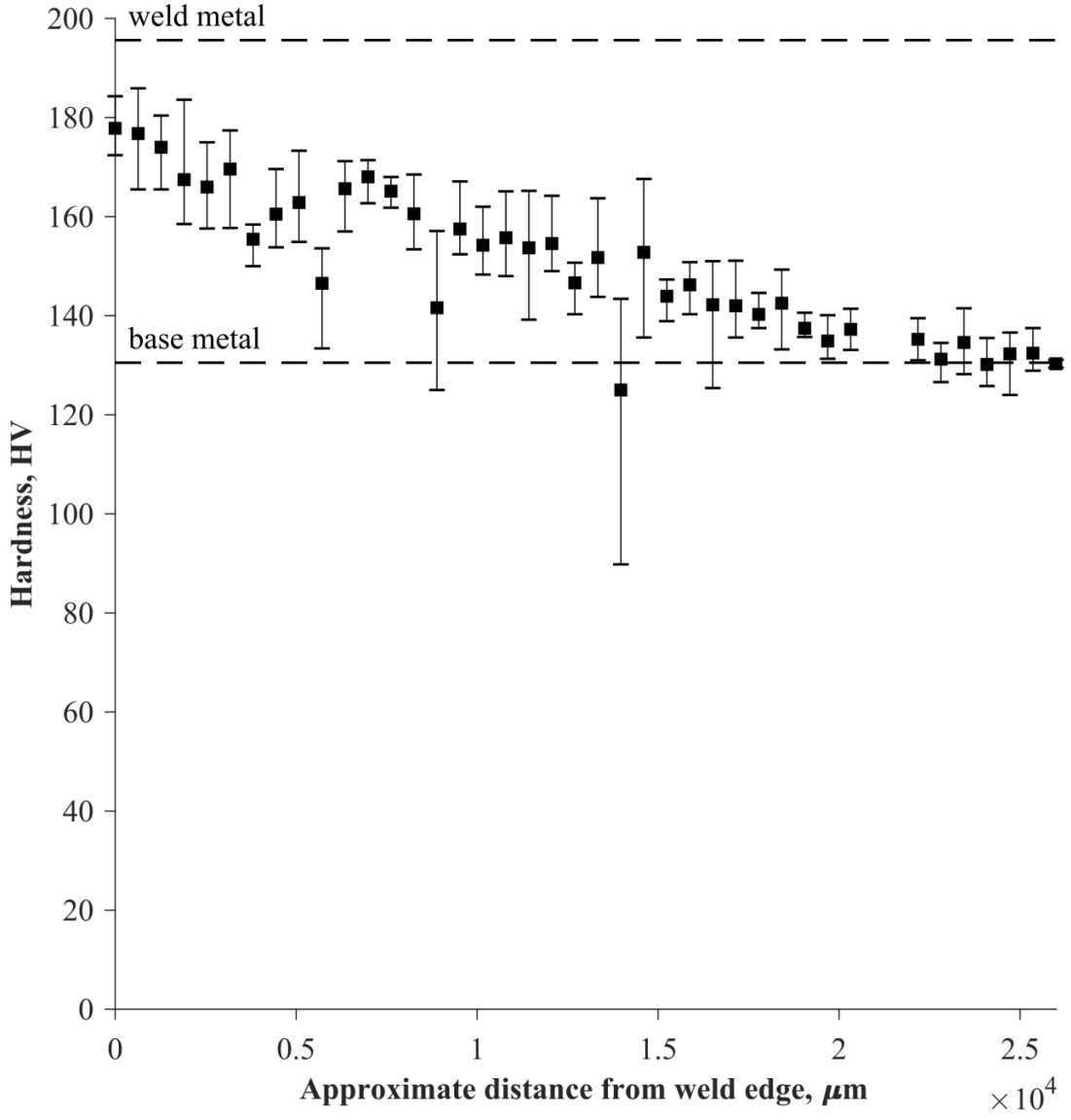

Figure 45. Vickers hardness as a function of the approximate distance from the edge of the weld. The rectangles are the average from a minimum of two but typically three measurements. The error bars are the maximum and minimum hardness measured. The dashed lines show the average hardness of the weld and base metal determined from six measurements. The gap in the data is a consequence of the welded plate being sectioned for mounting into an epoxy puck. The exact amount of material lost to sectioning is unknown.

2.2.1 References

Delph, T. J. (1979). Notch effects in uniaxial tension specimens. Oak Ridge National Laboratory, Oak Ridge, TN, ORNL/TM-6717.

Swindeman, R. W., Swindeman, M. J., Roberts, B. W., Thurgood, B. E., & Marriott, D. L. (2007). A review of available tensile and creep rupture data sources and data analysis procedures for deposited weld metal and weldments of Alloy 800H.

Voorhees, H. R., Freeman, J. W., & Herzog, J. A. (1962). Trends and implications of data on notched-bar creep rupture. *Journal of Basic Engineering*, 84(2), 207-213.

Wright J. K., Lillo, T. M. (2015). Progress report on Alloy 617 time-dependent allowable stresses. Idaho National Laboratory, Idaho Falls, ID, INL/EXT-15-35640.

2.3 Graphite Development and Qualification

2.3.1 Irradiation Experiments–Graphite

2.3.1.1 AGC-4 Status

AGC-4 was received at the HFEF in August as scheduled, and the Dry Transfer Cubicle Cask Insert is in the DOA and remains ready to be unloaded into the HFEF Main Cell whenever the necessary cell lifting equipment can be repaired to receive it.

Operating procedures for the disassembly of AGC-4 in HFEF have been revised and are being put into the document system.

Replacement parts and equipment for the AGC-4 disassembly table have been fabricated and staged for installation in the cell for when the crane and electromechanical manipulators have been repaired. The disassembly equipment is illustrated inFigure 46.

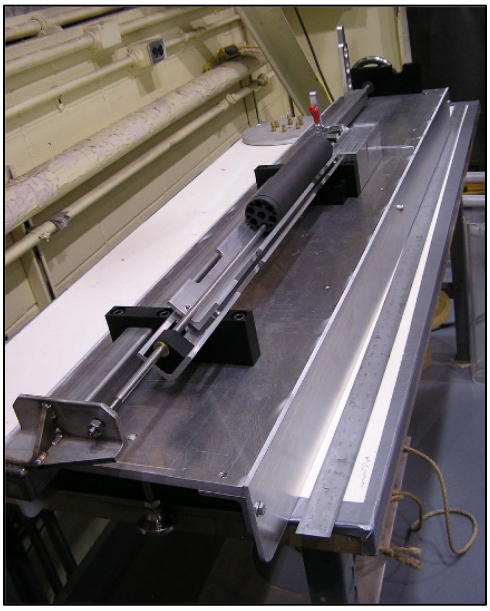

Figure 46. Replacement parts and equipment for the AGC-4 disassembly table.

2.3.1.2 Carbon Lab Preparations for AGC-4

The Carbon Lab recently added two new Netzsch dilatometers to the irradiated testing portion of the lab in preparation for receipt of AGC-4. Additionally, arrangements are being made to replace gloves in the required gloveboxes and to exercise all required equipment and data acquisition systems.

2.3.1.3 HDG-1 Experiment

The HDG-1 Graphite Pre-Irradiation Data Package Report, INL/EXT-20-59175 was completed to satisfy the Advanced Reactor Technologies Level 2 Milestone (M2AT-20IN030504038). This HDG-1 pre-IE Data Package Report, detailing preirradiation mechanical properties, was issued in July.

This report established the preirradiation physical, thermal, and mechanical material properties of each graphite specimen within this first HDG capsule. Approximately 40% of the specimens in the HDG-1 capsule will be reirradiated (60% of the specimens are new).

Estimates of the dose profiles for HDG-1 were calculated to optimize the dose profiles for each graphite grade. Figure 47 shows examples of these dose profile plots for grade 2114, loaded and unloaded.

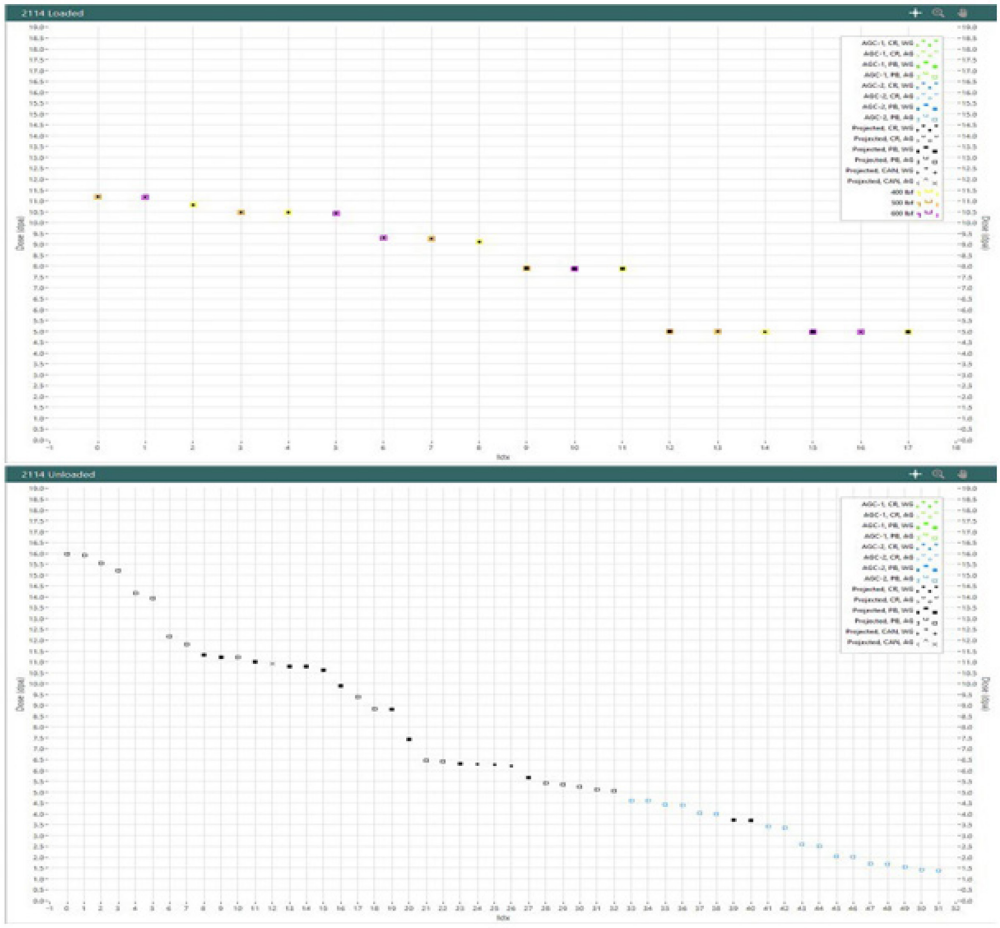

Figure 47. Loaded (top) and unloaded (bottom) HDG-1 dose profile plots for graphite grade 2114.

HDG-1 is the final planned 600°C graphite irradiation test train for the AGC program. As indicated in Figure 48, irradiated test measurements from HDG-1 will be combined with results from AGC-1 and AGC-2 results, also irradiated at 600°C, to establish the irradiated graphite response over a combined neutron dose range from 0.5 to 15 dpa (displacements per atom). Figure 49 illustrates the temperatures achieved within the HDG-1 (the final 600°C irradiation capsule) during the initial 168B irradiation cycle.

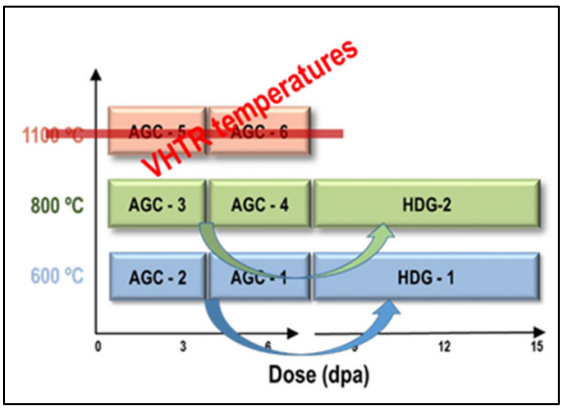

Figure 48. AGC test train progression.

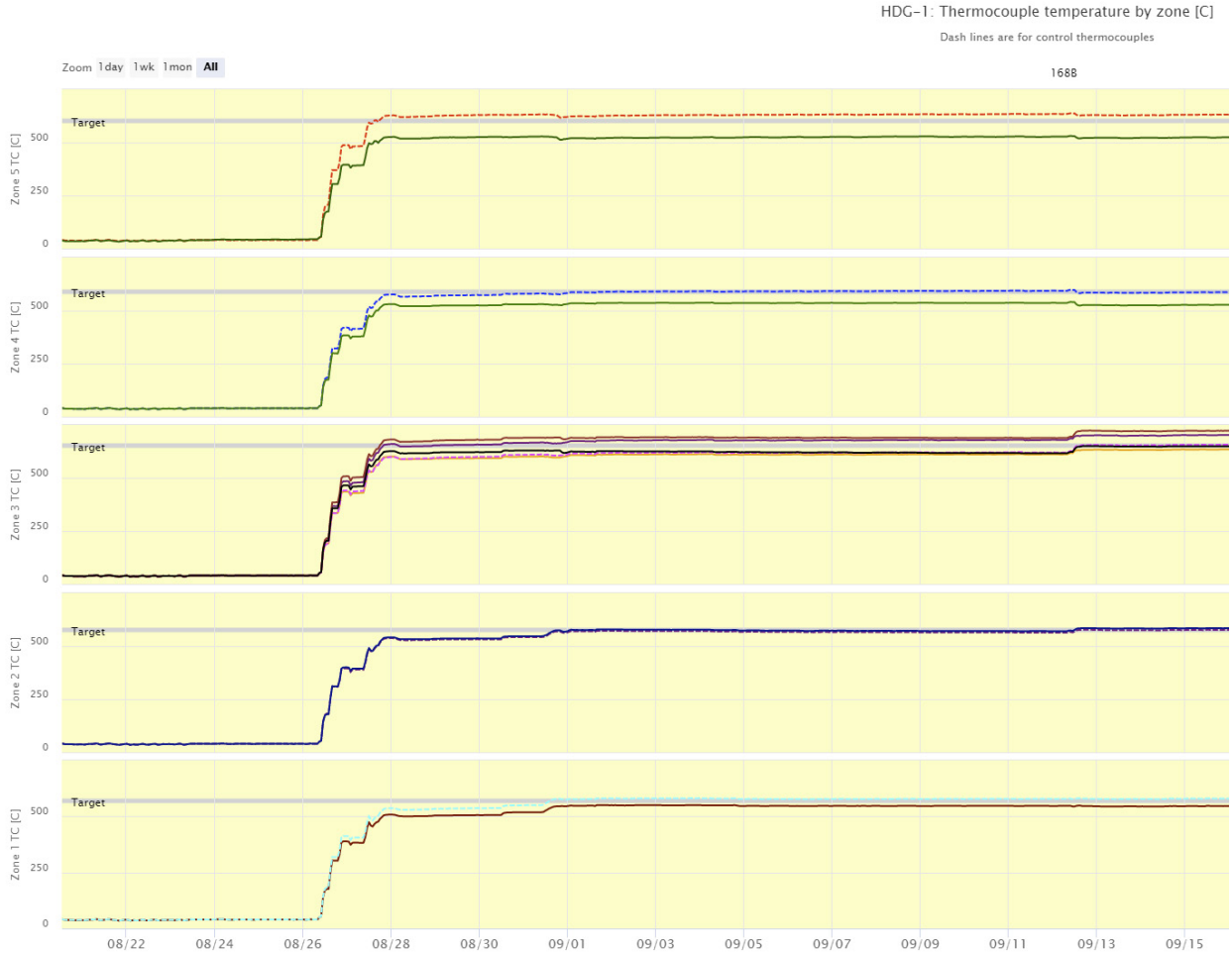

Figure 49. HDG-1 temperatures for cycle 168B.

2.3.2 Materials: Graphite

2.3.2.1 Baseline Characterization

NDMAS

Nuclear Data Management and Analysis System (NDMAS) supports the graphite database encompassing baseline characterization, AGC, and, eventually, HDG specimen data. Along with the data, the reports that were generated from the above data will be available. These reports are currently being sorted based on what data they represent.

The NDMAS team at INL has developed a web-based portal for user access, using SAS software that is part of a new enterprise application software offering at INL. This SAS Visual Analytics report provides interactive data tables and graphs that allow data exploration and means of downloading data in various file formats. These data will be accessible to users outside the laboratory, with permissions as defined by the program directors.

The SAS report currently contains five pages that describe the overall program and provide tables and plots of related properties. Additional pages will ultimately be included to provide the reports from which the data were obtained and to provide a visual representation of in-billet locations of selected samples. The INL Baseline Graphite Characterization Web Portal will be published in early FY 2021.

Screenshots of two example pages of the portal are provided in Figure 50 and Figure 51.

Figure 50. Screenshot of the INL Baseline Graphite Characterization Web Portal home page.

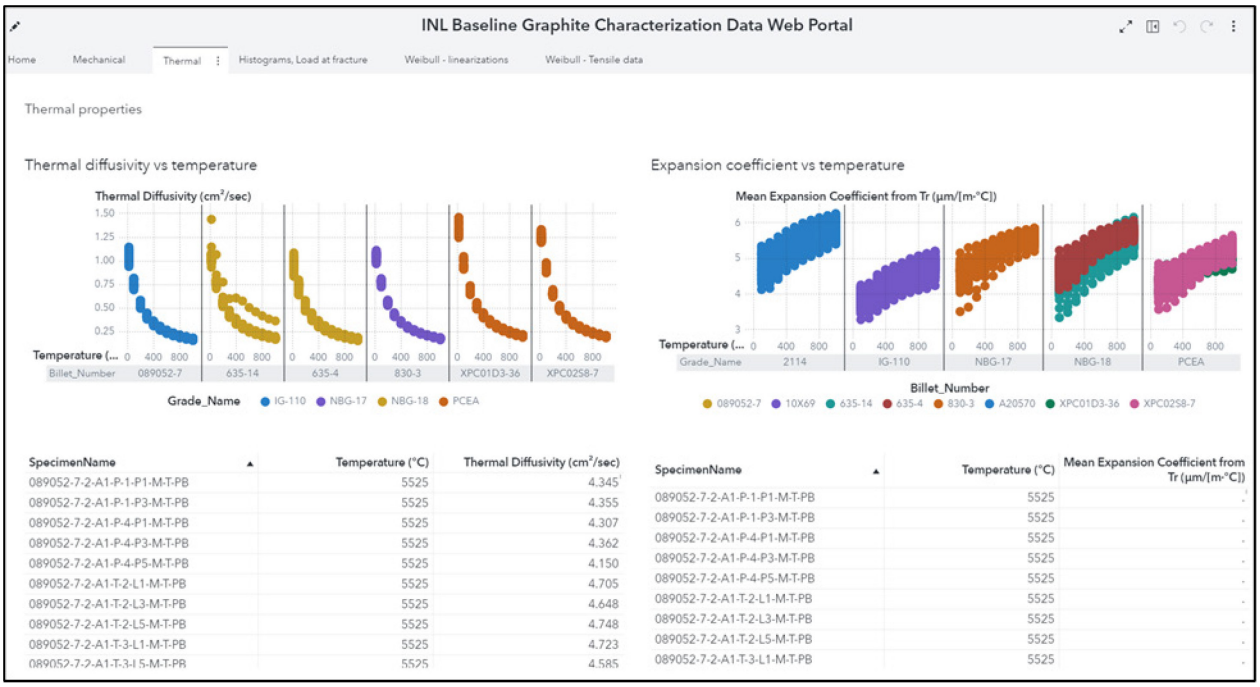

SpecimenName	Temperature (°C)	Thermal Diffusivity (cm²/sec)
089052-7-2-A1-P-1-P1-M-T-PB	5525	4.345
089052-7-2-A1-P-1-P3-M-T-PB	5525	4.355
089052-7-2-A1-P-4-P1-M-T-PB	5525	4.307
089052-7-2-A1-P-4-P3-M-T-PB	5525	4.362
089052-7-2-A1-P-4-P5-M-T-PB	5525	4.150
089052-7-2-A1-T-2-L1-M-T-PB	5525	4.705
089052-7-2-A1-T-2-L3-M-T-PB	5525	4.648
089052-7-2-A1-T-2-L5-M-T-PB	5525	4.748
089052-7-2-A1-T-3-L1-M-T-PB	5525	4.723
089052-7-2-A1-T-3-L5-M-T-PB	5525	4.585

SpecimenName	Temperature (°C)	Mean Expansion Coefficient from Tr (µm/[m·°C])
089052-7-2-A1-P-1-P1-M-T-PB	5525	
089052-7-2-A1-P-1-P3-M-T-PB	5525	
089052-7-2-A1-P-4-P1-M-T-PB	5525	
089052-7-2-A1-P-4-P3-M-T-PB	5525	
089052-7-2-A1-P-4-P5-M-T-PB	5525	
089052-7-2-A1-T-2-L1-M-T-PB	5525	
089052-7-2-A1-T-2-L3-M-T-PB	5525	
089052-7-2-A1-T-2-L5-M-T-PB	5525	
089052-7-2-A1-T-3-L1-M-T-PB	5525	

Figure 51. Screenshot of the INL Baseline Graphite Characterization Web Portal thermal properties page.

Microstructural Studies and Modeling

ORNL continues to apply a wide array of microscopy techniques to characterize a variety of graphite grades included in the AGC program. The micrographs and information obtained will provide a detailed baseline of pristine microstructures that can be compared to those of irradiated samples. The goal is to obtain detailed information of the microstructure of graphite that can be used to understand the intricated connection between grain size, pore size distribution, connectivity, and the mechanical properties of a given graphite grade. Furthermore, these data will be used to inform microstructural based mechanistic models needed to predict the performance of different graphite grades.

Recent XCT data sets were processed to generate pore network models of the connected porosity of the graphite samples; a preliminary model for NBG-18 graphite is shown in Figure 52. The purpose of this analysis was to identify the pore size and their size distribution and connectivity for the various graphite grades. The data will then be compared with mercury porosimetry results. These results will help to evaluate which grades have a higher degree of pore connectivity and calculate other important parameters, such as gas diffusion and permeability.

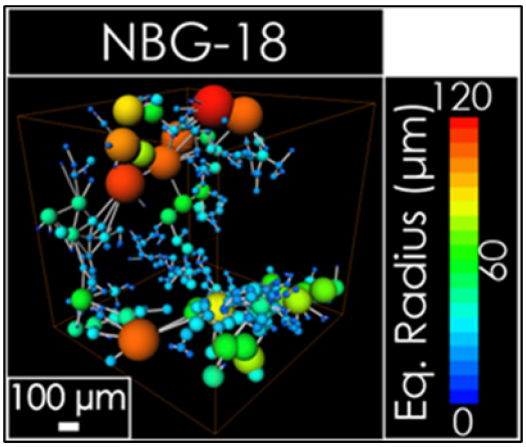

Figure 52. Pore network model of NBG-18 porosity.

Digital Image Correlation System

The Carbon Lab has ordered a digital image correlation (DIC) camera system to accompany the load frame in the irradiated portion of the lab. DIC allows for noncontact strain measurements, which will be essential in performing strain measurements on irradiated graphite samples. It works by applying a speckle pattern or a series of small dots to a specimen and tracking the movement of the dots on a micron scale.

The primary purpose of the DIC system will be the evaluation and strain mapping of split disc tensile testing. This is a relatively new test for graphite that shows a lot of promise as a way of performing tensile tests on irradiated specimens. Initial scoping tests with a similar DIC system are shown below. Figure 53 shows strain readings across the horizontal and vertical axis of the sample. The samples fail in tension in the center, as can be seen from the green plot; there is a tensile strain across the width of the sample.

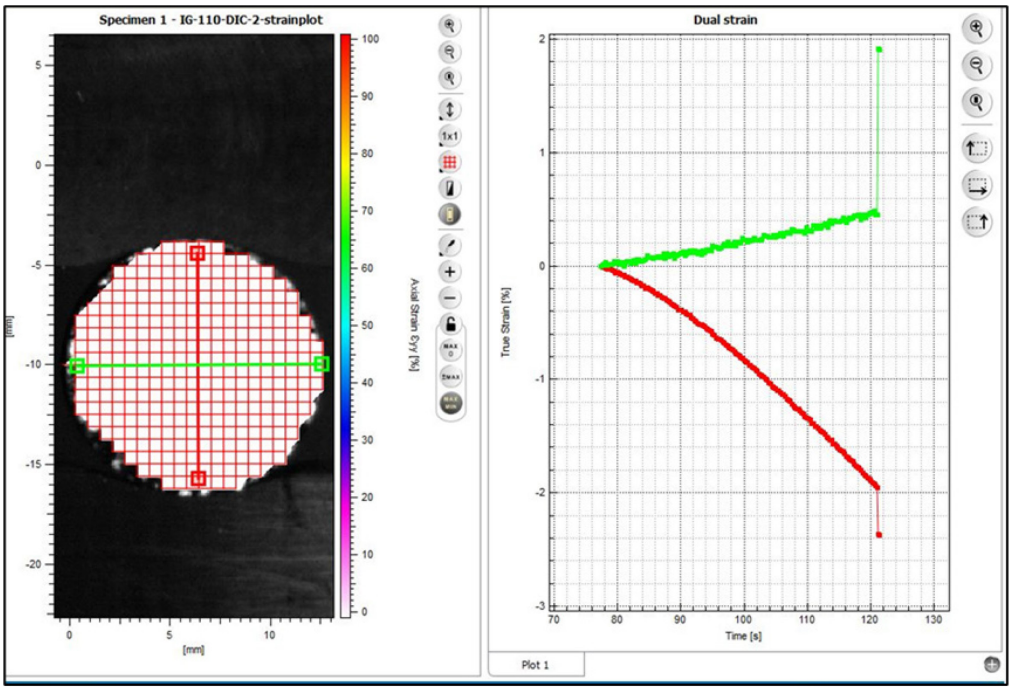

Figure 53. Strain mapped across the horizontal and vertical axes of a split disc graphite specimen.

Figure 54 shows a snip from the video of the sample being broken with a strain map overlay. The blue colors represent compressive strain, and the red colors indicate tensile strain.

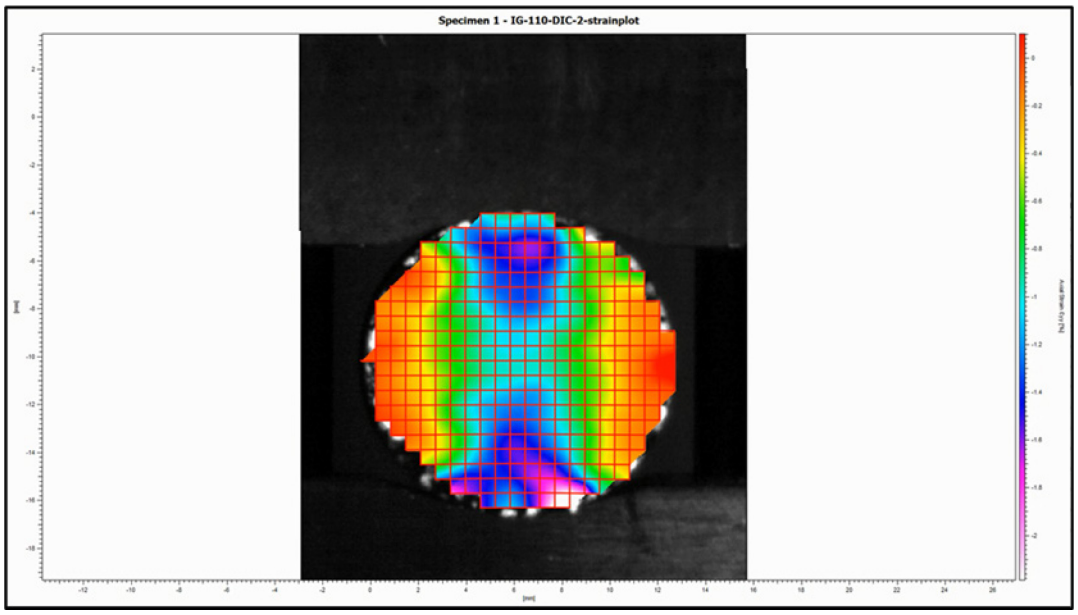

Figure 54. Video image capture of split disc specimen with an overlaid strain map.

2.3.2.2 Graphite Modeling

Graphite modeling work this quarter focused on two main topics. The first is the refinement of the phase-field model used to investigate fractures in graphite, and the second is the parameterization and application of an oxidation model developed by Kane[a].

The phase-field fracture model uses experimentally determined distributions of microstructural features to generate a representative volume element (RVE). Typical RVEs corresponding to the as manufactured and oxidized IG-110 microstructures are shown in Figure 55. This quarter, the procedure for generating the oxidized RVEs was adjusted so that the pores retained a more lenticular shape. This more closely matches experimental observations.

[a] Kane, J. J., et al., "Understanding the reaction of nuclear graphite with molecular oxygen: Kinetics, transport, and structural evolution", *Journal of Nuclear Materials,* Vol. 493, 2017, pp. 343-367.

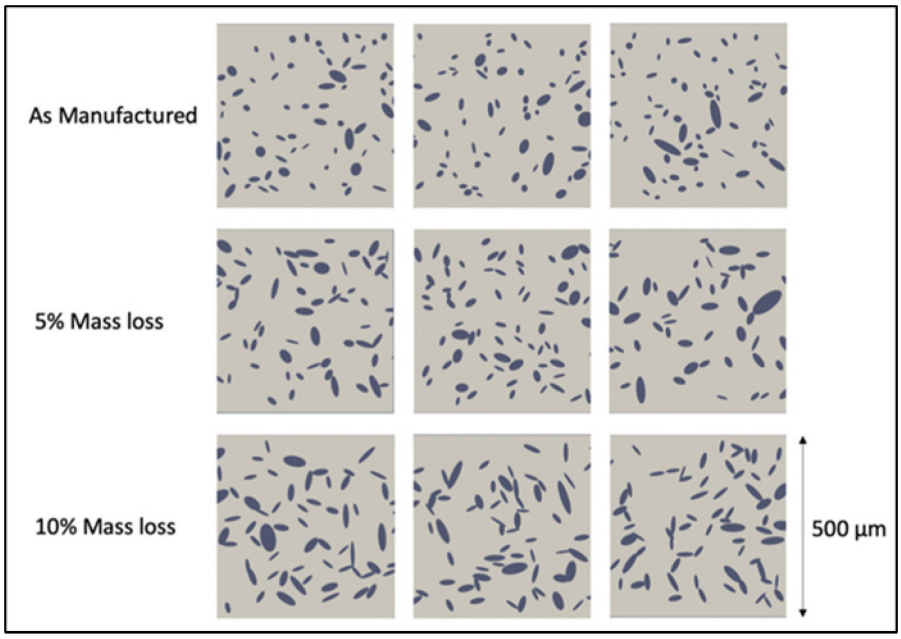

Figure 55. Representative volume elements for the as manufactured and oxidized microstructure of IG-110.

The tensile strength is simulated by imposing a constant strain rate, which results in the evolution of the damage phase (crack). This procedure and ultimate damage phase are shown on the left and right side of Figure 56, respectively.

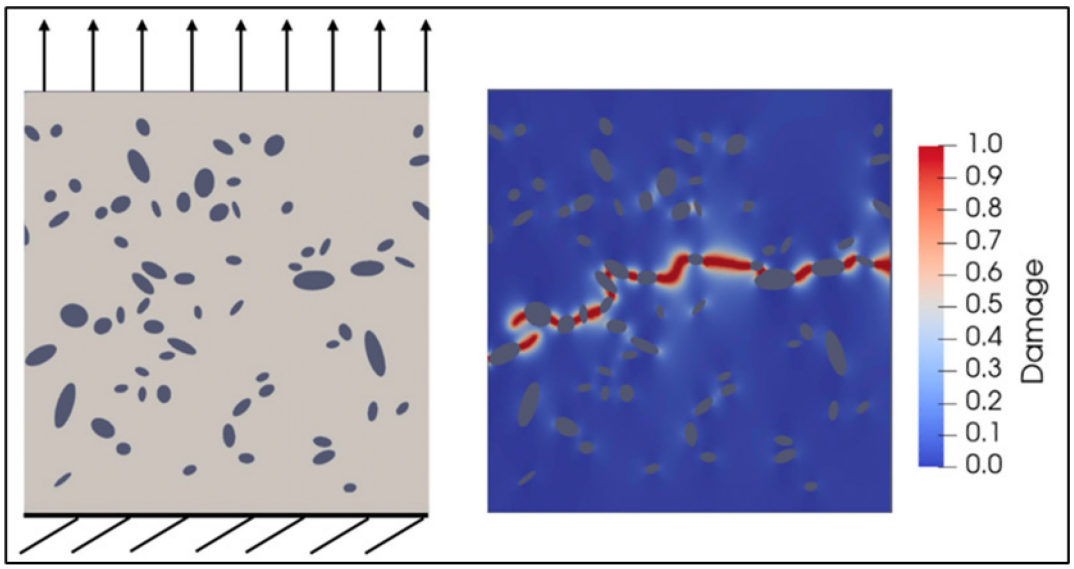

Figure 56. Schematic of the tensile simulation (left) and resulting damage phase (right).

Multiple simulations are run, each with a unique RVE, which produced the strength distribution data shown in Table 10. Comparing the experimental and simulated results in the top two rows of the table, the model can be seen to match the experiment reasonably well.

Table 10. Simulated maximum tensile strength distribution in IG-110.

	Mean	SD	Scale (Weibull)	Shape (Weibull)
As Manufactured Experiment	25.69	1.88	25.51	16.19
As Manufactured Simulated	22.25	2.34	22.26	11.51
5% Mass Loss Simulated	15.45	1.78	16.21	10.49
10% Mass Loss Simulated	9.96	1.64	10.63	7.14

Turning to Table 11, the simulated strength loss after oxidation compares well with the strength loss determined from upsetting experiments performed at INL.

Table 11. Strength loss percent after oxidation.

	5 Percent Mass Loss	10 Percent Mass Loss
Simulation	30.5 %	55.2 %
Experiment	33 %	53 %

As seen in the above phase-field fracture work, oxidation can cause a significant degradation to a graphite's mechanical behavior. Therefore, it is important to be able to determine to what extent oxidation might occur under various conditions. This quarter, the graphite oxidation model developed by Kane was reparametrized for graphite grade NBG-18. Simulations were run for various sample geometries. Figure 57 shows the simulated mass loss as well as experimental results from INL for multiple specimen geometries, illustrating that the oxidation model reproduces the experimental mass loss trend quite well.

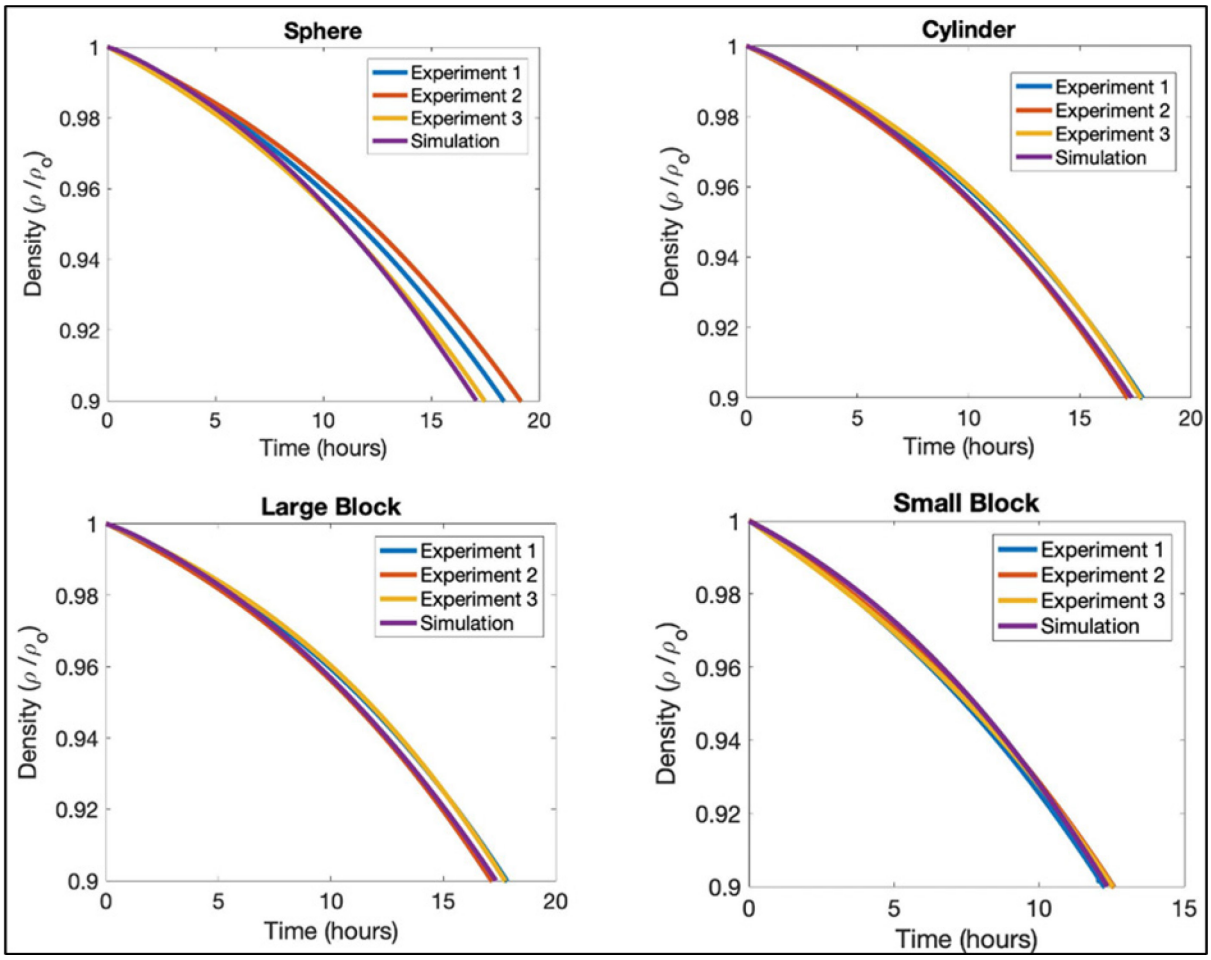

Figure 57. Simulated and experimental oxidation mass loss on nuclear grade graphite NBG-18 for various specimen geometries.

2.3.3 Collaborations and Licensing: Graphite

2.3.3.1 GIF Graphite Working Group and Project Management Board

The fall Project Management Board (PMB) meeting was held virtually in September. An update was provided on the latest graphite research from participating Generation IV Information Forum (GIF) countries. USA highlights included the completion of AGC-4 irradiation (DOE) and start of HDG-1 irradiation (DOE).

The GIF Project Arrangement on Materials for international research and development on development of very-high-temperature reactor nuclear energy systems is centered on graphite used for fuel elements, core supports, and reflectors. One task assigned to the GWG included data collection on the graphite oxidation kinetics and oxidation effects on mechanical and physical properties upon oxidation in air. Chronic oxidation by impurities in the helium coolant is addressed by accelerated oxidation tests in conditions nonperturbed by diffusion and at low concentration of oxidant in helium. Separate experiments should be performed for the evaluation of effective diffusivity of gas impurities. The final goal is the development and validation of models that might be included in computer codes. The report on graphite oxidation was initiated in September 2020 and will outline the activities from the last 10 years (2010–2020) funded by DOE through the NGNP and ART programs. The time frame for drafting, reviewing, and approving the report for distribution is estimated at 5–6 months (February–March

2021). The report on U.S. contributions will be used as an input for the high-level deliverable document for the graphite oxidation work package to be submitted to the PMB.

The ART graphite technical lead, Dr. William Windes, agreed to initiate a discussion between the existing GWG countries and the newly joined GWG countries to ascertain the level of interest in technologies addressing spent graphite waste. If there is enough interest and common objectives between participating GIF countries, a new task within the decommissioning and disposal technology area will be added.

2.3.3.2 ASME and Licensing

ASME Irradiation Data

Currently, the ASME code does not specifically address how to include irradiation or oxidation degradation behavior in nuclear graphite applications. A major effort is being undertaken to determine the best method for using irradiated and oxidation data. ART graphite experts are leading this effort and will use results from the AGC Experiment, acute and chronic oxidation studies, and effects of oxidation studies. Only publicly available data can be used, such as results from the AGC (USA) or INNOgraph (EU) experiments which limits the total amount of data available (i.e., data from commercial, research, and international laboratory studies not in the public domain must be excluded from consideration) .

The current strategy is to initially limit graphite irradiation response up to the turnaround dose value for each specific graphite grade. As shown in Figure 58, the irradiation response for all tested grades (in both AGC and INNOgraph experiments) demonstrates a predictable linear response up to and slightly past turnaround. This region is also within the linear creep response for all graphite grades, demonstrating an additional common response within this irradiation dose range. The intent is to use this common behavior for all grades to develop the code for all potential graphite grades that can be used for nuclear core internals.

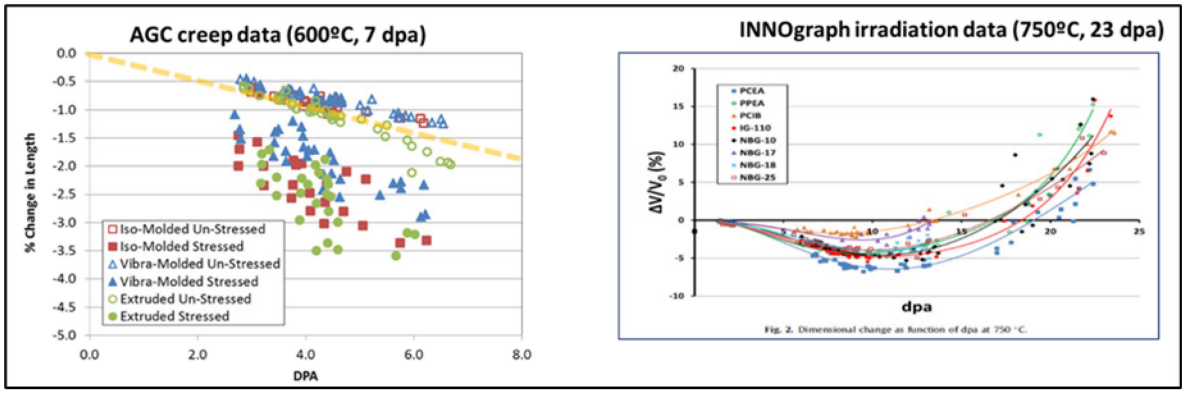

Figure 58. Irradiation response for all grades of graphite tested during AGC and INNOgraph experiments.

NRC Support

The NRC has asked various ART graphite researchers for technical assistance in areas including ASME code interpretation, behavior modeling, and ASTM testing standard development. Specific activities will be funded by the NRC through separate subcontracts, but the hope is that we can leverage ART graphite activities within these specific NRC research areas to provide greater insight into the licensing requirements for commercial HTR designs.

NRC/Numark Inc. Responses

In June 2020, the NRC requested that the ASME Nonmetallic Design and Materials Working Group (NWG) AGC and INNOgraph experiments respond to comments generated by Numark Inc. during their technical review of the graphite section of the ASME BPVC. This review of the ASME code by Numark

Inc. was performed in support of the NRC's effort to endorse the graphite section the BPVC. The review encompassed the entire HHA Graphite Materials subsection of the code and produced over 50 comments requiring detailed responses.

ART graphite researchers took the lead in responding to this review and have provided an initial copy of the responses to the NRC in August 2020. The final draft of the responses was provided to the NRC in October 2020.

NRC Gap Analysis

The ASME and NRC has requested that the ASME NWG assess the graphite code as written within the 2017 version of the BPVC. Two documents are to be produced during this assessment; a background document describing how the code was developed with appropriate public references and a gap analysis describing those areas of the code that could be improved, or optimized, for eventual use by a commercial license applicant.

- *Background document:* The draft manuscript, which documents the background on the code rules for designing graphite core components, was submitted July 30th to ASME for publication consideration as a Nuclear Technical Book. It is currently under review and assessment by ASME, who will produce the proofs for publication review.
- *Gap analysis:* The gap analysis has been delayed to coordinate the content with the NWG responses to the NRC/Numark review comments. While the NWG responses are intended to completely answer the Numark comments, the underlying concepts for both the comment and response require additional information. The gap analysis report is intended to fulfill this purpose by providing additional information on some of the more complex issues addressed within the NRC review. The gap analysis will be finalized after the NRC/Numark responses have been completed and delivered to the NRC.

ASME Code Development

Virtual meetings of ASME BPVC Week (ASME BPVC 2020) and the ASME WG: Nonmetallic Design and Materials (SG-HTR, BPV III) were attended on Tuesday, August 18, 2020. A design code reference was proposed to address the compilation of the United Kingdom (UK) experience with damage tolerance in graphite cores. A discussion with the UK regulator was initiated regarding document access.

ASME adopted a new method that uses a process zone volume to determine the mesh size in the finite-element model when calculating the probability of the failure of a component. Previously, the mesh size was defined using the grain size as a reference to calculate a process volume. An independent validation calculation was performed to compare the two methodologies and demonstrated that the process zone method was an improvement when stress analysis results were compared. The change was proposed through two ASME records, 16-2113 and 16-2114, which was approved by all subcommittees as well as BPV III. The change will be adopted in the 2021 edition.

The design and construction rules for composite components and assemblies appeared the first time in the current edition of the ASME BPVC Sec III, Div 5, under subsection HH, subpart B, and the general requirements of subsection HA, subpart B. This was a significant accomplishment after an undertaking of several years (at moderate effort), which was first proposed in 2008. The ASME code for composite materials applied the simplified assessment, previously discussed, whereby the material strength is probabilistically determined, which was compared with the component stress limit assigned by the predefined structural reliability class.

ASTM Standards

ASTM Virtual Meetings

Virtual meetings of the ASTM D02.F0 Subcommittee on Manufactured Carbon and Graphite Products were attended June 30 and July 1, 2020. With the retirement of W. David Swank, the attendees needed to address the replacement of secretary to the subcommittee. In the absence of other volunteers, Martin Metcalfe agreed to act as caretaker secretary. A stalled standard guide (2016) has been edited and progressed through to subcommittee ballot.

ASTM STP and Symposium

The technical theme for a proposed ASTM STP publication and symposium was discussed, and the STP title "Graphite Testing for Nuclear Applications: The Validity and Extension of Test Methods for Material Exposed to Operating Reactor Environments" was agreed upon. An announcement document has been drafted. Manufactured Carbon and Graphite Products subcommittee members proposed, and ASTM officers approved the concept, holding this symposium in September 2021 in Chicago as part of the International Nuclear Graphite Specialist Meeting. For the STP and symposium to go ahead, a minimum of 12 papers will be required. National Nuclear Laboratory (UK) is offering to present four papers with possibly one extra. U.S. DOE labs expect to provide 4–5 papers. Indications from China's Shanghai Institute of Applied Physics and the Office for Nuclear Regulation in the UK have been positive. Targeted approaches from AST D02.F0 members have been made to the Nuclear Research and Consultancy Group in the Netherlands, as well as to Universities of Oxford and Manchester (UK). Organizations and contacts in South Korea and Japan are being identified to request further global support for this endeavor.

ASTM Standard E181

Currently, the ASTM E181 Standard Test Methods for Detector Calibration and Analysis of Radionuclides is under consideration for revisions within the ASTM E10 committee, which governs standards related to reactor dosimetry. ASTM E181 is ill-suited for applications within the Advanced AGC program, specifically because it pertains to the interpretation of flux wires embedded in graphite samples irradiated in the ATR. Historical flux wire data obtained in the AGC program has been inconsistent, and quantifiable uncertainties have been difficult to ascertain. The AGC program is funding an effort to revise and improve E181, which will lead to high quality, repeatable data for the neutron flux, and therefore irradiation damage, in the AGC graphite samples. The effort will consist of a round robin measurement of a single set of flux wires (potentially candidates include Co, Fe, Ti, Nb, Ni, and Cu). A round robin measurement effort is under development to assess a single set of flux wires (potentially candidates include Co, Fe, Ti, Nb, Ni, and Cu) at multiple independent institutions, as shown in Table 12.

Table 12. Participants in round robin flux wire measurements.

Role	Name	Work Location	Measurement Laboratory	Contact Email
Project Manager	Will Windes	Idaho National Laboratory	—	will.windes@inl.gov
Project/Sample Coordinator	Tommy Holschuh	Idaho National Laboratory	—	tommy.holschuh@inl.gov
Measurement Station #1	Jorge Navarro	Oak Ridge National Laboratory	Neutron Activation Analysis Laboratory	navarroj@ornl.gov
Measurement Station #2	Tommy Holschuh	Idaho National Laboratory	IRC Reactor Metrology Laboratory	tommy.holschuh@inl.gov

Role	Name	Work Location	Measurement Laboratory	Contact Email
Measurement Station #3	Michael Reichenberger	Idaho National Laboratory	Radiation Measurements Laboratory	michael.reichenberger@inl.gov
Measurement Station #4	Greg Fischer	Westinghouse	Pace Analytical Services	fischega@westinghouse.com
Measurement Station #5	Larry Greenwood	Pacific Northwest National Laboratory	Radiochemical Processing Laboratory	larry.greenwood@pnnl.gov
Measurement Station #6	Dave Vehar	Sandia National Laboratories	Radiation Metrology Laboratory	dave.vehar@sandia.gov

A set of flux wires will be irradiated at the High-Flux Isotope Reactor in FY 2021 with the purpose of activating long-lived radioisotopes to be measured by a group of metrology laboratories in the United States. The various labs will quantify the absolute activity in each irradiated wire at the end of irradiation.

The flux wires will first be measured at the Neutron Activation Analysis Laboratory for logistical ease, then will be transported to INL and measured at the INL Research Center (IRC) Reactor Metrology Laboratory and Radiation Measurement Laboratory. The fourth and fifth measurement stations are designated as Westinghouse and Pacific Northwest National Laboratory. The timeline for these two measurement stations has not been finalized, and the order may be changed depending each laboratory's schedule.

ASTM E481

ASTM E481 Standard Test Method for Measuring Neutron Fluence Rates by Radioactivation of Cobalt and Silver is under consideration within the ASTM E10 committee. The standard uses the thermal neutron activation of irradiated cobalt and silver wires to obtain neutron fluence rates in the thermal neutron region as well as estimate the mean neutron energy in the spectrum (corresponding to the average neutron temperature). Within the reactor dosimetry community, a specific nuclear data library is used to evaluate flux wire reaction rates. The International Reactor Dosimetry and Fusion File (IRDFF) consists exclusively of experimental nuclear data as compared to other evaluated nuclear data file (ENDF) libraries, such as ENDF/B (USA) or TENDL (international). The possibility for improved dosimetry methods or creating a flux wire set that obtains the most neutron energy spectrum data with the fewest wires is of interest to the AGC program.

The methods in ASTM E481 utilize the thermal neutron products from Co and Ag wires, specifically Co-60 and Ag-110m, which can be measured with gamma spectrometry during PIE. However, Co wires, especially in a harder neutron spectrum, produce Co-58 that can be quantified with IRDFF data. Currently, a fast reaction product from silver, Ag-106m, is not utilized within the IRDFF library or ASTM standards, but this reaction is of interest to the AGC program.

Updating the ASTM E481 standard to include the Co and Ag fast reactions and validating Ag-106m production rates in IRDFF would allow the AGC program to expand their flux wire selection. Though other flux wires have similar production rates as Ag-106m, using a single wire (Ag) to obtain fast and thermal reaction products provides additional confidence in the data set due to the self-consistent reaction rates.

The current efforts have been limited to revisions of E481 for succinct, application-specific language and the evaluation of a simulated data set for Ag-106m. One area of concern is the ability to quantify Ag-106m despite the large production rate of Ag-110m from thermal neutron reactions. The results of the simulated data set show the ability to discern Ag-106m in the gamma spectrometry measurements with a variety of irradiation and cooling times in ATR.

ASTM D7846

ASTM D7846 (Reporting Uniaxial Strength Data and Estimating Weibull Distribution Parameters for Advanced Graphites) has been reviewed in the light of inconsistencies with ASME code development activities. Per this ASME review, attention has been given to the definition of outlying observations. Also, the existing standard provides modulus values for up to 120 specimens, and the method has been extended to cover larger populations. Sections on censored data have been retained. Equations for both left censored (the specimen fractured before testing) and right censored (the specimen did not break) data have been added in the draft revision. Several issues still require further clarification before this standard can be finalized.

2.3.3.3 New NEUP CINR Call

A new graphite specific Nuclear Energy University Program (NEUP) research call "Effects of Irradiation Induced Microstructure Change in Graphite" was issued in August under the Consolidated Innovative Nuclear Research (CINR) work scope. This graphite research endeavors to determine the underlying mechanisms responsible for the irradiated bulk material property changes measured within large specimens, such as those used for the AGC or INNOgraph experiments. While the graphite community believes it understands atomic level damage mechanisms within irradiated graphite, what is unclear is how this crystallographic damage changes the bulk material properties. The assumption is that the microstructure is changed somehow, and this new research should provide evidence on how these changes affect the material properties.

2.4 Design Methods and Validation

2.4.1 Severe Accident Heat Removal–Argonne National Laboratory

The Natural Convection Shutdown Heat Removal Test Facility (NSTF) is a large-scale test facility constructed at Argonne National Laboratory with support from DOE and the Office of Advanced Reactor Technologies. With this facility, the program's primary objective is to generate NQA-1 qualified validation data for passive decay heat removal systems of advanced reactors. The test article reflects key features of a ½ scale, water-based, reactor cavity cooling system and is intended study the behavior, bound performance, and, ultimately, guide design decisions for passive decay heat removal systems for advanced reactors. Over a 12-month period in FY 2020, the program conducted a total of five matrix test cases at two-phase boiling operating conditions. Of these, four were performed under standard two-phase baseline conditions for the purposes of establishing confidence in the test facility's and operator's ability to generate repeatable results.

Matrix testing began by establishing two-phase conditions that could serve as a common reference basis for nominal behavior and system parameters and to monitor system repeatability. DataQuality057 served as the two-phase reference, or baseline test case, which identified initial and boundary conditions derived from openly available literature of the full scale reactor concept. For the NSTF, these conditions defined a nominal decay heat load of 51.6 kWt, 80% fill of the primary tank or approximately 1,004 gallons of liquid inventory, riser discharge configured into tank center port, and 34.05-inch cooling panel to heated wall setback distance. An auxiliary heat removal system was configured to act as a steam condensation network, with boil-off condensate removed from the system and stored in collection reservoirs. Given that two-phase natural circulation phenomena can invoke a wide range of thermal hydraulic behavior with minimal variations in operating conditions, repeating test conditions and establishing confidence in the facility ability to generate similar results was a priority. Shown below in

Figure 59 and Figure 60 are comparisons of the tank gas space pressure and system oscillation period, strong indicators of integral system behavior, for two repeat test cases.

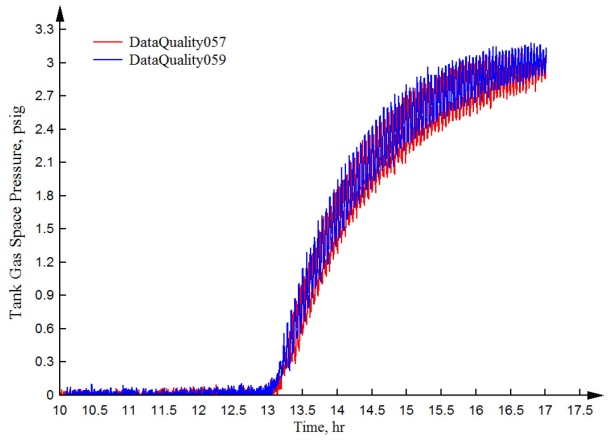

Figure 59. Repeatability comparison, tank gas space pressure.

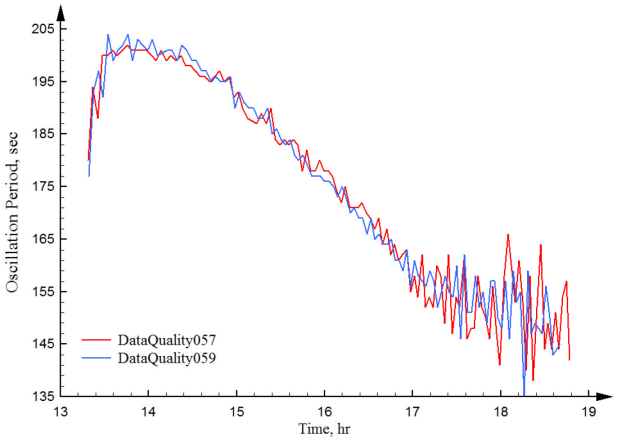

Figure 60. Repeatability comparison, loop oscillation period.

With the completion of the baseline two-phase test case (DataQuality057) and repeating facility behavior across separate test runs (DataQuality058 and DataQuality059), parametric testing was initiated with variations of the initial system inventory. These parametric tests examine the influence of static (initial) and dynamic (transient) system inventories, with four volumes identified that will study inventories ranging from overfilled, baseline, reduced, and depletion. During this year, two static inventory parametric tests were completed at a reduced initial fill level of 70% in DataQuality060 and 60% in DataQuality061. A comparison of all three test cases at varying fill levels is provided in Figure 61.

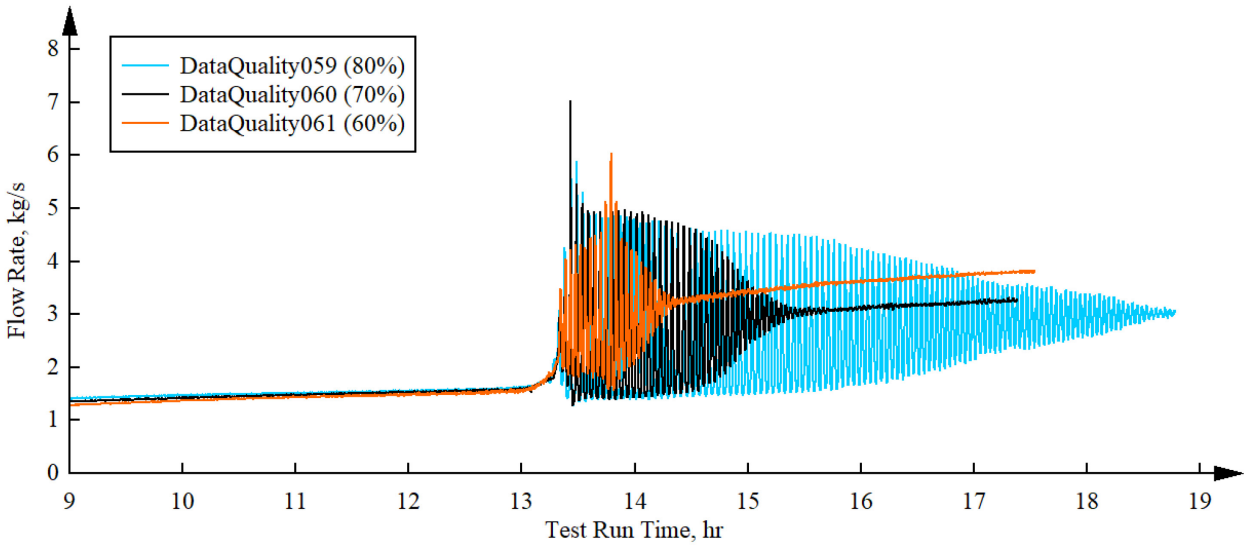

Figure 61. Comparison of system flow rate curves for tank inventory parametric, 80%, 70%, and 60% fill.

Readily apparent from the two-phase testing performed by the NSTF program is the presence of large, system-wide flow instabilities. For the baseline and the inventory parametric tests cases, the main instabilities encountered were the natural circulation oscillations and density wave oscillations (DWO). The former occurs upon the initiation of boiling or flashing and lasts for most of the two-phase duration when the voiding is not continuous and features intermittent excursions. As the test proceeds and inventory level decreases, vapor generation transitions to a continuous mode due to reducing the hydrostatic head, and the instability mechanism slowly transitions toward the DWO. Figure 62 and Figure 63 show the stability and two-phase flows regimes, including the flow oscillations transition during the systems instability modes.

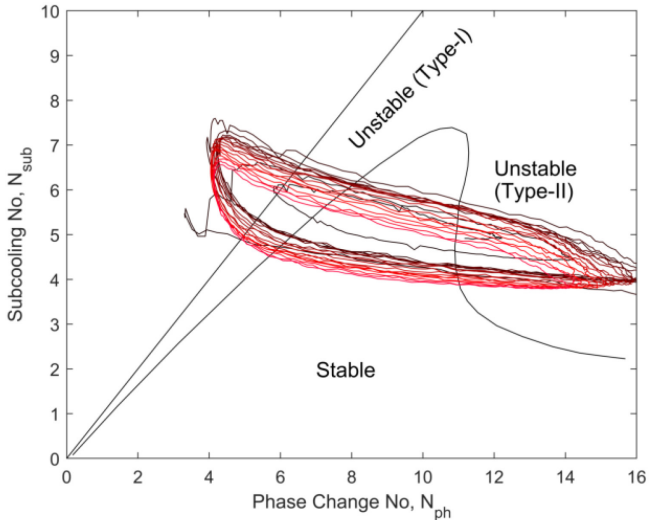

Figure 62. Flow instabilities from NSTF testing shown on a Fukuda and Kobori stability map.

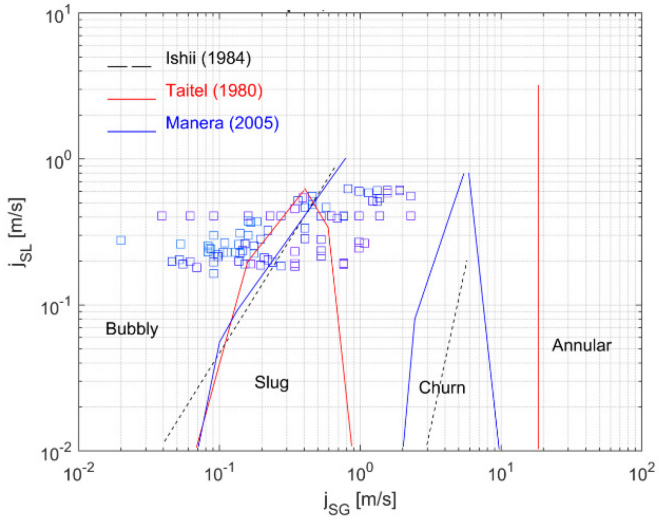

Figure 63. Two-phase flow regime mapping for a sustained DWO.

2.4.2 HTGR Methods and Core Simulation-INL

As part of the IAEA Coordinated Research Project (CRP) on high-temperature gas-cooled reactor (HTGR) uncertainty analysis in modeling (UAM), the simulations of the stand-alone thermal fluid (TF) steady-state Exercise II-4 were concluded in the fourth quarter of FY 2020. The IAEA CRP on HTGR UAM results were summarized in the L3 milestone report that was completed at the end of August 2020 and will also be published as a Ph.D. dissertation in October 2020. Selected highlights from the Exercise II-4 results are summarized here.

The IAEA CRP on HTGR UAM Phase II specification defines Exercise II-4 as a hot full-power TF-only steady-state core simulation. The core power-density distribution is provided and fixed (i.e., there is no neutronics feedback). The objective of this exercise is the isolation of the effect of TF uncertainties on the maximum fuel temperature (MFT) as the primary figure of merit (FOM). The variations in the TF boundary and material property correlations are shown in Table 13.

Table 13. Exercise II-4 TF input parameters and one standard deviation (%) values.

Input Parameter	Nominal Value	1σ Uncertainty
Boundary conditions		
Total reactor power	350 MW	± 1%
Core bypass	0% or 11%	± 1%
Reactor inlet temperature	259°C	± 1%
Helium mass-flow rate	157.1 kg/s	± 1%
Material properties		
Fuel graphite thermal conductivity	20.0 W/m.K	± 7%
Fuel graphite specific-heat capacity	3.50E+06 J/kg.K	± 3%
Reflector thermal conductivity (replaceable H-451 / permanent reflectors H-2020)	37.0 W/m.K 35.0 W/m.K	± 5%

Input Parameter	Nominal Value	1σ Uncertainty
Reflector specific-heat capacity (replaceable H-451 / permanent reflectors H-2020)	3.50E+06 J/kg.K 3.13E+06 J/kg.K	± 5%
RPV thermal conductivity	40.0 W/m.K	± 2.5%
Core-barrel thermal conductivity	17.8 W/m.K	± 2.5%

The RAVEN/RELAP5-3D calculation sequence applied for this analysis is shown in Figure 64. As a first step, RAVEN is used to create 1,000 values for each of the input parameters listed in Table 13. The RAVEN/RELAP5-3D interface subsequently creates 1,000 perturbed-input decks for RELAP5-3D and submits the cases to the computational cluster in parallel.

Two approaches are introduced in this work on the treatment of bypass flows in the RELAP5-3D model: a binary include or exclude assessment and the use of random sampling from a normal distribution defined for each of the seven defined bypass-flow channels. The first method involves the comparison of uncertainty and sensitivity parameters for two sets of simulations with the bypass flows included and excluded (i.e., assessing whether the inclusion of bypass flows in the model changes the MFT uncertainty or input-parameter sensitivity ranking).

The second method utilizes RAVEN to sample 1,000 perturbed values from normal distributions defined for each of the bypass-flow channels. A standard deviation of ±1% is assumed for these sample distributions, with the limits defined at 3σ, or ±3%. The objective of this approach is to assess whether small perturbations in the reflector and core-flow distributions lead to significant changes in either the MFT uncertainty or the sensitivity ranking of the input parameters.

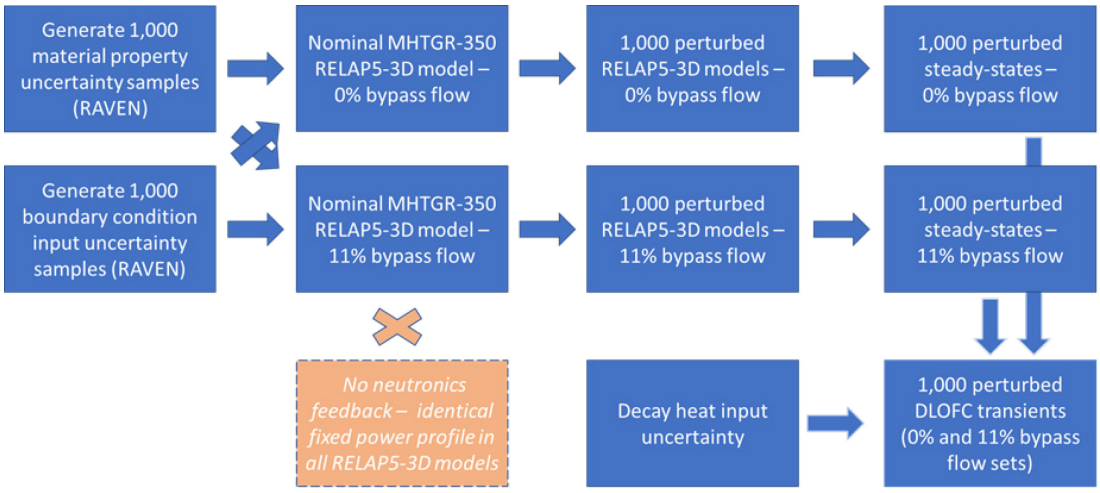

Figure 64. Coupled steady-state simulation options.

The full spatial data for all 30 fuel-temperature sets and the two model variants are presented in Table 14. The highest of these 30 fuel temperatures are designated as the MFT.

Table 14. Exercise II-4 fuel-temperature data for the 0% and 11% bypass-flow steady-states.

Axial level	Mean fuel temperature (K)			Standard deviation σ (%)			95th percentile (K)		
	FR1	FR2	FR3	FR1	FR2	FR3	FR1	FR2	FR3
With 11% bypass flows									
1	519	450	460	0.74	0.77	0.76	525	456	465
2	631	525	545	0.77	0.76	0.75	639	532	552
3	722	588	614	0.81	0.77	0.77	732	595	621
4	791	637	667	0.84	0.79	0.79	802	645	676
5	847	678	709	0.87	0.82	0.81	859	687	719
6	890	707	739	0.89	0.83	0.82	903	717	749
7	931	737	769	0.90	0.85	0.83	945	747	779
8	968	763	796	0.91	0.87	0.85	983	774	807
9	1000	785	817	0.92	0.89	0.85	1015	796	828
10	1024	802	831	0.93	0.90	0.86	1039	813	843
Zero bypass flows									
1	511	446	463	0.76	0.79	0.77	518	453	469
2	613	515	545	0.78	0.77	0.75	622	522	553
3	695	571	611	0.82	0.78	0.77	705	579	619
4	758	615	661	0.85	0.80	0.79	769	624	671
5	809	651	702	0.88	0.82	0.81	822	661	712
6	848	677	731	0.90	0.84	0.82	861	687	741
7	885	704	760	0.91	0.85	0.84	900	714	771
8	919	727	786	0.93	0.87	0.85	934	738	798
9	948	746	807	0.94	0.88	0.86	964	758	819
10	971	761	822	0.95	0.89	0.86	987	773	834

In addition to the mean and standard-deviation indicators, Table 14 also includes the 95th percentile fuel-temperature values, which could be of interest during the assessment of design margin (e.g., the margin available to an operational fuel-temperature limit of 1200 K). If the data in the two tables are compared, two main trends can be observed:

- The addition of bypass flows to the RELAP5-3D model resulted in significantly higher mean fuel temperatures because 11% (±1%) less flow through the fuel region removes less heat through forced convection. The fuel-temperature differences between the models with and without bypass flows are lowest in the upper-inlet region of the core (0.8–1.5% in the first axial level) and reach a peak difference value of 5.2% at the core-outlet region (fuel ring (FR) 1 and FR2, Level 10). This increased difference between the two models can be seen in Figure 65, where a comparison of the mean and 95th percentile FR1 fuel temperatures is shown. The axial profiles of the three fuel rings of the 0% bypass-flow model are shown in Figure 66. The inner fuel ring is substantially hotter than the central and outer fuel rings due to MHTGR-350 core loading and lack of central-reflector cooling, but the rise in fuel temperatures down the axial core height is similar.
- In contrast to this trend, the fuel-temperature uncertainty (σ) only increases from 0.7 to 0.9% from the top to the bottom of the core (i.e., the relative uncertainties in steady-state fuel temperatures are not temperature dependent). Second, there is almost no difference in the fuel-temperature uncertainties of the models with and without bypass flows.

The inclusion of bypass flows in the steady-state MHTGR-350 model therefore has a significant impact on the fuel temperatures but no impact on fuel-temperature uncertainties.

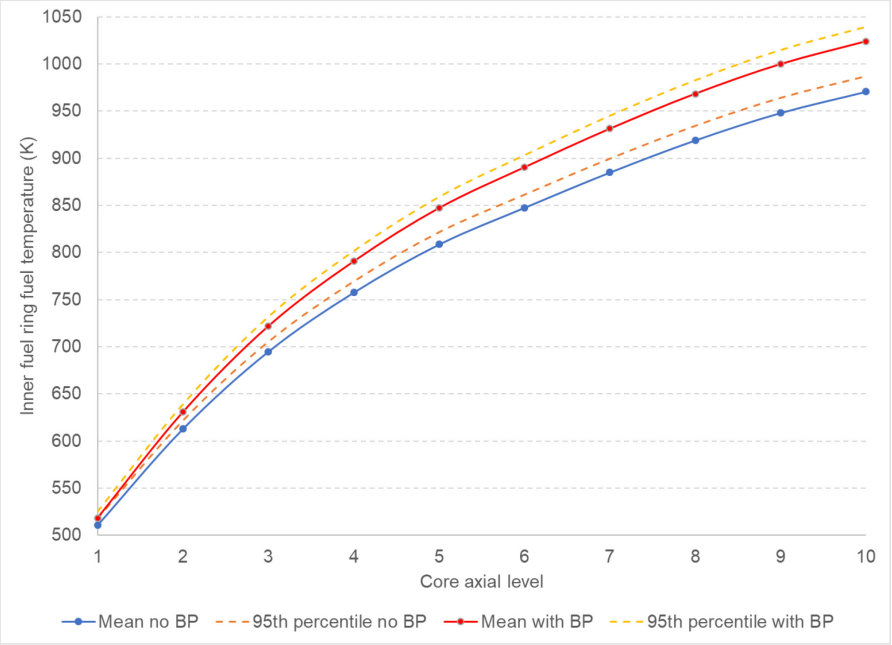

Figure 65. Comparison of the steady-state mean and 95th percentile FR1 axial fuel-temperature (K) profiles for the models with 11 and 0% bypass flows.

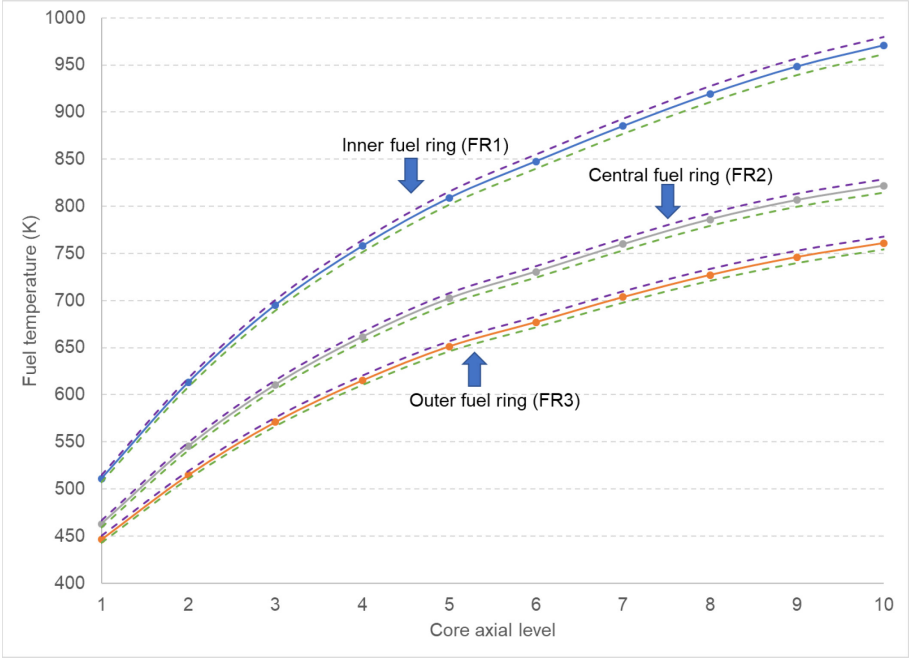

Figure 66. Comparison of FR1, FR2, and FR3 mean and standard-deviation fuel temperatures for the 0% bypass model.

For the sensitivity assessment, RAVEN is once again used to calculate typical sensitivity indictors based on the sample population. The RAVEN Pearson Correlation Coefficients (PCCs) are used as a first screening to assess whether a significant degree of linear correlation exists between the input parameters and the MFT as a main FOM. PCC values larger than $R^2 = 0.01$ are typically indicative of a meaningful degree of linear correlation, and the sensitivity coefficients determined by RAVEN can be used for a ranking assessment.

A comparison of the ranked PCCs obtained for the two bypass-flow models is presented in Figure 67 and Figure 68. Regardless of the inclusion of bypass flows in the two models, the highest-ranked parameters by a large margin are total power, inlet mass-flow rate, and inlet-gas temperature. Following the top three ranked boundary-condition parameters, the graphite H-451 core thermal conductivity is ranked fourth, with the first of the bypass flows in the fifth-ranked position. The relative magnitude of the bypass-flow PCCs and the lack of impact on the PCC ranking order both confirm that the inclusion of bypass-flow uncertainties, and even the inclusion of *any* bypass-flow channels, is not important for the determination of MFT *uncertainties*. The inclusion of the bypass flow remains, however, very important for *nominal* MFT estimates, and a larger uncertainty range should also be assessed in future work.

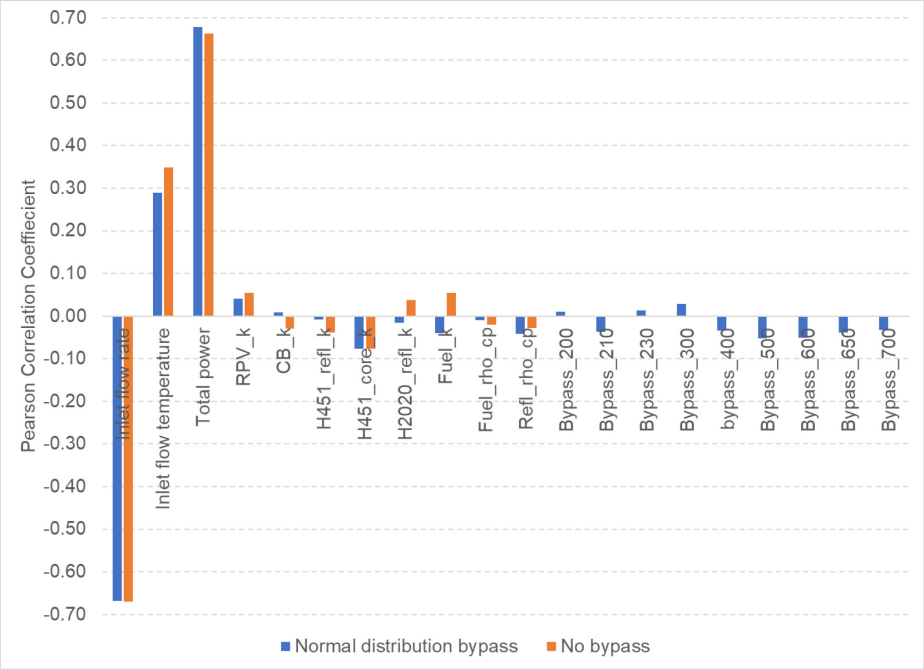

Figure 67. Comparison of steady-state MFT PCCs for models with and without bypass flows.

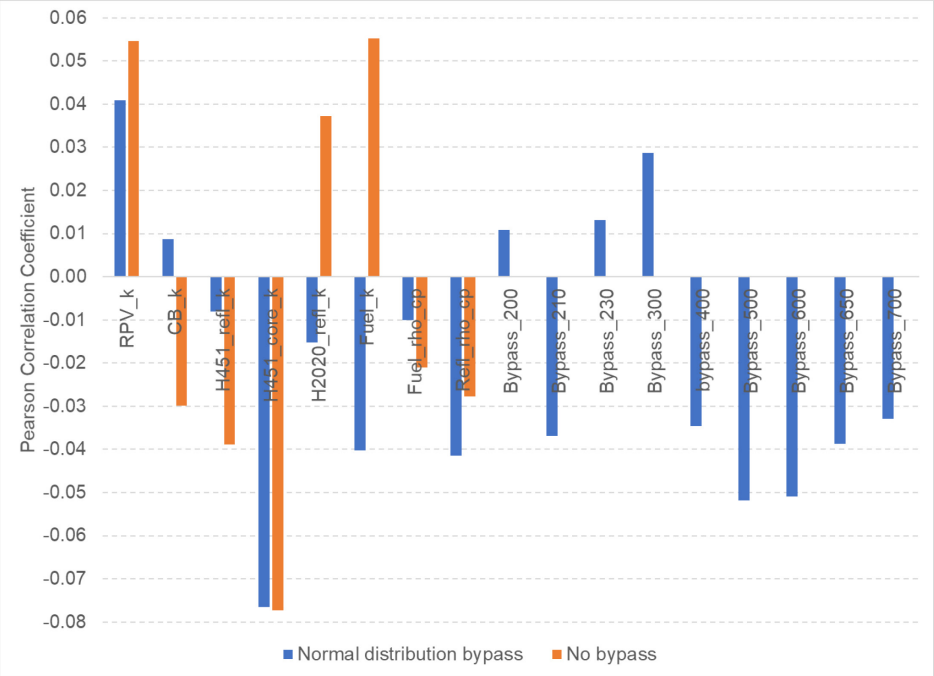

Figure 68. Details of the lower-ranked steady-state MFT PCCs for models with and without bypass flows.

3. 90-DAY LOOK AHEAD

3.1 Important Activities

3.1.1 Fuels Development

- Complete reirradiation and heating test of an AGR-3/4 fuel compact.
- Complete Stage I qualifications of equipment for the in-cell leaching of AGR-5/6/7 test train components.

3.1.2 High-Temperature Materials

- Attend the NRC Standards Forum meeting.
- Attend the U.S. DOE Materials for Harsh Service Conditions Virtual Workshop 2020.
- Participate in the November 2020 ASME BPVC Week.
- Participate in the Section III Division 5 Workshop on HTRs.
- Attend the Workshop on Advanced Manufacturing Technologies for Nuclear Applications.
- Sustain ongoing creep-rupture tests. These specimens include Alloy 800H weldments with Alloy 617 filler and Alloy 617 containing various geometric discontinuities. The data will be analyzed as tests finish. Metallography and optical microscopy will be used to characterize specimens of interest.
- Start a creep-rupture test (750°C, 51 MPa) of a cross-weld specimen with Alloy 800H base metal and Alloy 617 filler.
- Start a creep-rupture test (850°C, 38 MPa) of a cross-weld specimen with Alloy 800H base metal and Alloy 617 filler.
- Start a creep-rupture test (800°C, 60 MPa) of a weld-metal Alloy 617 V-notch specimen.

- Analyze the XCT data from the notch and straight gauge of a ruptured baseline base-metal Alloy 617 V-notch creep-rupture (800°C, 65.3 MPa) specimen.
- Perform cyclic testing of Alloy 617 weldments with Alloy 617 filler. The data will be analyzed as tests finish. Metallography and a combination of optical microscopy and SEM will be used to characterize specimens of interest.
- Draft a journal article on the elevated-temperature cyclic and creep properties of diffusion-welded Alloy 617.
- Compare the simulated damage of U-notch creep-rupture specimens from finite-element modeling against experimental results to evaluate different damage models.
- Perform metallography and optical microscopy on the ruptured cross-weld creep specimen with Alloy 800H base metal with Alloy 617 filler that was tested at 800°C, 47.708 MPa.
- Perform metallography and optical microscopy on the ruptured cross-weld creep specimen with Alloy 800H base metal with Alloy 617 filler that was tested at 800°C, 35.841 MPa.

3.1.3 Graphite Development and Qualification

- Investigate incorporating radiation effects into the microstructurally based phase-field fracture model.
- Explore the effect of local heat generation during graphite oxidation.
- Provide final draft of responses to Numark Inc. comments on the ASME code to NRC in October 2020.
- Complete disassembly and issue Level 2 milestone report, “Report detailing disassembly of AGC-4 and preparing the samples for PIE” (due FY 2021, previously due July 31, 2020).
- Submit manuscript “Graphite Material Property Changes After Oxidation”, for Level 3 milestone due November 2020.
- Participate in virtual ASTM Fall and Winter Meetings, October 8, 2020, and December 17, 2020 (WebEx).
- Attend the virtual ASME Code Week, November 8-13, 2020 (Zoom).
- Issue “AGC-4 Experiment Irradiation Monitoring Data Qualification Final Report” for Level 2 milestone due December 2020.

3.1.4 Methods

- Continue the planned matrix testing at the ANL NSTF
- Provide input to the IAEA summary document on the CRP on HTGR UAM.